

MASADA: From Microlensing Planet Mass-Ratio Function to Planet Mass Function

ANDREW GOULD^{1,2}

¹*Max-Planck-Institute for Astronomy, Königstuhl 17, 69117 Heidelberg, Germany*

²*Department of Astronomy, Ohio State University, 140 W. 18th Ave., Columbus, OH 43210, USA*

ABSTRACT

Using current technology, gravitational microlensing is the only method that can measure planet masses over the full parameter space of planet and stellar-host masses and at a broad range of planet-host separations. I present a comprehensive program to transform the ~ 150 planet/host mass ratio measurements from the first 6 full seasons of the KMTNet survey into planet mass measurements via late-time adaptive optics (AO) imaging on 30m-class telescopes. This program will enable measurements of the overall planet mass function, the planet frequency as a function of Galactic environment and the planet mass functions within different environments. I analyze a broad range of discrete and continuous degeneracies as well as various false positives and false negatives, and I present a variety of methods to resolve these. I analyze the propagation from measurement uncertainties to mass and distance errors and show that these present the greatest difficulties for host masses $0.13 \lesssim (M/M_\odot) \lesssim 0.4$, i.e., fully convective stars supported by the ideal gas law, and for very nearby hosts. While work can begin later this decade using AO on current telescopes, of order 90% of the target sample must await 30m-class AO. I present extensive tables with information that is useful to plan observations of more than 100 of these planets and provide additional notes for a majority of these. Applying the same approach to two earlier surveys with 6 and 8 planets, respectively, I find that 11 of these 14 planets already have mass measurements by a variety of techniques. These provide suggestive evidence that planet frequency may be higher for nearby stars, $D_L \lesssim 4$ kpc compared to those in or near the Galactic bulge. Finally, I analyze the prospects for making the planet mass-function measurement for the case that current astronomical capabilities are seriously degraded.

Subject headings: gravitational lensing: micro

1. Introduction

Microensing is the only technique that can, using existing and under-construction instruments, routinely deliver accurate planet mass measurements over a broad range of planetary and host masses and a broad range of orbital separations. This statement may seem surprising because microlensing light-curve analysis routinely returns only the planet-host mass ratio, q , while light-curve based measurements of the host mass, M_{host} , (and so the planet mass $m = qM_{\text{host}}$), are the rare exceptions.

On the other hand, several other techniques do yield many mass measurements. Most notably, the transit technique routinely identifies planet candidates (based on planet/host radius ratio measurements, together with photometric estimates of the source radius), which then permit, in favorable cases, spectroscopic followup that measures the radial velocity (RV) curve and so yields the planet mass (after taking account of the fact that the transit itself demonstrates that the orbital inclination is close to $i \sim 90^\circ$). However, due to low RV signal, together with the rarity of transits at wide orbital separations, this method rapidly loses sensitivity for low-mass hosts, low-mass planets and orbits of more than a few tens of solar radii.

The RV technique can detect planets with periods ranging from of order a day to several decades, i.e., a factor ~ 500 in semi-major axis, making it the most versatile planet-detection technique in this sense. However, the quantity that it directly measures (as with microlensing light curves) is not m itself, but rather the product of this quantity with something else, i.e., $m \sin i$, where i is the inclination. The inclination can be recovered for the small fraction of RV planets that are transiting (so, $\sin i \simeq 1$, as noted above). And for any individual system, i can in principle be measured from astrometric follow-up observations. Indeed, it is expected that *Gaia* astrometry will yield $\sin i$ (and so m) measurements for some known RV planets, and that more m measurements will come from RV follow-up of *Gaia* astrometric planet discoveries. However, given *Gaia*'s precision, these planet-mass measurement will be restricted primarily to Jovian and super-Jovian planets orbiting F and G stars in one-to-few year orbits. Unfortunately, while the technology exists to make much more precise astrometric measurements, which would greatly extend this technique to lower-mass hosts and planets (Unwin et al. 2008), there are no active programs to implement this design.

By contrast, the overwhelming majority of microlensing planet detections can be transformed into planet-mass measurements by the “simple” expedient of imaging the host after it has separated from the microlensed source on the sky. The reason that this “simple” idea has not been widely implemented is that, using current instruments, the typical wait time to separately resolve the host is of order 15 years. Because only about a half dozen microlensing planets were discovered as of 15 years ago, the total number of microlensing planets with

mass measurements using this technique is still quite small, being mainly restricted to favorable cases rather than just the planets that were discovered first. Moreover, it would be difficult to rigorously characterize the sample of early microlensing planets from a statistical point of view, so that it is not completely clear what one would learn from simply measuring the masses of all early microlensing planets.

However, the situation is rapidly changing in three respects. First, the rate of planet detections (with good light-curve characterization) has increased to about 25 per year, beginning with the inauguration of regular operations of the Korea Microlensing Telescope Network (KMTNet, Kim et al. 2016) experiment. While regular operations began in 2016, leading to annual discoveries of about 3000 events from the EventFinder (Kim et al. 2018a), and while microlensing alerts were being generated in real time by 2018 (Kim et al. 2018b), it was only in the last year that the new AnomalyFinder system (Zang et al. 2021, 2022b) began to detect planets in a uniform way. In particular, the 2018 season has now been fully analyzed (Gould et al. 2022; Jung et al. 2022), and it has yielded 33 planets that are suitable for a mass-ratio function analysis. Preliminary analysis of other seasons indicates that this is likely to be somewhat above average. In this paper, I assume a rate of 25 planets per year that will have well-characterized light curves.

Second, as just indicated, the planetary sample is being homogeneously selected. In fact, the KMT sample that is the present focus is just the latest and largest of three homogeneously selected samples, which are already being subjected to analyses to determine the planet-host mass-ratio function (Shvartzvald et al. 2016; Suzuki et al. 2016; Zang et al. 2023b). See Section 7 for more details about earlier surveys. These mass-ratio function studies have independent importance, not only because they can be completed much sooner, but also because we do not yet know whether mass or mass ratio is the more fundamental quantity in planet formation. The fact of homogeneous selection means that once the planet masses are measured, the sample can be subjected to rigorous statistical analysis for the planet mass function (and also for planet frequency as a function of host mass and Galactic environment).

Third, the next generation of telescopes, i.e., extremely large telescopes (ELTs), which are already under construction, will have apertures of 25–39 meters, i.e., about 4 times larger than those of current “large” telescopes, which are 6.5–10 meters. This ratio implies that the resolution is 4 times better, so the wait times will be 4 times shorter. That is, at adaptive optics (AO) first light on these telescopes (perhaps 2030), the “typical” wait time will be about 4 years and a “conservative” wait time will be about twice that, i.e., 8 years. Hence, the great majority of planets discovered up through this year (2022), can have mass measurements at ELT AO first light. According to the above rate estimate, this implies a sample of about 150 AnomalyFinder planets 2016–2022 (taking account of the fact that 2020

was mostly a “lost year”). Assuming that KMTNet continues to operate in a similar mode until 2028, the sample would roughly double to 300, which could then mostly be accessible to mass measurements by 2035.

In a substantial majority of cases, a single late-time image in a single band will be sufficient to make a correct and reasonably precise mass measurement. The technique itself was first applied by Alcock et al. (2001), and a closely related idea was already advanced by Refsdal (1964). It has been successfully applied to 6 planetary events: OGLE-2005-BLG-071 (Bennett et al. 2020), OGLE-2005-BLG-169 (Batista et al. 2015; Bennett et al. 2015), MOA-2007-BLG-400 (Bhattacharya et al. 2021), MOA-2009-BLG-319 (Terry et al. 2021), OGLE-2012-BLG-0950 (Bhattacharya et al. 2018), and MOA-2013-BLG-220 (Vandorou et al. 2020).

However, as I will show, mass application of this technique (in its simplest form) will also lead to a significant number of incorrect measurements, together with detection failures that arise from various causes. As I also show, it is straightforward to identify and correct these incorrect measurements, but this requires additional observing resources and additional time. Given that the overall program already requires substantial observing time on large and (still to be completed) very large telescopes, it is essential to understand these potential complications before the observing program is undertaken in earnest. Similarly, it is essential to conduct the observations in such a way as to minimize the non-detections of hosts that are (ultimately) detectable.

Here, I systematically address these issues in the context of a program of mass measurements of planets that have been (or will be) detected in the KMTNet survey. Some aspects have been investigated previously, in which case I present brief summaries and appropriate references. Other aspects have not been addressed or have been investigated only partially. In any case, the orientation here is on giving a systematic treatment.

Although the paper is framed in terms of the KMTNet sample, there are at least four other samples (three historic and one prospective) to which the same methods and principles could be applied. I briefly discuss these as well.

2. The Basic Method

The basic method is simply to image the lens (host) and source after they have moved sufficiently far from each other to separately resolve them. As mentioned in Section 1, this has already been done for a total of 6 planetary events, using AO on the Keck telescope for all 6 and also using the *Hubble Space Telescope (HST)* for several of these. In this section, I

will treat the “basic method” as implying single-band imaging in some infrared (IR) band, for example, I will assume K band.

The results of these late-time measurements are combined with the microlensing timescale, t_E ,

$$t_E \equiv \frac{\theta_E}{\mu_{\text{rel}}}; \quad \theta_E \equiv \sqrt{\kappa M \pi_{\text{rel}}}; \quad \kappa \equiv \frac{4G}{c^2 \text{au}} \simeq 8.14 \frac{\text{mas}}{M_\odot}, \quad (1)$$

which is measured during the event. Here, $(\pi_{\text{rel}}, \boldsymbol{\mu}_{\text{rel}})$ are the lens-source relative (parallax, proper motion), $\mu_{\text{rel}} \equiv |\boldsymbol{\mu}_{\text{rel}}|$, and M is the lens mass. The essence of the method is that, at late times, one measures the vector lens-source separation, $\Delta\boldsymbol{\theta}$, and then derives

$$\boldsymbol{\mu}_{\text{rel, hel}} = \frac{\Delta\boldsymbol{\theta}}{\Delta t}; \quad \Delta t \equiv t_{\text{obs}} - t_0, \quad (2)$$

where t_{obs} is the time of the observation and t_0 is the time of closest approach of the source to the host during the event. Note that in this equation, $\boldsymbol{\mu}_{\text{rel}}$ is further subscripted by “hel”, indicating that what is measured here is the *heliocentric* proper motion. By contrast, the timescale measured during the event (i.e., t_E without subscript) is the *geocentric* timescale. The heliocentric (with subscript) and geocentric (without subscript) parameters are related by,

$$\theta_E \equiv \mu_{\text{rel}} t_E = \mu_{\text{rel, hel}} t_{E, \text{hel}} \quad \boldsymbol{\mu}_{\text{rel, hel}} = \boldsymbol{\mu}_{\text{rel}} + \frac{\pi_{\text{rel}}}{\text{au}} \mathbf{v}_{\oplus, \perp}, \quad (3)$$

where $\mathbf{v}_{\oplus, \perp}$, which is known exactly, is Earth’s velocity relative to the Sun at t_0 , projected on the sky.

For completeness, I note that Equation (2) is strictly correct only if the measurement is made at the same time of year as the peak of the event, t_0 . Otherwise, there is a correction of order $\sim \pi_{\text{rel}}/\Delta\theta$, which is typically $\mathcal{O}(10^{-3})$, i.e., far below the level of other errors in the measurement. Hence, although it is no trouble to include this correction in practical measurements, I ignore it here in the interest of clear exposition.

There are then two measured quantities (proper motion $\boldsymbol{\mu}_{\text{rel, hel}}$ and the host K -band flux) and two unknowns (the host mass M_{host} and the lens-source relative parallax π_{rel}). Ignoring for the moment the possibility of false positives (see Section 4), the two measurements lead to two equations that relate M_{host} to π_{rel} , and so (in the great majority of cases, see below) to a unique measurement of these two quantities. Specifically,

$$(1 + q)\kappa M_{\text{host}} \pi_{\text{rel}} = \left(\boldsymbol{\mu}_{\text{rel, hel}} - \frac{\pi_{\text{rel}}}{\text{au}} \mathbf{v}_{\oplus, \perp} \right)^2 t_E^2, \quad (4)$$

and

$$K = M_K(M_{\text{host}}) - 5 \log\left(\frac{\pi_L}{\text{mas}}\right) + 10 + A_K(\pi_L); \quad \pi_L = \pi_{\text{rel}} + \pi_S, \quad (5)$$

where $M_K(M_{\text{host}})$ is the K -band mass-luminosity relation of the host star, π_S is the source parallax, π_L is the lens parallax, and $A_K(\pi_L)$ is the K -band extinction at the lens distance, $D_L = \text{au}/\pi_L$. Note that while Equations (4) and (5) contain 3 quantities that are either known exactly ($\mathbf{v}_{\oplus, \perp}$) or whose errors are often so small that they can be ignored (K and $\boldsymbol{\mu}_{\text{rel, hel}}$), they also contain four other terms whose uncertainties generally need to be taken into account. These are the Einstein timescale t_E , the source parallax π_S , the mass-luminosity relation $M_K(M_{\text{host}})$, and the extinction as a function of distance, $A_K(\pi_L)$. Note also that I have included the term “ $(1 + q)$ ” in Equation (4) for completeness, although (because $q \ll 1$ for planets), it can be ignored at the conceptual level.

For any individual event, the usual procedure is to consider all possible pairs of $(M_{\text{host}}, \pi_{\text{rel}})$ and ask what is the total χ^2 from Equations (4) and (5), taking account of the measurement errors in t_E , $\boldsymbol{\mu}_{\text{rel, hel}}$ and K , as well as the theoretical uncertainties in π_S and in the functions $M_K(M_{\text{host}})$ and $A_K(\pi_L)$. However, here my goal is to investigate the robustness of the method as a whole and to identify the regions of parameter space in which it may be degraded or even fail completely. Thus, I begin by assuming that all measurements errors and theoretical uncertainties are zero, and I will subsequently relax these assumptions.

By assumption, the host has yielded a measurable K -band flux. This already implies that the host is luminous in K , i.e., not a brown dwarf (BD), white dwarf (WD), neutron star (NS), or black hole (BH), for which the method will fail, at least in its “basic” form. I will also ignore for the moment the possibility (extremely rare in microlensing) that the host is an evolved star¹. Then, $M_K(M_{\text{host}})$ is a monotonically declining function, which can thus be inverted to $M_{\text{host}}(\pi_L) = M_K^{-1}(\Delta K(\pi_L))$, where $\Delta K(\pi_L) = K + 5 \log(\pi_L/\text{mas}) - A_K(\pi_L) - 10$. Because $M_K^{-1}(\Delta K)$ and $\log(\pi_L/\text{mas})$ are monotonically increasing, while $A_K(\pi_L)$ is monotonically decreasing, $M_{\text{host}}(\pi_L)$ is monotonically decreasing. Given my initial approximation that π_S is known, it follows that $M_{\text{host}}(\pi_{\text{rel}})$ is also monotonically decreasing.

Equation (4) is easily solved for $M_{\text{host}}(\pi_{\text{rel}})$ by dividing both sides by $(1 + q)\kappa\pi_{\text{rel}}$. The naive hope would be that the $M_{\text{host}}-\pi_{\text{rel}}$ curves resulting from these two equations would intersect in one and only one place. Following the assumption that the measurements and physical relations are exact, they must intersect at at least one point, namely the $(M_{\text{host}}, \pi_{\text{rel}})$ values of the actual host. However, inspection of Equation (4) shows that it is not the case that this intersection is unique. One sees that $M_{\text{host}} \rightarrow \infty$ in both of the limits of $\pi_{\text{rel}} \rightarrow \infty$ and $\pi_{\text{rel}} \rightarrow 0$ (respectively, $D_L \rightarrow 0$ and $D_L \rightarrow D_S$), while M_{host} achieves a minimum

¹Such hosts would likely become targets for spectroscopic observations that would not generally require extreme telescope resources.

$M_{\text{host,min}}$ at $\pi_{\text{rel,min}}$, given by

$$\pi_{\text{rel,min}} = \frac{\mu_{\text{rel,hel}} \text{au}}{v_{\oplus,\perp}} = 0.95 \text{ mas} \left(\frac{\mu_{\text{rel,hel}}}{6 \text{ mas yr}^{-1}} \right) \left(\frac{v_{\oplus,\perp}}{30 \text{ km s}^{-1}} \right)^{-1}, \quad (6)$$

$$M_{\text{host,min}} = 2 \frac{\mu_{\text{rel,hel}} v_{\oplus,\perp}}{(1+q)\kappa \text{au}} t_{\text{E}}^2 (1 - \cos \phi) = 0.063 M_{\odot} \left(\frac{\mu_{\text{rel,hel}}}{6 \text{ mas yr}^{-1}} \right) \left(\frac{v_{\oplus,\perp}}{30 \text{ km s}^{-1}} \right) \left(\frac{t_{\text{E}}}{30 \text{ day}} \right)^2 (1 - \cos \phi), \quad (7)$$

where $\cos \phi \equiv \boldsymbol{\mu}_{\text{rel,hel}} \cdot \mathbf{v}_{\oplus,\perp} / \mu_{\text{rel,hel}} v_{\oplus,\perp}$ and where I have made the final evaluation assuming $q \ll 1$.

For the general case, there will then be an even number of points of intersection between the curves derived from Equation (4) and (5), and, as a practical matter, this “even number” will almost always be “two”. We will see that if these two points are both on the low- π_{rel} (i.e., $\pi_{\text{rel}} < \pi_{\text{rel,min}}$) side of Equation (4), then this can lead to a “continuous degeneracy”. I will address this case in Section 5. Here, I focus on the great majority of cases, i.e., those with a discrete two-fold degeneracy for which one solution has $\pi_{\text{rel}} > \pi_{\text{rel,min}}$ and the other has $\pi_{\text{rel}} < \pi_{\text{rel,min}}$. If there were no way to resolve this degeneracy, it would seriously undermine the “basic method”. However, there are several approaches to resolving this degeneracy. See Sections 3 and 5.

Figures 1 and 2 illustrate the “basic method” using K_{host} photometry and $\boldsymbol{\mu}_{\text{rel,hel}}$ measurements from the six planetary events mentioned above. (For OGLE-2005-BLG-169, I adopt $K_{\text{host}} = H_{\text{host}} - 0.11$). For the mass luminosity relation, I adopt the Baraffe et al. (2015) 1 Gyr isochrones, which are shown in Figure 3. The source distance is held fixed at $D_S = 1.08 \times 10^{(I_{0,\text{clump}} - M_{I,\text{clump}})/5 - 2}$ kpc where $M_{I,\text{clump}} = -0.12$ and $I_{0,\text{clump}}$ is given by Table 1 from Nataf et al. (2013). I employ a dust model with a scale height of 120 pc. These figures have some interesting features, some of which I point out now, while others will be noted in Section 3.

The first point is that while figures with the same axes as Figure 2 appear in four of the six Keck papers (corresponding to the four lower panels of Figure 2), none of these show the high- π_{rel} branch of Equation (4). For MOA-2009-BLG-319 (Figure 5 of Terry et al. 2021) and MOA-2009-BLG-220 (Figure 5 of Vandorou et al. 2020), this is because the figures are restricted to the region near the solution. For OGLE-2012-BLG-0950, Figure 6 from Bhattacharya et al. (2018) is not directly comparable to Figure 2 because it only shows the $\boldsymbol{\mu}_{\text{rel,hel}}$ constraint after it is combined with a π_{E} constraint that is derived from the light curve. On the other hand, for MOA-2007-BLG-400, Figure 4 of Bhattacharya et al. (2021) displays the entire parameter space, but does not show this feature. However, it is also barely visible in Figure 2, where it is mainly superposed on the y-axis, although it is clearly visible in Figure 1. Nevertheless, one can see from Figure 2 (and better from Figure 1) that there

are cases for which Equation (5) intersects Equation (4) on its high- π_{rel} branch. I will show in Sections 3 and 5 that Batista et al. (2015) were correct to ignore this second solution, but this shows that, in general, these solutions must be considered.

Second, it is striking that for two of the 6 events, i.e., OGLE-2005-BLG-071 and OGLE-2012-BLG-0950, the “intersection” of the two equations takes the form of an “extended tangent”. At first, one might think that this a rare coincidence, but it is actually rooted in the peculiar “inflection” which is highlighted in Figure 3 and (as I will explain in Section 5) is especially critical for relatively nearby lenses.

Figure 4 illustrates how Equations (4) and (5) behave as key parameters change. For all 12 curves shown in this figure, I hold fixed $t_E = 25$ day, $\pi_S = 0.115$ mas, $A_K = 0.13$, $b = -3.0$, and $v_{\oplus,\perp} = 25$ km s $^{-1}$. That is, I fix all the quantities that are known (within errors) in advance of the high-resolution observations.

The three black curves show Equation (4) for $\mu_{\text{rel}} = 6$ mas yr $^{-1}$ and three values (from top to bottom) of $\cos\phi = (-1, 0, +1)$. Similarly, the red curves show Equation (4) for $\mu_{\text{rel}} = 3$ mas yr $^{-1}$. The curves with small circle show Equation (5) for 6 different values (top to bottom) of $K_{\text{host}} = (14, 16, 18, 20, 22, 24)$

Before continuing, I note the “basic method” for measuring host masses from resolved host-source pairs is closely related to another method that measures host masses from unresolved host-source pairs. Both methods generally rely on high-resolution imaging to exclude (or limit) light from other stars, and both derive the mass from a combination of measurements of K_{host} (or flux in some other band) and θ_E . The “unresolved” method has the major advantage that there is no need to wait for the host and source to separate. However, it has several major restrictions and disadvantages. First, it is restricted to cases for which the host is not too much fainter than the source: otherwise, the source light cannot be accurately subtracted from the combined flux. Second, it is restricted to the subsample of planets (roughly 2/3, see Section 3.1) for which there is a θ_E measurement from the light curve. Third, it runs a greater risk of falsely identifying another star as the host. See the examples of MOA-2016-BLG-227 (Koshimoto et al. 2017b) and MOA-2008-BLG-310 (Bhattacharya et al. 2017) in Sections 6.1.1 and 7.1, respectively. Nevertheless, this method has important applications, e.g., for OGLE-2006-BLG-109 (Bennett et al. 2010), OGLE-2007-BLG-349 (Bennett et al. 2016), and OGLE-2017-BLG-1434 (Blackman et al. 2021). See Sections 7.1 and 6.1.1.

3. Methods to Break the Discrete Degeneracy

Even within the context of the “basic method”, the discrete degeneracy that was discussed in Section 2 can be broken definitively in a substantial majority of cases. Moreover, for a majority of the cases that it cannot be broken definitively, the low- π_{rel} solution will be strongly favored statistically. Finally, it can essentially always be broken by taking one additional observation.

3.1. Geocentric Proper-Motion Measurements

In most cases (see the paragraph after next), the planetary event will have itself yielded an independent measurement of θ_{E} , via the source-size parameter $\rho = \theta_*/\theta_{\text{E}}$, where θ_* is the angular size of the source. This parameter is required to fit the light curve whenever it is strongly impacted by caustics, and, when ρ is needed, it is usually measured to better than 10%. Then θ_* can also be measured using standard techniques (Yoo et al. 2004), also usually to better than 10%. Hence, $\theta_{\text{E}} = \theta_*/\rho$ and $\mu_{\text{rel}} = \theta_{\text{E}}/t_{\text{E}}$ are usually known to about 10%. For a typical event, the true value of π_{rel} will be small, e.g., $\pi_{\text{rel,true}} \lesssim 0.05$ mas, whereas in the alternate solution, it will be $\pi_{\text{rel,alt}} \gtrsim 1$ mas. Using the same fiducial parameters as above, the two solutions would predict $\mu_{\text{rel}} \simeq \mu_{\text{rel,hel}}$ and $\mu_{\text{rel}} \gtrsim 1.5\mu_{\text{rel,hel}}$, respectively. Hence, they could be distinguished by ρ -based measurements of μ_{rel} that are of typical quality.

The historical example of OGLE-2005-BLG-169 illustrates this point. Although, nominally, Equation (5) “ends” before it intersects the high- π_{rel} branch in Figure 1, it does so only marginally, and this would not be the case once measurement errors were taken into consideration. However, lines with slopes of +1 on this figure have constant θ_{E} . Thus, one can see by eye that the two solutions are offset by $\Delta \log \theta_{\text{E}} = 0.5(\Delta \log M + \Delta \log \pi_{\text{rel}}) \simeq 0.42$, i.e., a factor 2.6. Because θ_{E} was reasonably well measured, the alternate solution would be ruled out by this argument. In fact, we will see that it would be ruled out by two other arguments as well.

However, as predicted by Zhu et al. (2014) and confirmed by Jung et al. (2022), of order half of microlensing planets do not have caustic crossings. In particular, Jung et al. (2022) found that of 33 planets from 2018 that were suitable for statistical studies, only 16 had caustic crossings. Nevertheless, a review of the remaining 17 shows that five (OGLE-2018-BLG-0298Lb², KMT-2018-BLG-0087Lb, OGLE-2018-BLG-1185Lb, OGLE-2018-BLG-

²This event has two solutions, one in which the source crosses the caustic and another in which it crosses a ridge extending from a cusp. It is classified as “non-caustic-crossing” because the latter solution has lower

1011b, and OGLE-2018-BLG-1011c) have good measurements of ρ , while three others have useful constraints on ρ (OGLE-2018-BLG-0977Lb, OGLE-2018-BLG-0506Lb, and OGLE-2018-BLG-1647Lb).

Based on this experience, I estimate that this method can resolve the degeneracy for $\sim 2/3$ of planets.

3.2. Microlens Parallax

A substantial fraction, probably a majority, of the alternate, high- π_{rel} solutions can be decisively rejected based on microlensing-parallax constraints that are derived from the original light curves. This statement may seem surprising because only a minority of published microlensing-planet analyses even report parallax parameters, and, of those that do, many give only constraints rather than measurements.

However, there are two factors that make microlensing parallax a much more powerful tool for rejecting high- π_{rel} alternate solutions than for making parallax measurements. First, the alternate solutions generally have very large values of the microlensing parallax, π_{E} . Second, these alternate solutions make very precise predictions of the direction of the parallax vector, $\boldsymbol{\pi}_{\text{E}}$. Hence, the high- π_{rel} solution can be ruled out, even when the parallax analysis was not considered to be sufficiently constraining to warrant being reported in the original papers. Here,

$$\boldsymbol{\pi}_{\text{E}} = \pi_{\text{E}} \frac{\boldsymbol{\mu}_{\text{rel}}}{\mu_{\text{rel}}}; \quad \pi_{\text{E}} \equiv \frac{\pi_{\text{rel}}}{\theta_{\text{E}}} = \sqrt{\frac{\pi_{\text{rel}}}{\kappa M}} = 1.57 \left(\frac{\pi_{\text{rel}}}{2 \text{ mas}} \right)^{1/2} \left(\frac{M}{0.1 M_{\odot}} \right)^{-1/2}. \quad (8)$$

The first point is that the illustrative values used in Equation (8) are typical of the real problem under consideration. From Equation (6), $\pi_{\text{rel},\text{min}} \sim 1 \text{ mas}$, while (by definition) the high- π_{rel} branch has $\pi_{\text{rel}} > \pi_{\text{rel},\text{min}}$. And because, typically, $\pi_{\text{rel},\text{true}} \ll 1 \text{ mas} \sim \pi_{\text{rel},\text{min}}$ (and $M_{\text{host}}(\pi_L) = M_K^{-1}(\Delta K(\pi_L))$ is monotonically declining), it is likely that the host mass in the high- π_{rel} solution is a factor several lower than the true mass. Hence, typically, $\pi_{\text{E}} \gtrsim 1$ for the high- π_{rel} solution.

However, this fact, in itself, would not be enough to rule out such solutions for typical planetary events. To understand why, I examine some “typical” cases of “marginally interesting” microlens parallax constraints. By this I mean, cases for which the parallax solutions would not traditionally be published because they were regarded as “not constraining”, but

χ^2 . In any case, the two solutions have similar values and error bars for ρ .

which were in fact published due to my own initiative. I focus on KMT-2018-BLG-2004 and OGLE-2018-BLG-1367, which are both illustrated in Figure 3 of Gould et al. (2022). In both cases, the parallax amplitude is consistent with all values $0 \leq \pi_E \lesssim 3$. and so appears to contain essentially no information. The parallax constraints were nevertheless included in the Bayesian analyses of that paper because the effectively 1-dimensional (1-D) contours (Gould et al. 1994) in the 2-D $\boldsymbol{\pi}_E$ plane do in fact contain some information. Note, however, that for the illustrative example of Equation (8), the constraint $\pi_E \lesssim 3$ would not exclude the high- π_{rel} solution, i.e., $\pi_E = 1.57$.

Nevertheless, inspection of Figure 3 from Gould et al. (2022) shows that if $\boldsymbol{\pi}_E$ were additionally constrained to lie at least 10° from the long-axis of these contours, then this solution would be excluded.

Now, if one were to assume that the direction of $\boldsymbol{\pi}_E$ for the (wrong) high- π_{rel} solution was randomly distributed relative to this long axis, then one would conclude that $1 - (4 \times 10^\circ / 360^\circ) = 89\%$ of spurious high- π_{rel} solutions could be excluded, provided that the parallax-contour measurements were of comparable quality to Figure 3 of Gould et al. (2022). In fact, however, the situation is substantially more favorable. The first point is that for the high- π_{rel} solution, by definition, $\pi_{\text{rel}} > \pi_{\text{rel},\text{min}} = \mu_{\text{rel,hel}}\text{au}/v_{\oplus,\perp}$. Hence, the direction of $\boldsymbol{\pi}_E$ (same as that of $\boldsymbol{\mu}_{\text{rel}} = \boldsymbol{\mu}_{\text{rel,hel}} - \mathbf{v}_{\oplus,\perp}\pi_{\text{rel}}/\text{au}$), is more closely aligned to the direction of $\mathbf{v}_{\oplus,\perp}$ than to $\boldsymbol{\mu}_{\text{rel,hel}}$, and usually substantially so. However, for a substantial majority of the microlensing season, $\mathbf{v}_{\oplus,\perp}$ points approximately due east (or due west).

On the other hand, for a substantial majority of the microlensing season, the major axis of the 1-D parallax contours is roughly aligned north-south. This is because, for events that are short compared to a year, Earth’s acceleration can be approximated as constant, and the parallax vector is much better constrained in the direction of this acceleration (Smith et al. 2003; Gould 2004), which is usually close to either due east or due west. This “happy coincidence” that Earth’s projected acceleration is typically aligned (or anti-aligned) with its projected velocity is due to the fact that the bulge microlensing fields lie near the ecliptic. By contrast, toward the Large Magellanic Cloud, Earth’s projected acceleration is perpendicular to its projected velocity.

The case of OGLE-2005-BLG-169 also illustrates the power of this parallax argument. Lines with a slope of -1 in Figure 1 have constant parallax, so one sees immediately that the alternate solution has $\Delta \log \pi_E = 1.18$, i.e., 15 times larger. In more detail, $M = 0.078 M_\odot$, $\pi_{\text{rel}} = 6.0 \text{ mas}$, $\boldsymbol{\mu}_{\text{rel,hel}}(N, E) = (+4.87, +5.60) \text{ mas yr}^{-1}$, and $\mathbf{v}_{\oplus,\perp}(N, E) = (+3.1, +18.5) \text{ km s}^{-1}$, together with Equation (3), imply $\boldsymbol{\pi}_E = \sqrt{\pi_{\text{rel}}/\kappa M} \boldsymbol{\mu}_{\text{rel}}/\mu_{\text{rel}} = (+0.2, -3.1)$. By contrast, Gould et al. (2006) published a 1-D parallax measurement at the time of the original discovery, $\pi_{E,\parallel} = -0.086 \pm 0.261$, which is the component of $\boldsymbol{\pi}_E$ in the direction of the

apparent (“geocentric”) acceleration of the Sun, i.e., $\psi = -79^\circ$ (north though east). By comparison, the alternate model predicts $\pi_{E,\parallel} = 0.2 \cos \psi + (-3.1) \sin \psi = +3.1$. Hence, although the original parallax “measurement” appeared to be almost completely unconstraining at the time, it rules out the alternate model in this case.

Thus, even when the parallax contours are substantially “fatter” than those shown in Figure 3 of Gould et al. (2022) (and hence are rarely published unless they are strongly inconsistent with zero, i.e., indicating very large π_E), they can still be adequate to exclude the high- π_{rel} solution. This reflects a general principle that seemingly “useless” information can suddenly be the key to unlocking a puzzle³ when new techniques become available, such as old clothing in police storage lockers after the advent of DNA testing. In particular, this emphasizes the importance of archiving final-reduction light-curve photometry of all microlensing planets.

Of course, there are some cases that the high- π_{rel} solution is correct. For reasons that are discussed further below, these are quite rare. Nonetheless, it is important to point out that this same test will typically confirm those solutions. Indeed, it is likely that in those cases, the high parallax will already have been noticed and the host will already be recognized as being of exceptionally low mass and/or nearby.

3.3. Unique Main-Sequence Solutions

For a substantial fraction of cases, Equation (5) (provided that it is restricted to main-sequence hosts) will “end” before it can intersect with the $\pi_{\text{rel}} > \pi_{\text{rel},\text{min}}$ branch of Equation (4). I will cover the case of luminous BD hosts later in this section. For the sake of discussion, I adopt $M_K = 11.0$ and $M = 0.078 M_\odot$ for a star at the hydrogen-burning threshold⁴ from Figure 22 of Benedict et al. (2016). And, for simplicity, I assume that extinction is negligible for the following example, wherein $\mu_{\text{rel,hel}} = 6 \text{ mas yr}^{-1}$, $v_{\oplus,\perp} = 30 \text{ km s}^{-1}$, $t_E = 30 \text{ day}$ (i.e., the fiducial parameters of Equations (6) and (7)), $K = 21$, $\cos \psi = 0$, and $\pi_S = 0.12 \text{ mas}$. Then, the pair $(M_{\text{host}}, \pi_L) = (0.078 M_\odot, 1.00 \text{ mas})$, corresponding to $(M_{\text{host}}, \pi_{\text{rel}}) = (0.078 M_\odot, 0.88 \text{ mas})$ is the “end point” of the mass-luminosity relation:

³“Any man can make use of the useful, but it takes a wise man to make use of the useless”, - Lao Tzu

⁴It may be that the dimmest “stars” in Figure 22 of Benedict et al. (2016) are actually relatively young BDs that are still cooling. Such young BDs are over-represented in the solar neighborhood relative to typical microlenses, which are several hundred pc from the plane. Thus, as a technical point, non-detections could be consistent with very slightly more massive BDs, e.g., $0.08 M_\odot$. The value adopted here, $0.078 M_\odot$, is adequate for the illustrations of this section.

there are no solutions with higher π_{rel} because the sources would have to be dimmer than the bottom of the main sequence. Therefore, because the minimum from Equation (6), $\pi_{\text{rel},\text{min}} = 0.95 \text{ mas}$, is already larger than this end-point value, there are no solutions on the $\pi_{\text{rel}} > \pi_{\text{rel},\text{min}}$ branch of Equation (4) for this case.

However, this argument will fail in a large fraction of cases. For example, the fiducial value $\mu_{\text{rel}} = 6 \text{ mas yr}^{-1}$ is quite typical of microlensing events, and the fiducial value $v_{\oplus,\perp}$, while also fairly typical is, in addition, the maximum possible value. Hence, one broadly expects $\pi_{\text{rel},\text{min}} \sim 1 \text{ mas}$. On the other hand, a large fraction of hosts will be brighter than the above example, i.e., $K = 21 - \delta K$, where δK is a few magnitudes. For example, an $M_{\text{host}} = 0.5 M_{\odot}$ star at $D_L = 5 \text{ kpc}$ would have $K \sim 19.5$. In such cases, the end point of the main sequence will be at $\pi_{\text{rel}} \sim (10^{\delta K/5} - 0.12) \text{ mas} \rightarrow 1.88 \text{ mas}$, so the high- π_{rel} branch will not necessarily pass “under” the end point.

Figure 1 shows three clear examples of this argument, namely, MOA-2007-BLG-400, MOA-2009-BLG-319, and MOA-2013-BLG-220. The argument clearly fails for OGLE-2005-BLG-071 and OGLE-2012-BLG-0950, for which the “two solutions” are both on the low- π_{rel} branch. In both cases, these solutions are very close to each other. These cases will be discussed in greater detail further below. Finally, if one could really assume zero errors, the argument would apply to OGLE-2005-BLG-169. However, as discussed above, this application is marginal, and, in practice, one must consider the alternate solution.

Moreover, even when this argument does successfully exclude the alternate high- π_{rel} solution for main-sequence hosts, it will still always permit a high- π_{rel} BD host. The first point is that the entire “basic method” depends on the existence of a mass-luminosity relation that is approximately independent of other parameters, in particular, age and metallicity. The K -band relation is approximately independent of metallicity. And, as I will now discuss, it is also basically independent of age for (unevolved) main-sequence stars. This would not quite be true of M dwarfs, particularly late M dwarfs, which can take several 100 Myr to reach the zero-age main sequence. However, the great majority of lenses are either in the bulge or are several hundred pc from the Galactic plane, where such young stars are exceedingly rare. Thus, this age dependence can usually be ignored.

However, it cannot be ignored for alternate, high- π_{rel} solutions because these are close to the Sun and so, given their low Galactic latitude, also close to the Galactic plane, where young stars are more plentiful. And this means that one must consider cooling BDs as well.

The main argument against such solutions, assuming that they cannot be excluded by geocentric proper-motion or microlens-parallax arguments (Sections 3.1 and 3.2), is statistical. In addition to general statistical arguments favoring distant over nearby lenses for

discrete degeneracies (e.g., Gould 2020), these BD solutions are possible for only a brief range of ages for each of a narrow range of masses.

In brief, there are two broad classes of this discrete degeneracy: one in which the mass-luminosity relation (Equation (5) intersects the high- π_{rel} branch of Equation (4) while it is still on the main sequence) and the other where the intersection would indicate a cooling BD. The μ_{rel} (Section 3.1) and π_{E} (Section 3.2) arguments can be applied against either class and will likely rule out the great majority of the high- π_{rel} solutions. For the few remaining events, those that are in the second class, will be strongly disfavored by probabilistic arguments.

3.4. Decisive Resolution by Extra Observations

For any particular case, it is straightforward to decisively resolve the degeneracy between nearby and distant solutions by performing two epochs of late-time AO observations instead of one. A total of three epochs is all that is required to measure the heliocentric lens-source relative proper motion and parallax, $\boldsymbol{\mu}_{\text{rel, hel}}$ and π_{rel} . These could be t_0 (when the lens and source are known to have essentially zero offset) and two epochs, say in April and September, many years later. These would be sufficient to distinguish between small π_{rel} and the values $\pi_{\text{rel}} \gtrsim 1$ mas that are typical of the high- π_{rel} solutions. The decision on whether to make such additional observations will depend on the required purity of the sample for deriving statistical conclusions about planets. At present, it appears that of order 80% to 90% of the planets with large high- π_{rel} alternate solutions will be decisively resolved by the methods of Sections 3.1 and 3.2), while the statistical uncertainty of the remainder will be small. However, if greater purity is desired, then this method remains available.

Another method, which also requires an extra observation but does not require any special timing, is to observe the source in a second, substantially bluer band, e.g., J -band. The high- π_{rel} solution will almost always have substantially lower mass and hence be substantially redder. In some cases of high-extinction fields, the lower predicted extinction at the higher π_{rel} might effectively cancel this intrinsic difference, but this will be rare and, moreover, such wasted observations can easily be avoided by predicting the observed colors of the two solutions in advance.

This color method is, in fact, the third one that can be applied to the case of OGLE-2005-BLG-169. I considered only K -band observations when I constructed Figures 1 and 2 because I wanted to focus on issues related to the “basic method”. However, several of these events were observed in two or more bands, including OGLE-2005-BLG-169, which was observed in optical bands using *HST* by Bennett et al. (2015). Their resulting solution was consistent

results with the one derived by Batista et al. (2015) based on Keck IR observations, while these would have been totally inconsistent if the alternate solution had been correct.

Thus, while Batista et al. (2015) and Bennett et al. (2015) did not explicitly consider the alternate solution, they did explicitly remark on all three of the arguments that objectively rule it out: agreement with the Gould et al. (2006) proper-motion measurement (Section 3.1), consistency with the Gould et al. (2006) parallax measurement (Section 3.2), and consistency between results obtained in red and blue bands (Section 3.4).

3.5. Remaining Problematic Cases

The main source of problematic cases will be events with low $\mu_{\text{rel, hel}}$, which will have strong overlap with members of the input sample that have small μ_{rel} (if known). While low, e.g., $\mu_{\text{rel}} < 2 \text{ mas yr}^{-1}$, events are expected to be rare ($p \sim (2/2.9)^3/6 \sqrt{\pi} \sim 3\%$, Gould et al. 2021), planetary events with $\mu_{\text{rel}} < 2 \text{ mas yr}^{-1}$ appear to occur at a higher rate. For example, of the 71 planetary events with proper-motion measurements that are examined in Section 6, 9 have $\mu_{\text{rel}} < 2 \text{ mas yr}^{-1}$, of which 2 have $\mu_{\text{rel}} < 1 \text{ mas yr}^{-1}$, compared to the 2.0 and 0.25 that would be expected if planetary events followed the underlying event distribution. However, there is a significant selection bias toward lower μ_{rel} for events with detectable planetary anomalies because, other event characteristics being equal, $\Delta\chi^2 \equiv \chi^2(1\text{L1S}) - \chi^2(2\text{L1S}) \propto \mu_{\text{rel}}^{-1}$. See Section 6.3. Here $nLmS$ means n lenses and m sources.

Assuming that these events prove to have $\mu_{\text{rel, hel}} \sim \mu_{\text{rel}}$, then from Equation (6), they would have $\pi_{\text{rel, min}} \lesssim 0.3 \text{ mas}$. It might still be that the actual lens was in or near the bulge, in which case the alternate solution would still have very large π_{rel} and so would be susceptible to the various rejection arguments given above. However, it is also possible (if less likely) that the actual lens had $\pi_{\text{rel}} \sim 0.35 \text{ mas}$ in which case the alternate solution might have $\pi_{\text{rel}} \sim 0.25 \text{ mas}$. In this case, it might be very difficult to apply either of the methods from Sections 3.1 and 3.2, and the statistical arguments would likewise fail. Moreover a reliable measurement of the difference in trigonometric parallaxes, i.e., 0.1 mas , would probably require extraordinary effort.

4. False Positives

In Section 3, I showed that if two stars are detected in a single epoch of late-time AO follow-up imaging, and *if these stars are actually the microlensed source and the host*, then one can make unambiguous host mass and distance determinations in the great majority of

cases and can make strong statistical arguments regarding these determinations in most of the remaining cases.

However, the inference that the star identified as the host is in fact the host is far from trivial. Logically, there are four broad outcomes from a first epoch of late-time imaging: either zero, one, two, or more than two stars are detected in the neighborhood of the anticipated target. I mention zero detections only for completeness: it is very difficult to imagine the circumstances under which a source that was detected (even highly magnified) by a 1.6m optical telescope, could fail to appear in an 8m (or 30m) *K*-band image (other than if a brighter star were superposed, in which case there would still be at least one star detected in the image).

For this reason, if only one star is detected, it is almost certainly the source (or a brighter companion of the source). The main potential reasons for this would be that the host has not separated sufficiently to be seen due to the glare of the source (which could be quite severe if it is, e.g., a giant), or the host is dark (BD, WD, NS, or BH). The specific circumstances, in particular whether there was a geocentric proper-motion measurement, would have to be evaluated to determine whether to wait for another observation or to conclude that the host was dark.

If more than two stars are detected, then some additional work (possibly including additional observations) is required to determine which among these several stars is the source and which is the host. I discuss this in Section 4.5.

In this section, I focus on the case that exactly 2 stars are detected. The principal operational issue is that, assuming one can confidently identify which is the source, one can, in principle, proceed to directly apply the “basic method” of Section 2 to measure the host mass and distance. Then, for the case that the “host” is actually a false positive, these measurements will, in fact, be incorrect. Thus, the main questions are: how likely is this to occur, under what conditions will there be “warning signs” that the measurements are incorrect, is the frequency of undetected “bad measurements” at an acceptable level, and, finally, if not, what can be done to reduce the frequency of “bad measurements”?

In general, for the case that two stars are detected, a “false positive” requires two conditions: first, the true host is not detected, and second, some other star is detected. Logically, there are only three choices for the “other star”: a companion to the host, a companion to the source, and an unrelated field star.

When concrete scenarios are needed, I will assume that the late-time AO observations are made by MICADO in the *K*-band, on the 39m European Extremely Large Telescope (EELT). Hence, I will assume that the images have a FWHM $\theta_{\text{FWHM}} = 14 \text{ mas}$. The implications

would not be qualitatively different if I were to use the 25m Giant Magellan Telescope (GMT), with $\theta_{\text{FWHM}} = 22 \text{ mas}$. However, it is important to note that substantial initial progress can be made toward the goals outlined in this paper using present-day, 8m class, telescopes, whose imaging characteristics are very different. Nevertheless, most questionable cases can only be resolved using next-generation telescopes, so my assumption is relevant to the final resolution. Moreover, I do not want to clutter the exposition with many different cases, and I therefore rely on the reader to adapt the reasoning presented here to other particular observational configurations and strategies.

4.1. Stellar Companion to the Host

Among the three possible causes of false positives, the one most likely to corrupt the “basic method” of Section 2 will be companions to the host that are heavier and more luminous than the host. Such configurations can easily account for *both* the presence of a star other than the host *and* the failure of the host star to appear.

To give a concrete sense of the problem, let us imagine that an $M_{\text{host}} = 0.9 M_{\odot}$ G dwarf is detected 10 years after the event at 50 mas from the source. I will further specify that this star is at $D_L = 5 \text{ kpc}$. The first point is that if the G dwarf is the host, then the “basic method” will (approximately) yield the correct mass and distance of this star. However, if this G dwarf is a companion to the true host, which is an $M_{\text{host}} = 0.4 M_{\odot}$ M dwarf, then the solution generated by Equations (4) and (5) will be wrong for two reasons. First, the inferred $\mu_{\text{rel, hel}}$ will be incorrect, and second, the “ M_{host} ” entering the two equations will be different. Thus, there is a good chance that we would not even realize that this was in fact a “G dwarf”.

Nevertheless, as an all-knowing outsider to this process, I can ask: “given that there is a G dwarf at 50 mas from the source, what is the chance that it gave rise to the observed microlensing event”, which took place 10 years earlier? According to Duquennoy & Mayor (1991), about 40% of G dwarfs do not have stellar companions. For this class, the probability that the G dwarf was the host is 100%. The remaining 60% of G dwarfs have companions at various mass ratios and periods. However, those with separations $\Delta\theta \gtrsim 4\theta_{\text{FWHM}} \sim 60 \text{ mas}$, corresponding to projected separations $a_{\perp} \gtrsim 300 \text{ au}$, and so periods $\log P/\text{day} \gtrsim 6.4$, would have been seen regardless of mass (unless they were BDs, WDs, NSs, or BHs). This corresponds to about 35% of those with companions. Another 25% have periods $\log P/\text{day} < 4.0$, in which case they would have given rise to noticeable binary-lens effects in typical planetary microlensing events (which have higher magnifications than average). Thus, only $40\% \times 60\% = 24\%$ of G dwarfs have companions that could have escaped detection during

both the microlensing event and during the AO follow-up observations. However, those that do escape detection are very good candidates for the host. That is, each component of a stellar binary has a probability to generate a microlensing event proportional to its θ_E , i.e., to the square root of its mass. So, for typical mass ratios of a G-dwarf companion, $Q \sim 0.5$, the probability that the companion was responsible for the microlensing event is $\sqrt{Q}/(1 + \sqrt{Q}) \rightarrow 40\%$. Hence, before considering other mitigating factors, the overall probability of a false positive for this G-dwarf example is about 10%.

Nevertheless, there are two potential methods for recognizing the presence of such a false positive. Moreover, I will show that the G-dwarf example is unrepresentative of the general case and is more adverse than typical cases.

First, as discussed in Section 3.1, about 2/3 of planetary events will have good (e.g., 10%) measurements of μ_{rel} . While $\mu_{\text{rel}} \neq \mu_{\text{rel, hel}}$, a difference of e.g., 25% would raise a “red flag”. In the above example, the region immune to such red flags would be an annulus from 37 mas to 63 mas from the source, compared to the 60 mas radius from the observed G dwarf, within which the true host could be “hiding”. That is, only about 25% of this region would fail to trigger a red flag. Note that if a red flag were triggered, this would still not yield an accurate mass measurement, but it would trigger an additional investigation, which I discuss in Section 4.5.

Second, it is possible that the original light curve contains substantial parallax information. Recall that this information is normally highly directional in nature, so it could reveal strong conflicts with the measured direction of $\boldsymbol{\mu}_{\text{rel, hel}}$ even if it, by itself, provided no constraint on the lens mass. Unfortunately, however, the fraction of events with such parallax constraints is relatively small, and to be conservative, I ignore this channel in my assessment of the robustness of the method.

Thus, for single-epoch detections of G dwarfs as the putative host, I conclude that of order 10% of events without ρ measurements and of order 3% of events with ρ measurements will be corrupted by binary companions and will escape any red flags that would alert us to this corruption.

As I discuss in Section 4.5, one can easily vet these alerts by taking an additional AO image after several years. Because these alerts will arise in only a small minority of all events, they can be acted upon at small fractional cost in the observing time of the overall program.

We do not expect that a major fraction of the detected “putative hosts” will be G dwarfs. Microlensing is intrinsically sensitive to stars in proportion to their Einstein radii, $\theta_E = \sqrt{\kappa M \pi_{\text{rel}}}$, and hence, $\propto M^{1/2}$. As there are vastly more M dwarfs than G dwarfs, there are also vastly more M-dwarf than G-dwarf events. For a sample of planetary events (i.e.,

the current focus), the bias toward M-dwarf events is expected to be less severe because, it is currently believed (based on planets that are much closer to their hosts than microlensing planets), that more massive stars host more planets. Nevertheless, we still expect that the majority of hosts will have lower mass than G dwarfs. And, while of order half of all G dwarfs have M dwarf companions, only a small fraction of M dwarfs have G dwarf companions (simply because there are far more M dwarfs overall). Thus, the typical detected “putative hosts” will be K and M dwarfs, for which the fraction with companions is lower than described in the above G-dwarf example.

Overall, I conclude that unrecognized corruption of the sample by luminous binary-star companions will be a small, though non-negligible effect. I discuss how the contamination of the sample can be further greatly reduced in Section 4.5.

4.2. Stellar Companion to the Source

The great majority of microlensed sources from ground-based surveys are either on the upper main sequence or are evolved stars. Hence, they are of order $\sim 1 M_{\odot}$ and so have companion distributions similar to G dwarfs. Hence, source companions will populate the field in a manner very similar to the above G-dwarf example. However, their path to becoming false positives is substantially different than for host companions.

I first consider the case (about 2/3 of all planets) for which there is a good ρ measurement. Again I use the example that $\mu_{\text{rel}} = 5 \text{ mas yr}^{-1}$ with an error of about 10% and that the observation is taken 10 years after the event. Hence, I adopt a “permitted range” of $\pm 25\%$, i.e., $37 \text{ mas} < \Delta\theta < 63 \text{ mas}$ for an observed source companion to be mistaken for the host. This corresponds to periods $6.40 \lesssim \log(P/\text{day}) \lesssim 6.75$. Only about 4% of G dwarfs have companions in this period range. In addition, if this source companion is to be mistaken for the host, the host itself must be absent. This can occur only if the host is dark or if it is sufficiently close to the source companion to disappear in its glare. Because (in contrast to the host-companion scenario of Section 4.1) the source companion is drawn randomly from the mass-ratio distribution, I adopt a 25 mas radius typical black-out zone. Thus, in this example, only about $(2 \times 25)/(2\pi \times 50) \sim 16\%$ of luminous hosts would be successfully blocked out. Hence, the source-companion channel of false positives is about 1% (for the case that ρ is measured during the event).

Next I consider the remaining 1/3 of planetary events for which ρ is not measured. Before proceeding with this analysis, I note that a single late-time observation will yield a very precise measurement of the source position. This can be combined with a measurement

of the source position at the time of the event (based on difference images), which normally has a precision of about 10 mas, to yield a source proper motion measurement with precision $\sigma(\boldsymbol{\mu}_S) \sim 1 \text{ mas yr}^{-1}$. This greatly restricts the domain of plausible $\boldsymbol{\mu}_{\text{rel, hel}}$ relative to the case that $\boldsymbol{\mu}_S$ is unknown. In practice, one would solve Equations (4) and (5) under the assumption that the detected star was the host and ask whether the resulting transverse velocity of the lens was consistent with known Galactic populations. For example, suppose that, in the solution, $\pi_{\text{rel}} \simeq 10 \mu\text{as}$ (implying that the lens was almost certainly in the Galactic bulge) and $\boldsymbol{\mu}_S \simeq 0$ in the bulge frame. Then observed values of $\mu_{\text{rel, hel}} > 6 \text{ mas yr}^{-1}$, i.e., $\Delta\theta > 60 \text{ mas}$ would be regarded as suspicious, while $\Delta\theta < 14 \text{ mas}$ would be unobservable. Only 9% of G-dwarfs have companions in the remaining region. And only about 1/4 of these would succeed in “blacking out” the actual host. Hence, while contamination by unflagged false positives for the case of unmeasured ρ is a factor several higher than the measured- ρ case, it is still very small.

4.3. Random Field Stars

In principle, if there is one star observed (in addition to the source), it could be a random field star. To evaluate this possibility, I normalize this population to the source binary-companion distribution just analyzed. Holtzman et al. (1998) report that there are 4.2 stars arcsec^{-2} with $M_I \leq 9$ toward Baade’s Window, which corresponds to $M \gtrsim 0.25 M_\odot$, while Duquennoy & Mayor (1991) report that G dwarfs have an average of 0.56 companions in this mass range. Based on the clump-giant surface densities reported by Nataf et al. (2013), I find that microlensing planets typically lie in fields with 2–3 times the surface density of Baade’s Window. Therefore, the frequency of source companions is comparable to the frequency of random field that lie within 0.053 arcsec^2 , i.e., a circle of radius 130 mas. Thus, it will be somewhat less common to find field stars at the separations in the typical range of interest than to find binary companions to the source. As I have already shown that the latter present a relatively minor problem, I do not rehearse the details of that analysis as applied to random field stars.

4.4. Confusion Between Source and Host

In all the preceding analyses, I have implicitly assumed that if exactly two stars are detected, then it will be clear which is the source. For the great majority of cases, the source K -band magnitude can be predicted from the source I -band magnitude, which is usually well measured during the event, and the source $V - I$ color. This is often well measured,

but if not, it can be estimated from the source magnitude together with the Holtzman et al. (1998) color-magnitude diagram (CMD). Then, in most cases, one of the two observed stars will have approximately this brightness, while the other will be very different.

However, confusion may be possible for two reasons. First, the source and host may be of comparable brightness. Second the source may have a close companion that is not separately resolved, so that the “star” at the source location is much brighter than the source. For example, a companion at $a_{\perp} \sim 15$ au would be separated by ~ 2 mas. The fact that there were two stars would not leave any detectable trace on the AO imaging, while (barring rare geometries) the source companion would not leave any discernible trace on the microlensing event.

I now show that the cases for which this cannot be resolved with good confidence are rare and that the practical impact of the remaining cases is small.

The first point is that, as mentioned above, the proper motion of each star can be measured separately in the bulge frame from their positional offsets relative to the precise (difference image) measurement of their position at t_0 . For the case that the lens is in the disk, this measurement will often identify it as a disk star. Second, there will sometimes be directional information from the microlens parallax, although this will be relatively rare. Third, it is actually mainly for nearby disk lenses (i.e., just those that are most easily resolved kinematically) that the problem of comparable brightness arises. That is, source stars are typically upper-main-sequence or evolved stars in the bulge. It would be rare that a bulge host would be as luminous in K as an upper-main-sequence star and extremely rare to be as luminous as a sub-giant star. On the other hand, a host at $D_L = 4$ kpc or $D_L = 2$ kpc would gain an advantage of 1.5 or 3 magnitudes from smaller distance modulus. Hence, at these two distances, respectively, early and middle M-dwarf hosts would have comparable brightness to G-dwarf sources. Fourth, as source stars are usually bright, the chance that they will have still brighter companions is small. For example, Duquennoy & Mayor (1991) find that only 4.6% of G dwarfs have companions of comparable or greater mass.

Finally, we should ask how the estimates of the host mass and system distance would be affected if the wrong identification were made. There would be two effects. First, obviously, the source brightness would be attributed to the host, which would impact Equation (5). Second, the heliocentric relative proper motion would be assigned opposite sign: $\boldsymbol{\mu}_{\text{rel, hel}} \rightarrow -\boldsymbol{\mu}_{\text{rel, hel}}$. Hence, the quantity entering Equation (4) would transform $|\boldsymbol{\mu}_{\text{rel, hel}} - \mathbf{v}_{\oplus, \perp} \pi_{\text{rel}}/\text{au}| \rightarrow |\boldsymbol{\mu}_{\text{rel, hel}} + \mathbf{v}_{\oplus, \perp} \pi_{\text{rel}}/\text{au}|$. Because the second term in these expressions is usually small compared to the first, this usually would be a minor issue. However, in the great majority of cases, the whole problem originates from the fact that the host and source have comparable brightness. Hence, the fact that one has mistaken the source for the host does not have a major impact

on this estimate. And, because the issue is mostly resolved for nearby (i.e., large π_{rel}) hosts, the error in Equation (4) induced by reversing the sign of $\boldsymbol{\mu}_{\text{rel, hel}}$ is small.

4.5. Second Epoch of Late Time AO Observations

In my view, the statistical uncertainties induced by the various effects discussed in Sections 4.1–4.4 on the final results, e.g., planetary mass function and 2-D planet+host mass distribution, are likely to be modest. Hence, reliable results can be obtained by following a general policy of obtaining a single epoch of late-time K -band imaging. However, there will be, as I have discussed, a significant minority of individual cases that will be flagged for further investigation, and most of these would greatly profit by making an additional AO observation after two or so years.

Comparison of the two images would immediately give an independent measurement of the relative proper motion of the two observed stars, regardless of their relation to the microlensing event. If the “putative host” were actually a companion to the source, then this relative proper motion would be essentially zero, which would directly contradict the tentative conclusion that its displacement from the source represented host-source relative proper motion.

Similarly, if the “putative host” were in fact a random field star, its *vector* proper motion relative to the source would almost certainly be inconsistent with the result derived from their first-epoch separation. That is, with precise astrometric measurements, the chance for agreement in one dimension is already small, but it is negligible in two dimensions.

For the great majority of the cases for which the “putative host” was a companion to the host, the second measurement would immediately make this clear. Combining the putative-host/source relative proper motion derived from the two epochs with the putative-host position in the first, one could derive the position of the putative host relative to the source at t_0 , likely with errors of order 1 mas. In almost all cases, this separation would be much larger than 1 mas because such a close companion would have given rise to strong microlensing effects during the event. Thus, the fractional error in the projected angular separation between the host and its companion would be small. Unfortunately, this additional information would not help break the mass-distance degeneracy, although it would give a measurement of $\boldsymbol{\mu}_{\text{rel, hel}}$ and so (via Equation (4)) a good estimate of θ_E , which would be especially important for events without a ρ measurement. Note that in most cases, the internal motion of this binary would be very small compared to its motion relative to the source.

At this point, there would be three choices: drop the event from the sample, include it as a probabilistic measurement with two constraints (θ_E and upper limit on the K -band flux), or perform further investigatory work. This might include taking substantially deeper images in the hope of detecting the host or a spectrum of the companion to the host. Such a spectrum (combined with the K magnitude) could give a reasonable good estimate of the system distance. Combining this with the θ_E measurement would then yield the host mass.

Because each of these cases (companion to host, companion to source, and random field star) would be resolved individually by a second AO epoch, it follows immediately that all such possibilities would be resolved simultaneously for the case that more than two stars were detected.

If the late-time imaging were done in a second band, e.g., J , then it could also aid in resolving the issues of confusion between the source and host. Of course, before conducting such observations, one would have to assess that it would be likely to re-detect the host, particularly if it were faint and red and/or the field had high extinction. However, if feasible, measurements of the $(J - K)$ colors of the two stars, combined with an empirical IJK color-color diagram, would allow precise predictions of their I -band magnitudes, which could then be compared with the one derived for the source during the event. Moreover, such J -band second epochs would be generally useful, as they would allow for an independent check on the mass and distance estimates from the “basic method”.

There is another class of events for which such a $(J - K)$ measurement of the source could be useful. For some high-magnification events, the product of the source flux and the Einstein timescale, $f_S t_E$ is much better measured than either parameter separately. For such events, $t_q \equiv q t_E$ is also usually an invariant (Yee et al. 2012). If I_S were determined from the J and K measurements (as just described), this would then both greatly reduce the uncertainty in t_E , which enters the host-mass determination via Equation (4), and reduce the uncertainty in q (and hence in $M_{\text{planet}} = q M_{\text{host}}$).

Finally, late time images, particularly in a second band, such as J , could clarify the small subset of cases for which the source is corrupted by a nearby (i.e., unresolved) companion. If the companion is as bright or brighter than the source, then it will substantially change the measured flux of the (apparent) source. However, even if the companion is a magnitude or so fainter than the source, it can still affect the astrometry. For example, at a separation of 10 mas and at 1 magnitude fainter, such a companion would most likely not be separately resolved and would displace the measured “source” position by about 3 mas. Moreover, the ~ 0.35 mag “excess” in K -band flux might also escape notice, depending on the precision of the original light-curve modeling. Then one might, at least initially, attribute this astrometric offset to a binary companion to the host. In fact, such a small offset would almost certainly be

ruled out by the lack of binary-microlensing signatures in the original light curve, as discussed above. However, much larger offsets are possible if the source companion is brighter than the source.

Such large excesses in the (apparent) source flux would, in most cases, be easily recognized from the prediction of K_S flux (from I_S and $(V - I)_S$). However, if $(V - I)_S$ was not measured or was poorly measured, then a late-time $(J - K)$ color could determine whether the measured K flux was indeed excessive.

5. Analytic Error Estimates

In this section I give analytic error estimates for the measurements of M_{host} and D_L due to measurement uncertainties in t_E , and theoretical uncertainties in the π_S (equivalently, D_S), in the extinction profile $A_K(\pi_L)$, and in the mass-luminosity relation $M_K(M_{\text{host}})$. I initially assume (as will usually be the case) that the errors in the measurements of the observed flux, K , and in $\boldsymbol{\mu}_{\text{rel, hel}}$ are small. However, I subsequently address the impact if they are not.

The purpose of these estimates is to facilitate comprehensive understanding of the measurement process. They should not be applied to determine the error bars of actual measurements. Rather these should be determined, as I outline below, by standard Bayesian procedures. In particular, I will adopt simplified forms of the analytic equations in order to make them more intuitively accessible. Moreover, the approach given here ignores the constraints that arise from the measurements of the source and lens kinematics, which can reduce the size of the error bars in some cases. That said, I believe that this approach yields approximately correct error estimates for the great majority of cases.

I begin by solving Equation (4) for π_{rel} and substituting it into Equation (5), which yields an equation for K as a function of M_{host} (plus several parameters and functions). Strictly speaking this would lead to two equations, one for each branch. However, I simplify Equation (4) by setting $\mathbf{v}_{\perp, \oplus} \rightarrow 0$. This is not strictly necessary from a mathematical standpoint, but it makes the results much more transparent. It has little practical impact in most cases because the second term in this equation is usually small. There is an important subclass of events for which this is not a good assumption. However, this subclass is most easily identified by considering the simplified formalism, and it is best addressed separately. See Section 5.5. I also suppress the subscript “host” on M in the interests of readability.

This yields

$$K = M_K(M) - 5 \log\left(\frac{\pi_L}{\text{mas}}\right) + 10 + A_K(\pi_L); \quad \pi_L = \frac{(\mu_{\text{rel, hel}} t_E)^2}{(1+q)\kappa M} + \pi_S. \quad (9)$$

For purposes of this section, I adopt the Baraffe et al. (2015) 1-Gyr, solar-metallicity K -band isochrone, which is illustrated in Figure 3. Note that over the mass range $-0.4 \gtrsim \log(M/M_\odot) \gtrsim -0.9$, the K -band mass-luminosity relation is given by $M_K = 4.32 - 5 \times \log(M/M_\odot)$, i.e., $L_K \propto M^2$. Because this will play an important role in the error analysis, it is worthwhile to remark on the origins this “episode” of power-law behavior in the mass luminosity relation.

Because $M \propto R$ for main-sequence stars, this power-law region can be expressed as $L_K \propto R^2$, i.e., constant surface brightness (in the K band) as the mass changes. Physically, this implies constant temperature. Indeed, one finds from the Baraffe et al. (2015) isochrones that the temperature evolves slowly in this interval, although it is not strictly constant. From a stellar interiors point of view, this nearly constant temperature arises from a fully convective interior supported by ideal-gas pressure, $P = nkT$. Starting at about $M \sim 0.35 M_\odot$ the radiative zone gradually expands (until convection is eliminated at about $M \sim 1.3 M_\odot$). Below about $M \sim 0.13 M_\odot$, stars are increasingly supported by degeneracy pressure (until this becomes dominant in the BD regime, $M \lesssim 0.075 M_\odot$).

I begin by finding the change δK from a combination of small changes δM , $\delta \pi_S$, and δt_E

$$\delta K = \frac{\partial K}{\partial M} \delta M + \frac{\partial K}{\partial \pi_S} \delta \pi_S + \frac{\partial K}{\partial t_E} \delta t_E \quad (10)$$

where

$$\frac{\partial K}{\partial M} = M'_K + Z \frac{\pi_{\text{rel}}}{M}; \quad \frac{\partial K}{\partial \pi_S} = -Z; \quad \frac{\partial K}{\partial t_E} = -2Z \frac{\pi_{\text{rel}}}{t_E}; \quad Z \equiv \frac{5}{\pi_L \ln 10} - A'_K. \quad (11)$$

5.1. Error Induced by π_S

I evaluate the effect of an error $\delta \pi_S$ by considering all other parameters and functions to be correct and finding the required change in M to enforce $\delta K = 0$:

$$\frac{\delta M}{M} = \frac{\delta \pi_S}{\pi_{\text{rel}} + (M/Z)M'_K}. \quad (12)$$

As I now show, the role of $A'_K(\pi_L)$ is small, and therefore, in order to facilitate analytic treatment, I set $A'_K \rightarrow 0$ (i.e., $Z \rightarrow 5/(\pi_L \ln 10)$). First, a substantial majority of lenses are

behind nearly all the dust, in which case A'_K is negligibly small. Second, for very nearby lenses ($D_L \lesssim 1$ kpc), $dA_K/dD_L \sim 0.1/\text{kpc}$, so that the ratio of the extinction term to the distance term in Z is $\sim (0.1/\text{kpc})/[5/(\ln(10)D_L)] \simeq 0.046(D_L/\text{kpc})$. For typical lines of sight, the relative effect peaks at about $D_L \sim 3$ kpc, where $dA_K/dD_L \sim 0.05/\text{kpc}$, so the ratio is about 7%. While the effect of dust certainly cannot be excluded from mass and distance estimates, its impact on the errors in these quantities (the focus of the present section) is almost always small, and so can be ignored. I note, however, that the sign of the effect of ignoring the dust is to slightly underestimate the size of the errors (typically by a few percent). That is, at fixed θ_E , the predicted flux of the lens $F \propto L/D^2$ will increase with distance because its increasing luminosity, L , (from higher mass) dominates over the distance term in the denominator. This increase is reduced by the increasing column of dust with distance, thus reducing the leverage of the K -band flux measurement.

After a small amount of algebra, Equation (12) then becomes

$$\frac{\delta M}{M} = \frac{-\delta\pi_S}{\pi_S + H(M)\pi_L} = \frac{\delta D_S}{D_S} \left[1 + \frac{D_S}{D_L} H(M) \right]^{-1}; \quad H(M) \equiv -\frac{1}{5} \frac{dM_K}{d \log M} - 1. \quad (13)$$

The function $H(M)$ is shown in Figure 5, as calculated from the online discrete representation of the Baraffe et al. (2015) isochrones. I note that these isochrones are in excellent agreement with the high-precision M-dwarf mass measurements of Benedict et al. (2016) over the mass range $0.1 < M/M_\odot \lesssim 0.45$. However, Benedict et al. (2016) show a cluster of 5 stars near $M \sim 0.6 M_\odot$ that lie about 0.15 mag below the Baraffe et al. (2015) prediction. Reconciliation of these details, as well as precision testing of the Baraffe et al. (2015) isochrones for $0.6 \lesssim M/M_\odot \lesssim 0.9$, should be carried out before employing them in practice. However, from the present perspective, I am only concerned with the general form of $H(M)$. The main features are that

$$H(M) \simeq 0 \quad (0.13 < M/M_\odot < 0.4), \quad (14)$$

and that it rises toward both lower and higher masses. Adopting $\sigma(D_S)/D_S \sim 12\%$ for typical lines of sight, one sees that the error induced by this uncertainty in D_S is a maximum in the mass range shown in Equation (14), where it is $\sigma(M)/M \sim \sigma(D_S)/D_S \sim 12\%$, and that it is substantially smaller away from this mass range.

Using $\delta\pi_{\text{rel}} = -\pi_{\text{rel}}(\delta M/M)$ and $\delta\pi_L = \delta\pi_{\text{rel}} + \delta\pi_s$, one obtains

$$\frac{\delta D_L}{D_L} = \frac{\delta D_S}{D_S} \frac{1 + H(M)}{1 + H(M)(D_S/D_L)}. \quad (15)$$

Hence, for bulge lenses ($D_L \sim D_S$), the error in D_L is essentially the same as the error in D_S (as one would naively expect) and, in particular, is independent of the mass. For disk lenses, the fractional error in D_L is the same as that of D_S for the mass range shown in Equation (14), while it is lower for other masses (because $H(M) > 0$ and $D_S/D_L > 1$).

5.2. Error Induced by t_E

Before beginning, I note that the fractional errors in t_E that are derived from microlensing light curves cover a very wide range, from $< 1\%$ to several tens of percent. In the former case, their impact on the errors in M_{host} and D_L are negligible compared to those of uncertainties in other quantities, such as D_S . In the latter, the present perturbative approach cannot fully capture their impact. Furthermore, as I detail below, there can be additional information that is not captured by this formalism and that can substantially reduce the impact of the t_E errors.

From Equation (11), $\partial K/\partial t_E = 2(\pi_{\text{rel}}/t_E)(\partial K/\partial \pi_S)$. Hence, we can immediately transform Equation (13) to obtain

$$\frac{\delta M}{M} = \frac{-2(\delta t_E/t_E)\pi_{\text{rel}}}{\pi_S + H(M)\pi_L} = -2\frac{\delta t_E}{t_E} \frac{1 - (D_L/D_S)}{H(M) + (D_L/D_S)}. \quad (16)$$

For bulge lenses ($D_L \sim D_S$), the impact of the t_E errors on the mass estimate is very small. The physical reason is clear: if the host is approximately at the bulge distance then the measurement of K directly gives the mass, without any significant input from the θ_E determination. However, for disk lenses, the impact can be far larger, particularly for those in the mass range of Equation (14), for which Equation (16) yields $\sigma(M)/M \rightarrow 2[\sigma(t_E)/t_E](D_S/D_L - 1)$. This can be quite problematic for events with large fractional errors in t_E .

The fractional error induced in D_L is

$$\frac{\delta D_L}{D_L} = 2\frac{\delta t_E}{t_E} \frac{[1 - (D_L/D_S)]^2}{H(M) + (D_L/D_S)}, \quad (17)$$

i.e., smaller than Equation (16) by a factor $[1 - (D_L/D_S)]$.

I note that the late-time AO measurement of $\mu_{\text{rel,hel}}$ can substantially improve the determination of t_E relative to what was possible based on the microlensing light curve alone. For high-magnification events of faint sources, $t_* \equiv \rho t_E$ may be well-measured (an invariant), even if ρ and t_E have large errors because this “source self-crossing time” is directly constrained by the interaction of the source with the caustic. If we, for the moment, ignore the difference between $\mu_{\text{rel,hel}}$ and μ_{rel} , then the angular source size is given by the product $\theta_* = \mu_{\text{rel,hel}} \times t_*$, both of which are well-measured. However, θ_* is related to the dereddened source color and magnitude $[(V - I), I]_{S,0}$ by $\theta_* \propto 10^{-I_{S,0}/5} G(V - I)_{S,0}$ where G is a known, empirically determined function. Thus, $I_{S,0}$ can be determined. Then, inverting standard procedures (e.g., Yoo et al. 2004), one can determine the instrumental magnitude I_S , using the intrinsic magnitude of the clump (from Table 1 of Nataf et al. 2013) and the

location of the clump on an instrumental CMD. This equivalently yields the source flux, f_S in the instrumental system. For such high-magnification events with invariant t_* , it is also the case that $f_S t_E$ is an invariant (Yee et al. 2012). Hence, because f_S is well-determined, so is t_E . For an actual event, the correction from heliocentric to geometric proper motion would have to be included, but in only rare cases would this significantly undermine the above logic.

In the cases for which t_E is poorly measured but $f_S t_E$ is an invariant, one can also strongly constrain t_E by “directly” measuring f_S . In fact, this cannot be done within the context of the “basic method” (i.e., single, late-time K -band image) because, in order to infer f_S in the I -band from K -band photometry, one also needs photometry in a second band that is closer to I , e.g., J . However, it is a broadly applicable approach, if it is needed.

This again emphasizes the importance of evaluating the mass and distance in the context of a full Bayesian analysis, including taking account of the correlations in the microlensing light-curve parameters, including especially those between f_S , t_E , ρ , and q . This is particularly important if the fractional error in t_E is large. For these cases, it is probably fine to use the invariant quantities and their error bars if these are reported in the original paper. If not, they should be re-derived from new light-curve modeling.

Finally, I note that the most difficult cases, i.e., nearby lenses in the mass range of Equation (14), are also intrinsically rare (because they occupy little phase space) and are the most accessible to other constraints and measurements. For example, a host at $D_L \sim 2$ kpc and at the bottom of this mass range would have $K_{\text{host}} \sim 19$ and a large lens-source relative parallax, $\pi_{\text{rel}} \sim 0.4$ mas, making it susceptible to a precise trigonometric parallax measurement. Indeed, its microlensing parallax would also be large, $\pi_E \sim 0.6$, implying that it was likely to have been measured during the event, a measurement that could be greatly improved by imposing the directional constraint from the late-time measurement of $\boldsymbol{\mu}_{\text{rel, hel}}$. Finally, such “bright” (by 30m standards) hosts would be good spectroscopic targets.

5.3. Errors Induced by $M_K(M_{\text{host}})$ and $A_K(\pi_L)$

Because $M_K(M_{\text{host}})$ and $A_K(\pi_L)$ are functions rather than parameters, they can in principle differ from their assumed forms in very complex ways. However, in order to illustrate the role of these potential differences, I will assume that locally, i.e., in the neighborhood of the mass and distance of the actual lens, they differ by some offset, δK , and that the derivatives of these functions are unaltered. Then, the induced error in M is simply $\delta M = -\delta K / (\partial K / \partial M)$. Following the same procedures as in the previous two subsections,

I find,

$$\frac{\delta M}{M} = \frac{-\delta K/M}{-M'_K - Z\pi_{\text{rel}}/M} \rightarrow \frac{-(\ln 10/5)\delta K}{H(M) + D_L/D_S}. \quad (18)$$

Regarding $A_K(\pi_L)$, a conservative estimate is $|\delta K| \lesssim 0.07$. First, for typical lines of sight, the full column of dust toward the bulge is only $A_K \sim 0.3$, and there are few lines of sight that are substantially above $A_K \sim 0.5$. Second, the great majority of the lenses are either in the bulge (i.e., behind essentially all the dust) or in the disk but well over 100 pc from the Galactic plane (so behind most of the dust). The total extinction toward the bulge is well measured from the position of the clump (Gonzalez et al. 2012), so for these two classes of lenses, $A_K(\pi_L)$ is either the full extinction or slightly less than this. Third, given the small total extinction, a continuous dust model (based, e.g., on a constant dust scale height) would be adequate to achieve 0.1 mag accuracy, even in the near-disk regions. Fourth, it is likely that there will be good 3-D dust maps toward the bulge, based on Gaia data, by the time of first AO light on 30m class telescopes.

Based on the scatter in Figure 22 from Benedict et al. (2016), I estimate $|\delta K| \lesssim 0.07$ for M_K and thus a quadrature sum $|\delta K| \lesssim 0.1$ for both effects combined. This implies that the numerator in Equation (18) is limited by $|(\ln 10/5)\delta K| \lesssim 0.045$.

From the functional form of Equation (18), the errors are most severe for very nearby lenses in the mass range of Equation (14). That is, this source of error is qualitatively similar to the t_E -based error that was just discussed in Section 5.2, except that the numerator of Equation (18) is more constrained. Hence, exactly the same remarks apply about the most difficult cases as in the close of that section.

Finally, I note that the fractional distance error is smaller than the fractional mass error,

$$\frac{\delta D_L}{D_L} = \frac{-(\ln 10/5)\delta K}{H(M) + D_L/D_S} \left(1 - \frac{D_L}{D_S}\right). \quad (19)$$

5.4. Error Induced by $\mu_{\text{rel,hel}}$ and K_{host}

While the uncertainties in $\mu_{\text{rel,hel}}$ and K_{host} are generally expected to be small, it is straightforward to evaluate their impact using the above analysis.

Because $\mu_{\text{rel,hel}}$ and t_E appear symmetrically in Equation (9), the impact of the uncertainty in $\mu_{\text{rel,hel}}$ is directly given by Equations (16) and (17) in Section 5.2 (with the substitution $\delta t_E/t_E \rightarrow \delta\mu_{\text{rel,hel}}/\mu_{\text{rel,hel}}$).

Given the method I have used to estimate the effects of uncertainties in the mass-

luminosity relation and the dust profile, the impact of the uncertainty in K_{host} is directly given by Equations (18) and (19) in Section 5.3.

5.5. Character of the $H(M) \sim 0$ Regime

All the equations for error propagation that are derived above for the mass estimates have the form,

$$\frac{\delta M}{M} \propto \frac{1}{H(M) + D_L/D_S} \quad (20)$$

Hence, in the mass interval of Equation (14), the errors diverge for $D_L \ll D_S$, implying that a practical understanding of this regime is important. From a mathematical perspective, this divergence occurs because Equations (4) and (5) intersect at an acute angle, or, stated otherwise, are nearly parallel at their point of intersection. This is because, in the approximation $\mathbf{v}_{\oplus,\perp} \rightarrow 0$, $\log M = -\log \pi_{\text{rel}} + \text{const}$, while in the approximation $A_K \rightarrow 0$, and in the regime of $H(M) \simeq 0$ (i.e., $L_K \propto M^2$), $\log M = -\log \pi_L + \text{const}$. Hence, for $D_L \ll D_S$ (so $\pi_L \sim \pi_{\text{rel}}$), the slopes are similar. This means that the various other terms that affect the slopes cannot really be ignored in this regime. In particular, the assumption $\mathbf{v}_{\oplus,\perp} \rightarrow 0$ is actually $\pi_{\text{rel}} \mathbf{v}_{\oplus,\perp} \rightarrow 0$, and this is not consistent with the regime $D_L \ll D_S$, unless $\mathbf{v}_{\oplus,\perp}$ is identically zero.

Considerable insight into this regime can be gained by examining the subpanels for OGLE-2005-BLG-071 and OGLE-2012-BLG-0950 in Figure 1. In both cases, there is an extended region where the two curves are basically tangent. These are centered at $(M/M_\odot, D_L/\text{kpc}) \sim (0.35, 2.7)$ and $(0.45, 1.7)$, respectively, i.e., near the upper edge of Equation (14). In both cases, particularly for OGLE-2012-BLG-0950, Equation (4) curves upward in the near-tangent region, which reflects the fact that π_{rel} is not much smaller than $\pi_{\text{rel},\text{min}}$, i.e., the minimum of this curve. And in both cases, Equation (5) curves downward in this region. Hence, in both cases, had K_L been somewhat brighter, there would have been a discrete two-fold degeneracy, with the higher-mass solution well above the regime of Equation (14) and the lower-mass solution being at the low-mass end of this regime. Although there are no such cases among the six historical examples, they are likely to be relatively common in a large sample. These discrete degeneracies can be addressed by the methods discussed in Section 3.

However, the continuous degeneracies represented by the actual cases of OGLE-2005-BLG-071 and OGLE-2012-BLG-0950 cannot be properly captured by the perturbative approach of the present section. Rather, they require direct numerical estimates. Therefore, I will compare the idealized treatments given here with the numerical solutions for these two

events that were given by Bennett et al. (2020) and Bhattacharya et al. (2018), respectively. Interestingly, as noted in Section 2, neither paper presents a version of Figure 2, although such figures are common in papers that derive lens properties from high-resolution imaging. The reason is that each event had substantial π_E information, and the authors of both papers focused on incorporating this information to make the best estimate of the host mass and distance, rather than asking what could be learned from AO measurements alone. In particular, when there is a 1-D π_E measurement that is strongly inconsistent with zero, then a precise measurement of $\mu_{\text{rel, hel}}$ can yield very good measurements of the lens mass and distance without any photometric information (Ghosh et al. 2004; Gould 2014).

Here, however, my goal is to understand the challenges to applying the “basic method”, and I evaluate the role of π_E and other auxiliary information in that context. From this perspective, it is useful to derive the mass and distance estimates from the “basic method” and then check to see whether (or to what extent) they are confirmed by the π_E measurement.

The top panels in Figure 6 show the tracks of Equations (4) and (5) on the $\log M$ - $\log \pi_{\text{rel}}$ plane, i.e., the same as in Figure 1, except here showing error contours. The “top level” contours (displayed in a different color scheme) show the result of combining the two constraints, i.e., adding the χ^2 values from each set of contours. In both cases, there is a strong 1-D degeneracy at the 1σ level, which arises because Equations (4) and (5) are both slightly curved and nearly tangent. For this reason, the $2\text{-}\sigma$ and $3\text{-}\sigma$ errors are not proportionately larger than the $1\text{-}\sigma$ errors

The middle panels show the impact of including the light-curve based π_E measurements. The “top level” contours show the resulting error contours: they are dramatically reduced in the direction of the 1-D degeneracy. The physical origins of this reduction is made clear in the bottom panels where the filled contours show the π_E contours derived from Equations (4) and (5), while the open contours show the π_E constraints from the light curve. In both cases, these are nearly orthogonal, so their combination greatly restricts the modulus of π_E , which is essentially the direction of the 1-D degeneracies in the top panel, i.e., $\log \pi_E \sim (\log \pi_{\text{rel}} - \log M)/2$. Returning to the middle panel, the “second level” contours (in a different color scheme) show the result of combining the light-curve π_E constraint with Equation (4) alone, i.e., the method of Ghosh et al. (2004) and Gould (2014).

For both events, I constructed the light-curve π_E contours (magenta) by making analytic representations of the parallax figures from Dong et al. (2009a) and Bhattacharya et al. (2018). In the first case, this was straightforward and would not warrant particular mention. However, for OGLE-2012-BLG-0950, the numerical parallax contours are quite complex, partly because the two solutions, which arise from the “ecliptic degeneracy” (Jiang et al. 2004), overlap and partly because the solution suffers from the “jerk-parallax degeneracy”

(Gould 2004), which typically generates two well-separated minima along the $\pi_{E,\perp}$ direction. In the present case, the two minima are barely resolved, with the southern solution favored by roughly $\Delta\chi^2 \sim 2$, which is not significant. As the southern solution is ruled out by the Keck observations, I made my analytic representation using the northern solution.

Figure 6 illustrates the key issues regarding the most difficult cases of applying the “basic method”.

First, it shows that these difficult cases are closely associated with the “power-law episode” in the mass-luminosity relation, i.e., the $0.13 \lesssim M/M_\odot \lesssim 0.4$ interval of Equation (14), but they can extend beyond it. In particular, for OGLE-2012-BLG-0950, the actual mass, $M \simeq 0.56 M_\odot$, lies substantially beyond this mass interval. However, this mass value is only known via the incorporation of the light-curve π_E constraint: using the “basic method” alone (and only using the Keck K -band data as I have done and ignoring the *HST* data), the range of solutions broadly overlaps Equation (14) at the 1σ level. This is because, while the local slopes of the two equations have begun to diverge at the true value of M_{host} , the curves themselves remain consistent within their error bars.

Second, these cases illustrate the possibility of discrete degeneracies for which both solutions have $\pi_{\text{rel}} < \pi_{\text{rel,min}}$, even though neither is an example of such a case. That is, in both cases, if the true host mass had been greater (so that the measured K -band flux would have been brighter and thus Equation (5) would have been higher on the plots), then the curves would have intersected in two locations, i.e., to the left and right of the current $1\text{-}\sigma$ range. This possibility arises because (for the regime of Equation (14)), the slope of Equation (5) is very nearly -1 , while the slope of Equation (4) is substantially less negative than -1 (because π_{rel} is not truly small compared to $\pi_{\text{rel,min}}$). In the present two cases, this discrete degeneracy would still have easily been broken by the light-curve π_E measurement. In both cases, these good (albeit 1-D) π_E measurements were facilitated by the events having relatively bright ($I_{S,0} \sim 18.5$), mildly extinguished ($A_I \lesssim 1$), well-magnified ($A_{\text{max}} \gtrsim 10$) sources, and, especially, long ($t_E \sim 70$ day) timescales. Regarding the first three characteristics, conditions will vary strongly for other events. Regarding the long timescales, these were the ratio of rather large θ_E (~ 1 mas) with fairly typical μ_{rel} . In turn, the large θ_E were primarily due to the fact that these are both disk lenses (large π_{rel}). For the case of discrete degeneracies, in which the true solution is the more massive (and more distant) lens, this is less likely to be the case. However, it will still be the case that the alternate (incorrect) solution will predict a large π_E , so that even if π_E is not subject to even a 1-D measurement, the alternate solution can be ruled out. Thus, at least for events with relatively high-quality light curves, it may often be possible to break this discrete degeneracy.

6. A Practical Approach

To transform the mass-ratio measurements that are routinely derived from microlensing light-curve analyses into planet masses requires late-time imaging for essentially the entire sample. There are a relative handful of events that have mass measurements from the microlens parallax effect, but even these should probably be cross-checked with the imaging method for better understanding of potential problems of both methods.

This effort can begin with a single late-time image for each event. This imaging should wait until there is a reasonable expectation that the host and source will be separately resolved. In particular, one must balance the chance that the lens will be bright enough to detect (given the glare of the source), at whatever separation is expected, against the cost of failed observations. For dwarf-star sources, separation of 1.3 times the diffraction-limited FWHM is a reasonable threshold because a large fraction of potential hosts will be visible at this separation. In the K band, this corresponds to $\Delta\theta = 72 (D/10\text{m})^{-1}$ mas, where D is the mirror diameter.

For events with light-curve based ρ measurements, the decision on the wait time will rest on the μ_{rel} estimates, in addition to the characteristics of the observing instrument. For those events without ρ measurements (roughly 1/3 of the final sample), one must adopt a conservative lower limit, e.g., $\mu_{\text{rel, hel}} \gtrsim 2 \text{ mas yr}^{-1}$, in order to minimize the chance of wasting extremely valuable telescope time. Thus, for planets discovered in 2016–2022, the conservative estimates of separation in 2030 are 28–16 mas. Hence, applying the 1.3-FWHM criterion, we immediately see that it would be inappropriate to image any of these events that lack ρ measurements prior to AO first light on 30m class telescopes. On the other hand, it will be appropriate to do so at first AO light on these telescopes, or shortly thereafter, on essentially all of them.

Nevertheless, it will be feasible to image some fraction of the events that have ρ measurements using current instruments. Some of these observations will reveal only the source. The most likely explanation for this outcome is that the proper-motion has been correctly estimated, but the lens is too faint to be detected at the inferred separation. Hence, the indicated response is to wait for 30m AO to obtain a second epoch of imaging. Some will have ambiguous implications because more than two stars are detected. However, as discussed in Section 4.5, these ambiguities can be resolved by a second AO epoch taken after two years or so. Others will have “red flags”, such as an inconsistency between the heliocentric (from imaging) and geocentric (from the light-curve analysis) lens-source relative proper motions, or an inconsistency between the heliocentric proper motion and constraints from the microlens-parallax analysis. These, likewise, can be investigated by additional epoch of imaging two or so years later.

However, it is likely that a substantial fraction of these current-instrument observations will yield good host-mass measurements and so (unless the errors in q are very large) good planet-mass measurements, and these can be the basis for preliminary planet-mass and host-mass function studies. Once 30m-class AO is available, then first epochs can be obtained for the rest of the sample, while those requiring 30m-class second epochs can also be observed, which will lay the basis for comprehensive analyses of the sample as a whole, including events without ρ measurements. In a few cases of “red flags” or non-detection of hosts with giant-star sources, there may be reason for second-epoch 30m observations.

From the pattern of host-mass measurements as a function of θ_E , it will then likely be possible to distinguish which non-detections are due to BDs and which to WDs (or more massive remnants). For example, Kim et al. (2021a) showed that events with $\theta_E, \lesssim 100$ mas (and $\mu_{\text{rel}} \lesssim 10 \text{ mas yr}^{-1}$) are expected to have late M-dwarf or BD hosts. If this expectation is mostly confirmed for those with detections (including those without ρ measurements), then the remainder of those without detections but with ρ measurements can be inferred, with good confidence, to have BD hosts. For events that lack both ρ measurements and host detections, a similar analysis can be conducted based on t_E alone (together with constraints on π_E , when available), although these designations will generally be less secure.

Thus, while the full analysis of the sample must await 30m AO observations, initial progress can be made using present facilities, particularly during the latter part of the 2020s. Moreover, by systematically applying present-day telescopes to events to which these are accessible, the burden on and duration of the 30m AO observations will be reduced.

With these prospects in mind, I present two comprehensive tables of planetary events that are both likely to enter the final sample and are well-analyzed today, i.e., are either published (including on arXiv) or are in a late state of preparation that I have personally reviewed. The sample is defined as planets that have been (or will be) found by the KMT AnomalyFinder (Zang et al. 2022b) in 2016-2019 and 2021-2022 and that have “good” $\log q$ measurements. For present purposes, I define these as having error bars $\sigma(\log q) < 0.2$ and discrete degeneracies (defined as $\Delta\chi^2 < 10$) of $|\Delta \log q| < 0.25$. I conceptually include 2022 because the observing season is mostly complete and there are no major data issues so far, although no planet analyses have yet been completed for this season.

In addition to the planets that are likely to enter the statistical sample, which I have just described, I also include those from the same six seasons that might enter the sample based on further information derived from AO observations, as well as a few others that may be of particular interest for a variety of reasons. These are indicated by the notes that are described below.

Table 1 has 82 events with ρ measurements (or strong upper limits), and Table 2 has 29 events without ρ measurements. The purpose of these tables is to support strategic planning of observations of the sample as a whole. They are not intended as a substitute for the original papers, including tables, which contain many more details than are summarized in these two tables. On the other hand, I have endeavored to provide information directly related to decisions regarding AO follow-up observations in a compact form, including some information that is either absent from or not easily extracted from the discovery papers.

Of all the seasons, only 2018 may be considered as complete (Gould et al. 2022; Jung et al. 2022). As mentioned above, no planets have yet been properly analyzed from 2022, while many planets are still being discovered and/or analyzed for the remaining 4 seasons. I will attempt to provide updated tables and/or supplements as new planets are analyzed.

Each planet is described by two lines in Table 1. The first column gives the event name in the first row and the KMT name (if different) in the second row. The second column gives t_0 , i.e., the peak of the event, while the third column gives the proper motion and its error. The fourth through sixth columns give the dereddened magnitude and color of the source and its K -band extinction. The sixth column gives the Galactic coordinates. The seventh through tenth give the logarithms of the Einstein timescale t_E (in days), the impact parameter u_0 , the normalized source radius ρ , and the mass ratio q , as well as their errors. All of these quantities are given for the lowest- χ^2 solution. Where there are major differences between solutions that are within $\Delta\chi^2 < 10$, these are discussed in the notes. The next column gives Earth’s projected velocity $\mathbf{v}_{\oplus,\perp}$ at t_0 in (N,E) coordinates and in km s^{-1} , followed by M_{cr} , which is expressed in units of $0.075 M_{\odot}$, i.e., the hydrogen-burning limit, and which is defined by

$$M_{\text{cr}} \equiv \frac{\theta_E^2}{\kappa} \frac{v_{\oplus,\perp}}{\text{au}\mu_{\text{rel}}} = \frac{\mu_{\text{rel}} v_{\oplus,\perp} t_E^2}{\text{au}\kappa} \quad (21)$$

The penultimate column gives 5 codes that are described below, while the final column gives the discovery reference.

The only quantity in Table 1 that is likely to be unfamiliar is M_{cr} , which is the lens mass at which $|\boldsymbol{\mu}_{\text{rel}} - \boldsymbol{\mu}_{\text{rel, hel}}| = \mu_{\text{rel}}$. At higher host masses, i.e., $M_{\text{host}} > M_{\text{cr}}$, the correction from geocentric to heliocentric will be smaller. Hence, if this quantity is well below the hydrogen-burning limit (i.e., $\ll 1$ in Table 1), then one need not be concerned about this correction because the hosts for which it is significant cannot be seen anyway. Otherwise, the correction must be carefully considered.

The parameters t_0 , μ_{rel} , $\sigma(\mu_{\text{rel}})$, $I_{s,0}$, $(V - I)_{s,0}$, A_K , and the Galactic coordinates (l, b) are the most important for deciding at what point the event can profitably be observed. The

first three of these allow one to estimate the separation and its uncertainty as a function of time, while the next two allow one to estimate the source type. In general, giants will require substantially greater separations than dwarfs. The last three of these columns are usually of minor importance, but a large value of A_K may affect observing strategy, while a small value of $|b|$ may indicate a substantial probability that the source cannot be assumed to be in the bulge. Note that the expected source flux in K can be estimated by combining $[(V - I), I]_{S,0}$, and A_K , together with tabulated VIK photometry (e.g., Bessell & Brett 1988). However, for purposes of a quick estimate, one can just approximate $K_S \sim I_{S,0} - (V - I)_{S,0} + A_K$. Note if the μ_{rel} estimate is a lower limit (rather than a measurement) it is shown in bold face.

The four parameters t_E , u_0 , ρ , and q (and their errors), can help understand the potential role of AO observations, as follows. If the fractional error in t_E is small, e.g., $\sigma(\log t_E) \lesssim 0.02$, then this error does not undermine the host mass and distance estimates relative to other sources of error. See Section 5.2. Otherwise, it will be of interest whether the t_E error can be reduced via its correlations with f_S and ρ , as described in Sections 4.5 and 5.2. Then, if the logarithmic errors in t_E and u_0 are very similar, it is a good indication that f_S and t_E are strongly anti-correlated, implying that it may well be possible to reduce the error in t_E using this technique. An analogous logic applies if the logarithmic errors in t_E and ρ are similar. The logarithmic error in q is of interest for two reasons. First, a high value of this parameter would imply that the event is less useful for constraining fine details of the planet mass function. Second, if the logarithmic errors in q are not much bigger than those in t_E , this probably means that $t_q \equiv qt_E$ is much better measured than q , so that if $\sigma(\log t_E)$ can be reduced by the above-mentioned techniques, then $\sigma(\log q)$ can be reduced as well.

The projected velocity $\mathbf{v}_{\oplus,\perp}$ is presented because it is an input into M_{cr} : if the M_{cr} test mentioned above indicates that the correction from heliocentric to geocentric must be taken into account, then the vector form of this quantity will be important.

Table 2 is similar to Table 1 except that it omits the columns: μ_{rel} , $\log \rho$, and M_{cr} , for which there is no information.

Table 3 gives the meanings and distributions of the five codes in the penultimate columns of Tables 1 and 2. The first code (0 or 1) indicates whether there is comment in the following two sections about the event. The second code gives my evaluation of whether the event will enter a statistical sample of AnomalyFinder detected planets with AO imaging. The third code tells the largest discrete degeneracy in $\log q$. My orientation is that if there is no degeneracy, or if $\Delta \log q < 0.1$, there should be no concern. Otherwise, I indicate the magnitude of this parameter. The fourth code gives the lens/source multiplicity. Most events are 2L1S. Those that are 3L1S are divided between events with two planets and events with

planet+binary. Here, $nLmS$ means n lenses and m sources. The final code tells whether the event has *Spitzer* data. Each classification in Table 3 gives the total number, in parentheses, of entries in Tables 1 and 2 with that classification. Note, in particular, that there are 4 3L1S 2-planet systems, which have a total of “8” planets.

6.1. Comments on Events in Table 1

6.1.1. 2016

MOA-2016-BLG-227: Koshimoto et al. (2017b) conducted Keck AO observations on $HJD' = 7613.85$, i.e., at $\tau = (t - t_0)/t_E \sim 5.6$ after peak. They detected excess flux but concluded that it was not likely to be due to the host. Regardless of whether this assessment turns out to be correct, these images form a valuable first epoch. **MOA-2016-BLG-319** has only an upper limit $\rho > 0.01$, but this places a significant constraint on μ_{rel} , so it is included in Table 1.

OGLE-2016-BLG-0613 is a 3L1S system, i.e., a stellar binary with a planet. Solution “C” is favored over solutions “B” and “D” by $\Delta\chi^2 = 10.0$ and 13.2, respectively. However, its model source flux is about 1.4 mag too faint, given its color. The other two solutions are brighter by 0.75 mag and 1.04 mag, respectively, and so they are favored in this sense. Late-time AO in two bands, one near the I band (e.g., J) and the other at K (to determine the color correction) could easily distinguish between “C” and “B”/“D”. Both “B” and “D” predict proper motions that are a factor ~ 1.5 larger than “C”, so this would provide a second test. If “B”/“D” are preferred, it would be difficult to distinguish between them. However, they differ in mass ratio by only $\Delta \log q_3 = 0.06$, compared to $\Delta \log q_3 = 0.29$, for “D” relative to “C”. This event entered the AnomalyFinder sample due to its binary-star component, rather than its planet. Hence, the search would have to be expanded to look for planets in all binary events for this planet to enter a statistical sample. This may well occur prior to first AO light on 30m class telescopes. **OGLE-2016-BLG-0693:** For this event, the source flux is very poorly measured, so the parameter combinations $t_E \times (u_0, \rho, q, f_S) = (5.5, 0.15, 8.8, 2.6)$ day are much better measured than (u_0, ρ, q, f_S) . Here, f_S is the flux on an $I = 18$ scale. In Table 1, I report the values and errors of all quantities assuming that $f_{S,\text{OGLE-IV}} = 0.0158$, i.e., the “fiducial value” adopted by Ryu et al. (2017a). A central goal of AO observations should be to measure I_S , which can be done by observing in J (a close proxy for I) and K (to determine the color correction). Note that in a free fit, $q \sim 0.02$ which is within the range of study of current statistical analyses of KMT data, while the fiducial I_S yields $q \sim 0.06$ (which is not). These issues can only be resolved by AO observations. **OGLE-2016-BLG-1067** has a *Spitzer* parallax measurement (Yee et al. 2015). However,

as there is only an upper limit on ρ , this did not yield mass and distance estimates. Because the ρ upper limit places a significant constraint on μ_{rel} , I have included this event in Table 1. **OGLE-2016-BLG-1093** has a *Spitzer* parallax measurement (Yee et al. 2015), which yields a host mass, planet mass, and system distance of $M_{\text{host}} \sim 0.46 M_{\odot}$, $M_{\text{planet}} \sim 0.71 M_{\text{Jup}}$ and $D_L \sim 8.1$ kpc. **OGLE-2016-BLG-1190** has a *Spitzer* parallax measurement (Yee et al. 2015), which yields a host mass, planet mass, and system distance of $M_{\text{host}} \sim 0.91 M_{\odot}$, $M_{\text{planet}} \sim 13.4 M_{\text{Jup}}$ and $D_L \sim 6.8$ kpc. There is substantial orbital motion information from the fit, and the predicted period and semi-major axis are $P \sim 3$ yr and $a \sim 2$ au. The host is expected to be $K_{\text{host}} \sim 18.5$. Hence, RV observations could confirm and greatly refine the orbital parameters presented by Ryu et al. (2017b) in their Figure 10 and Table 7. **OGLE-2016-BLG-1195** has a *Spitzer* parallax measurement (Yee et al. 2015), which yields a host mass, planet mass, and system distance of $M_{\text{host}} \sim 0.08 M_{\odot}$, $M_{\text{planet}} \sim 1.4 M_{\oplus}$ and $D_L \sim 3.9$ kpc (Shvartzvald et al. 2017). If correct, this would imply $K_{\text{host}} \sim 23.7$, i.e., $\Delta K \sim 6.3$ mag fainter than the source. Moreover, within errors, the host could be below the hydrogen-burning limit and thus much fainter. However, the *Spitzer* flux variation is only about 2.5 units, i.e., just a few times larger than the level of systematic effects seen in other events. Moreover, the full solution would imply a counter-rotating object in the Galactic disk. A Bayesian analysis carried out without the *Spitzer* data yields $M_{\text{host}} \sim 0.37 M_{\odot}$, $M_{\text{planet}} \sim 5.1 M_{\oplus}$ and $D_L \sim 7.2$ kpc, and thus would imply $K_{\text{host}} \sim 21.0$, i.e., $\Delta K \sim 3.6$ mag fainter than the source (Bond et al. 2017). This would certainly be observable at first AO light of 30m class telescopes and possibly before that using 8m-class telescopes. Note that the parameters in Table 1 are the weighted average of those reported by Shvartzvald et al. (2017) and Bond et al. (2017), who analyzed completely independent data sets. **OGLE-2016-BLG-1227**: Because the source is a bright giant and the host is likely to be a late M dwarf in or near the bulge, a separation of $\Delta\theta \sim 5$ FWHM ~ 70 mas for EELT is likely required to resolve the source and host. Given the extremely low proper motion, $\mu_{\text{rel}} = 0.8$ mas yr $^{-1}$, this would require almost a century wait time for EELT, but perhaps “only” 35 years for VLTI GRAVITY (Dong et al. 2019), which is effectively a 100m-class telescope. Note that M_{cr} is small, so the heliocentric and geocentric proper motions will not differ greatly.

KMT-2016-BLG-0212: Late-time AO observations can definitely distinguish between two classes of degenerate solutions with $\Delta \log q = 2.88$ (Hwang et al. 2018b). “Class I” (which is favored by $\Delta\chi^2 = 6.6$) predicts a source flux that is fainter by $\Delta I_S = 1.1$ mag. Thus, combining a nearby band (e.g., J) to approximate I with a more distant one (e.g., K) to make the color correction, will distinguish between these. If the smaller- q (higher χ^2) “Class II” solutions are confirmed, then among these, the “wide 2b” solution has a larger q by a factor 1.7 compared to “wide 2a” and “wide 3”. However, “wide 2a” predicts a 20% larger proper motion than “wide 2b”, so that if the former were confirmed by AO observations,

then this would also confirm the lower mass ratio, $q = 5 \times 10^{-5}$. Unfortunately, the reported errors in the μ_{rel} predictions are larger than their difference, and these are basically rooted in the relatively large error in ρ , so they cannot be substantially ameliorated by late time observations. Note that if “Class I” is confirmed, the mass ratio would be beyond the $q < 0.03$ limit for current systematic searches. **KMT-2016-BLG-1107** has a mass ratio that is beyond the $q < 0.03$ limit for current systematic searches. In addition, it is likely to be extraordinarily difficult to resolve because the source is extremely bright and the lens is expected to be a late M dwarf or BD in or near the bulge (Hwang et al. 2019), while μ_{rel} is very low. **KMT-2016-BLG-2605** is not in the current AnomalyFinder statistical sample because the underlying event was not discovered by AlertFinder or EventFinder, but rather in a special supplementary search that targeted giant-source events. Hence, it was not searched for planets by AnomalyFinder. However, it is interesting because t_{E} is the shortest for any microlensing planet, and its $\theta_{\text{E}} = 0.116$ mas implies that the host lies near the star/BD boundary (Ryu et al. 2021). Nevertheless, even if it is a star, the contrast ratio will correspond to $\Delta K \sim 7.5$. Hence, despite its high proper motion, $\mu_{\text{rel}} \sim 12 \text{ mas yr}^{-1}$, it probably cannot be resolved until the advent of 30m-class AO. However, as noted by Ryu et al. (2021), the highly uncertain source color could already be measured by high resolution (AO or *HST*) observations in two bands, which would improve the θ_{E} and μ_{rel} estimates that are critical to its interpretation, whether or not the host is luminous. It would be straightforward to extend the AnomalyFinder search to the 2016-2019 special giant-source sample (Gould et al. 2022), in which case this planet would likely become part of the statistical sample.

6.1.2. 2017

OGLE-2017-BLG-0173 has a $\Delta \log q = 0.41$ discrete degeneracy at $\Delta \chi^2 = 3.5$, which favors the lower mass ratio. The two solutions have $\Delta \log \rho = 0.039 \pm 0.29$, which fundamentally limits how well a proper-motion measurement could distinguish between these solutions. In fact, the source color was not measured during the event, so this would also have to be precisely measured by AO followup in order to derive a precise light-curve based proper-motion prediction. Even if perfectly successful, this could only add at most $\Delta \chi^2 = 1.8$ to the light-curve preference. Hence, the two solutions can be only marginally distinguished, even in principle. Nevertheless, because both solutions have low- q , it would be of interest to measure the host mass. **OGLE-2017-BLG-0373** has a $\Delta \log q = 0.38$ discrete degeneracy. The two solutions have nearly identical μ_{rel} , so they cannot be distinguished by a late-time proper-motion measurement. They have a $\Delta I_S = 0.17 \pm 0.07$. See Table 2 of Skowron et al. (2018). This could, in principle be distinguished, but would require two pho-

tometric bands, including one near the I band. **OGLE-2017-BLG-0406** has a *Spitzer* parallax measurement (Yee et al. 2015), which yields a host mass, planet mass, and system distance of $M_{\text{host}} \sim 0.56 M_{\odot}$, $M_{\text{planet}} \sim 0.41 M_{\text{Jup}}$ and $D_L \sim 5.2$ kpc. These would imply $K_L \sim 19.3$, i.e., $\Delta K \sim 4.5$ mag fainter than the source. Hence, the imaging of this event should not be attempted before 30m-class AO is available. I note that the π_E measurement is derived from the intersection of two 1-D parallax measurements, one from *Spitzer* and one from the ground, as originally suggested by Gould (1999). AO imaging would provide an important test of this approach. **OGLE-2017-BLG-1140** has a *Spitzer* parallax measurement (Yee et al. 2015), which yields a host mass, planet mass, and system distance of $M_{\text{host}} \sim 0.21 M_{\odot}$, $M_{\text{planet}} \sim 1.62 M_{\text{Jup}}$ and $D_L \sim 7.4$ kpc. These would imply $K_L \sim 22.3$, i.e., $\Delta K \sim 8$ mag fainter than the source. Hence, the imaging of this event should not be attempted before 30m-class AO is available. **OGLE-2017-BLG-1434** has excellent measurements of both π_E and θ_E , and these yield $M_{\text{host}} = 0.234 \pm 0.026 M_{\odot}$, $M_{\text{planet}} = 4.4 \pm 0.5 M_{\oplus}$, and $D_L = 0.86 \pm 0.09$ kpc. Blackman et al. (2021) confirmed these measurements by measuring the excess light due to the lens (while it was still superposed on the source in 2018) using Keck AO. **OGLE-2017-BLG-1691** has a 1L2S solution that is disfavored by $\Delta\chi^2 = 13.9$, with both KMTC and KMTS points directly on the anomaly contributing significantly. Thus, it can be confidently excluded. Nevertheless, I note that $\rho_{2,1L2S}/\rho_{2L1S} \simeq 1$, while $q_F = 0.006$, which together imply a ratio of predicted proper motions of $\mu_{\text{rel},1L2S}/\mu_{\text{rel},2L1S} \sim 0.2$. Thus, the late-time AO proper-motion measurement can provide an additional, and very strong, argument against 1L2S.

KMT-2017-BLG-0165: Jung et al. (2019a) argue from several lines of evidence that the lens dominates the blended light. Because the source and blend are of comparable brightness and color and are relatively isolated (see their Figure 7), this implies that they could be resolved at separations $\Delta\theta \gtrsim 40$ mas, which will occur beginning about 2024. In principle, this might create ambiguity between identifying the source versus the host. However, their Figure 4 shows that the host lies will lie to the east of the source. **KMT-2017-BLG-1003** is listed as having $\rho = 5.2 \pm 1.2 \times 10^{-3}$ measurement because this is the result for the “outer” solution, which is very slightly favored by χ^2 . However, the other (“inner”) solution has a very similar 3σ upper limit, $\rho < 6.7 \times 10^{-3}$, so the listed μ_{rel} is a good guide to determining the wait time. **KMT-2017-BLG-1038:** Shin et al. (2019) do not report $((V - I), I)_{S,0}$, so I have estimated $I_{S,0} = 18 - 2.5 \log(f_{S,KMTC}) - A_I$, and I have estimated $(V - I)_{S,0}$ from the colors of stars with the same I -band offset from the clump (as determined from Table 1 of Nataf et al. 2013) as those in Baade’s Window (as derived from *HST* photometry from Holtzman et al. 1998). While there is a best estimate of $\rho = 0.0012$, the finite-source signature is weak. Hence, Table 1 values are based on the upper limit $\rho < 0.004$. This means that the best estimate of the proper motion is roughly

3.3 times larger than the lower limit in Table 1. **KMT-2017-BLG-1194** has only an upper limit $\rho > 0.0026$, but this places a significant constraint on μ_{rel} , so it is included in Table 1.

6.1.3. 2018

OGLE-2018-BLG-0506 has only an upper limit on ρ but this leads to a strong constraint on the proper motion, $\mu_{\text{rel}} > 6.5 \text{ mas yr}^{-1}$, which can be used to predict when the lens and source are adequately separated for observations. **OGLE-2018-BLG-0532** has a blend that is about $\Delta K \sim 3$ mag brighter than the source and $\lesssim 50$ mas from it. In principle, this could be the host, but it is more likely to be a companion to the host or a random field star. In any case, its close proximity, together with the low proper motion, $\mu_{\text{rel}} = 3.3 \text{ mas yr}^{-1}$, imply that observations prior to 30m-class AO would be challenging. **OGLE-2018-BLG-0596** has a *Spitzer* parallax measurement (Yee et al. 2015), which yields a host mass $M_{\text{host}} \sim 0.23 M_{\odot}$ at $D_L \sim 5.6$ kpc, which would be $\Delta K \sim 7$ mag fainter than the source. Hence, the imaging of this event should not be attempted before 30m-class AO is available. **OGLE-2018-BLG-0677** is not in the AnomalyFinder statistical sample because it failed the $\Delta\chi^2$ criterion in the automated search. Although ρ is not measured, it is included in Table 1 because the limit on ρ is significant. **OGLE-2018-BLG-0740** has a bright, blue blend that is almost certainly the host or a companion to the host. Han et al. (2019a) obtained a spectrum and showed that there is only a 5% probability for the host-companion scenario. The light curve is consistent with $\rho = 0$. The values of ρ and μ_{rel} in Table 1 are derived under the assumption that the blend (with spectroscopic mass, $M_B = 1.0 \pm 0.1 M_{\odot}$) is the host. If the proper motion from late-time AO were inconsistent, it would imply that the blend is a companion to the host. This could be confirmed by a second epoch, which would demonstrate that the blend trajectory does not “point back” to the source. Hence, this is a very interesting case. Unfortunately, the source is $\Delta K \sim 5$ mag fainter than the blend. Therefore, imaging should not be attempted before 30m-class AO is available. **OGLE-2018-BLG-0799** has a *Spitzer* parallax measurement (Yee et al. 2015). However, a combination of a weak signal and low-level systematics made it difficult to reach unambiguous conclusions. The preferred solution had $M_{\text{host}} \sim 0.1 M_{\odot}$ at $D_L \sim 4$ kpc. Given that the source is a lower giant-branch star, this would imply a contrast offset of $\Delta K \sim 8$ mag, which would require a lens-source offset of order 5 FWHM for a detection. However, this solution predicts $\mu_{\text{rel, hel}} \sim 4 \text{ mas yr}^{-1}$, roughly double the value of $\mu_{\text{rel}} \sim 1.8 \text{ mas yr}^{-1}$ shown in Table 1. These are compatible in part because the ρ measurement is consistent with zero at 3σ , and partly because $\pi_{\text{rel}} v_{\oplus, \perp} / \text{au} \sim 0.76 \text{ mas yr}^{-1}$ at the preferred distance. Even with this higher proper motion, it would be very difficult to detect the host prior to 2030, using current instruments. Hence, it seems prudent to await 30m-class AO before imaging this event. Finally, note that based on a systematic

analysis of the role of *Gaia* in the interpretation of microlensing planets, Ryu et al. (2022b) concluded that the *Gaia* proper motion of the source should not have been incorporated into the analysis. **OGLE-2018-BLG-0932** has *Spitzer* data (Yee et al. 2015), which show a strong signal, although these have not yet been analyzed. However, it is likely that they will be analyzed prior to AO imaging. **OGLE-2018-BLG-0977** has a well-defined $\chi^2(\rho)$ minimum of $\rho = 1.9_{-0.6}^{+0.3} \times 10^{-3}$. While it is consistent with $\rho = 0$ at 3σ , significantly smaller ρ would imply an improbably high μ_{rel} . In any case, our present concern is that the light curve robustly predicts that the proper motion is relatively high. Hwang et al. (2022) made a Bayesian estimate, $\mu_{\text{rel}} = 6.0_{-1.8}^{+3.0} \text{ mas yr}^{-1}$. Thus, this is a plausible target for current instruments in the late 2020s, but it would be safer to wait for 30m-class AO. **OGLE-2018-BLG-1185** has a *Spitzer* parallax measurement (Yee et al. 2015). While the flux only declines about 1 *Spitzer* flux unit (i.e., of order the systematic errors seen in other events), the fact that the decline is not steeper places strong constraints on the mass of the host. Hence, this is likely to be a mid-to-late M dwarf. If the former, then the host would be $\Delta K \sim 3.5$ mag fainter than the source, while if the latter, it would be $\Delta K \sim 6$ mag. Given the relatively low proper motion, $\mu_{\text{rel}} \sim 5 \text{ mas yr}^{-1}$, it would seem prudent to wait for 30m-class AO. **OGLE-2018-BLG-1269** has a bright, $I \sim 15.8$, blend that is very likely to be the lens. It is $\Delta K \sim 3$ mag brighter than the source. Given the relatively high proper motion, $\mu_{\text{rel}} \sim 8 \text{ mas yr}^{-1}$, it probably can be imaged using current instrumentation in the late 2020s. **OGLE-2018-BLG-1647** has a μ_{rel} estimate that is so low as to invite suspicion, in particular because the ρ measurement is derived from a ridge crossing, rather than a caustic crossing. However, Jung et al. (2022) investigated the constraints on ρ in detail and found that $\rho < 2.3 \times 10^{-3}$ was excluded at 2.5σ , which places a limit $\mu_{\text{rel}} < 1.4 \text{ mas yr}^{-1}$. Hence, this event should await 30m-class AO before imaging.

KMT-2018-BLG-0029 has a *Spitzer* parallax measurement (Yee et al. 2015), from which $M_{\text{host}} \sim 1.2 M_{\text{host}}$ and $D_L \sim 3.4 \text{ kpc}$. If correct, the host would be of order 3.5 mag brighter than the source. **KMT-2018-BLG-0087** has only an upper limit on ρ , but this leads to a strong constraint on the proper motion, $\mu_{\text{rel}} > 7 \text{ mas yr}^{-1}$, which can be used to predict when the lens and source are adequately separated for observations. Note, however, that the source is a giant, $K_{S,0} \sim 12.3$, whereas the Bayesian analysis predicts $M_{\text{host}} \sim M \sim 0.1 M_{\odot}$ and $D_L \sim 7 \text{ kpc}$, i.e., $K_{\text{host},0} \sim 23.5$. Hence, imaging should not be attempted before 30m-class AO is available. Possibly, it is a candidate for VLTI GRAVITY (Dong et al. 2019), which is effectively a 100m-class telescope. **KMT-2018-BLG-0748** has $\theta_E = 0.11 \text{ mas}$, and therefore is likely to have $M_{\text{host}} \sim 0.1 M_{\odot}$ and to lie in or near the bulge. This would imply that it would be $\Delta K \sim 7$ mag fainter than the source and so, challenging to detect prior to 30m-class AO. **KMT-2018-BLG-1025** is not currently in the AnomalyFinder statistical sample because it has a discrete degeneracy $\Delta \log q = 0.29$.

However, as noted by Han et al. (2021a) this will likely be resolved by AO observations because the two solutions predict μ_{rel} values that differ by significantly more than their error bars. Note that M_{cr} is small, so the conversion from heliocentric to geocentric should not interfere with breaking this degeneracy. The best solution has only an upper limit on ρ , but it strongly constrains μ_{rel} , so the event is included in Table 1. **KMT-2018-BLG-1292**: The host is likely to be the origin of the blended light, in which case it would probably be an F or G dwarf at $D_L \sim 3.3$ kpc. To verify this would require separately resolving them, which is probably best done in J band because the blend and the source have similar brightness in I band, while the source is ~ 4.5 mag brighter in the K band. However, because $b = -0.28^\circ$ and $A_I \sim 5.2$, it would be challenging to apply the “basic method” to this event. Rather, the host mass should be measured by obtaining a spectrum in the V/I range of the energy distribution. Note that $V_B \sim 20.8$, while $V_S \sim 25$, so there would be very little source contamination in the V band. **KMT-2018-BLG-1743** is not currently in the AnomalyFinder statistical sample because it has a discrete degeneracy $\Delta \log q = 0.48$. However, as noted by Han et al. (2021c) this may possibly be resolved by AO observations because the two solutions predict μ_{rel} values that differ substantially. Nominally, the predictions of the two solutions are consistent at 1σ , primarily because ρ is poorly measured in the alternate (higher χ^2 , higher q solution). However, if the measured proper motion is near the prediction of the favored solution, which has smaller errors, the combined likelihood of the light-curve fit and the proper-motion prediction may be sufficient to clearly choose the favored solution. If, on the other hand, the proper motion is substantially higher than that of the favored solution, the other solution will be clearly selected. Note that M_{cr} is small, so the conversion from heliocentric to geocentric should not interfere with breaking this degeneracy.

6.1.4. 2019

OGLE-2019-BLG-0299 has only an upper limit on ρ . However, it is included in Table 1 because the resulting lower limit $\mu_{\text{rel}} > 1.74 \text{ mas yr}^{-1}$ is significant. **OGLE-2019-BLG-0960** has a *Spitzer* parallax measurement (Yee et al. 2015), as well as a strong ground-based parallax signal, with which it is in moderate tension. It is likely that the host is responsible for the blended light, in which case they could be separately resolved by 2025 (Yee et al. 2021). It is likely that the planet has mass $M_{\text{planet}} \sim 2 M_{\oplus}$.

KMT-2019-BLG-0371 has $q = 0.08$, so it lies well beyond the current completeness limit $q < 0.03$ of the AnomalyFinder samples. It is nonetheless an interesting target because it is a short event ($t_E = 6.5$ day) with a small $\theta_E = 140 \mu\text{as}$, and so Bayesian mass estimate

$M_{\text{host}} \sim 0.09 M_{\odot}$. If correct, then $M_{\text{planet}} \sim 7.5 M_{\text{Jup}}$, i.e., inside the nominal planetary range. Moreover, it would not be difficult to extend the current complete sample to short- t_E , low- q events, e.g., $t_q \equiv qt_E < 0.6$ days, in order to study the whole class of these objects. **KMT-2019-BLG-0842**: The blended light is $\Delta I \sim 2$ mag and $\Delta K \sim 1.5$ mag brighter than the source. Jung et al. (2020b) argue that it is plausibly the host. Hence, given the estimated $\mu_{\text{rel}} = 8.0 \pm 1.8 \text{ mas yr}^{-1}$ proper motion, this could be a good target with present instruments starting about 2029. **KMT-2019-BLG-1715** is a 3L2S event, with a planet in a binary-star system that microlenses a binary source. However, because the principal anomaly is due to the planet magnifying the primary source, its discovery by AnomalyFinder followed the standard path, and so it should be included in statistical samples.

6.1.5. 2021

KMT-2021-BLG-0119 has only an upper limit $\rho > 0.0018$, but this places a significant constraint on μ_{rel} , so it is included in Table 1. It has a significant 1-D π_E measurement, which constrains the lens to lie in the relatively near disk, $D_L \sim 3$ kpc. Shin et al. (2022b) note that the blended light is consistent with being the lens, and because it contains $\sim 40\%$ of the baseline light, this can be checked with AO observations taken immediately. **KMT-2021-BLG-0171** was discovered as part of a part of a follow-up program by which the anomaly was monitored intensively from the LCO facility at SSO (Yang et al. 2022). However, AnomalyFinder recovered the anomaly based on KMTA data. That is, the planet detection was not influenced by the follow-up data. Rather, these served to improve the characterization. Note that there are alternate solutions, which are disfavored by only $\Delta\chi^2 = 6.4$ and have smaller q by $\Delta \log q = -0.34$. However, Yang et al. (2022) argue that these are heavily disfavored by phase-space considerations. **KMT-2021-BLG-0240** has two classes of solutions, with 2L2S favored over 3L1S by $\Delta\chi^2 = 10.5$. Han et al. (2022f) argue that neither is decisively favored because the 2L2S solution would predict violent wiggles unless the binary-source is seen in deep projection, and these are not present in the light curve. In Table 1, I have listed the 3L1S solution. To be included in statistical studies, the 3L1S/2L2S degeneracy must be broken: otherwise the planet (or first planet for 3L1S) has three possible mass ratios, $q \sim (3.5, 6.5, 9.5) \times 10^{-4}$, which is probably too broad a range to be useful. The two classes predict different μ_{rel} , i.e., $\mu_{\text{rel},3\text{L1S}} = 3.1 \pm 0.4 \text{ mas yr}^{-1}$ and $\mu_{\text{rel},2\text{L2S}} = 3.9 \pm 0.8 \text{ mas yr}^{-1}$. Because these overlap, measurement of $\mu_{\text{rel,hel}}$ will not decisively distinguish between them. However, unless the binary source is in extreme projection, the RV variations should be easily visible from spectroscopy if 2L2S is correct. That is, for this case, $\sin i \sim 1$, while $(M_{S,1}, M_{S,2}) \sim (1.0, 0.6)M_{\odot}$, so the semi-amplitude of RV variations will be $v_{\text{semi}} \sim 14(a_S/\text{au})^{-1/2} \text{ km s}^{-1} = 110(a_S/a_{\perp,S})^{-1/2} \text{ km s}^{-1}$, where $a_{\perp,S} = 0.016 \text{ au} = 3.4 R_{\odot}$.

is the projected separation observed at t_0 . In the 2L2S scenario, the primary source has $I_{S,1} \simeq 21.1$ and $K_{S,1} \simeq 16.6$. There is relatively little blended light, so detection of such large RV signals is probably feasible today, without waiting for the source and lens to separate. If the 3L1S solution is confirmed, then the first planet has a discrete degeneracy $\Delta \log q = 0.17$, which is acceptable, while the second has $\Delta \log q = 0.32$, which may not be. **KMT-2021-BLG-0748** has an “alternate solution”, which is disfavored by $\Delta \chi^2 \sim 10$ and which Ryu et al. (2022a) consider to be a “satellite solution”. The satellite solutions differ somewhat in their physical implications because $\Delta \log q \sim 0.30$. They differ in I_S by 1 magnitude and so could be distinguished using J -band and K -band measurements together with IJK color-color relations. Because $\mu_{\text{rel}} \sim 3 \text{ mas yr}^{-1}$, these measurements should wait for 30m AO. **KMT-2021-BLG-0912** has three solutions with very different q , i.e., $(\Delta \log q, \Delta \chi^2)_{\text{Close I}} = (+0.42, +9.5)$ and $(\Delta \log q, \Delta \chi^2)_{\text{Wide}} = (-0.79, +19.2)$ relative to the “Close II” solution that is listed in Table 1. Once μ_{rel} is measured, it can easily distinguish between the heavily disfavored Wide solution and the two Close solutions because the former predicts $\mu_{\text{rel,Wide}} = 10 \pm 1, \text{ mas yr}^{-1}$. The two Close solutions will be more difficult to distinguish because $\mu_{\text{rel,Close II}} = 3.8 \pm 1.0 \text{ mas yr}^{-1}$, while $\mu_{\text{rel,Close I}} = 2.6 \pm 0.5 \text{ mas yr}^{-1}$, and hence their predicted distributions overlap. The relatively large errors are dominated by the errors in ρ , and the much smaller fractional errors in t_E and u_0 in Table 1 imply that an improved measurement of I_S from AO will not substantially improve the error in ρ . Hence, it is unclear whether the Close I/II degeneracy will be decisively resolved by AO measurements, although Close II is substantially preferred by χ^2 . **KMT-2021-BLG-1253** will almost certainly **not** be part of an objective sample because (with $\Delta \chi^2 = 105$)(with $\Delta \chi^2 = 105$) it failed the $\Delta \chi^2 > 120$ criterion for selection by AnomalyFinder. Nevertheless, if this event is pursued, it should be noted that it has an alternate solution, which is disfavored by $\Delta \chi^2 \sim 1.6$ and has $\mu_{\text{rel}} \sim 9 \text{ mas yr}^{-1}$. Both proper-motion estimates would allow the host to be detected with current instruments for observations beginning about 2029, provided that it is sufficiently bright. However, if the Bayesian estimates are approximately correct, the host will be $\Delta K \sim 3.3$ mag fainter, which could be challenging prior to 30m-class AO. **KMT-2021-BLG-1391** has an alternate solution, which is disfavored by $\Delta \chi^2 \sim 5$ and has $\mu_{\text{rel}} \sim 2.6 \text{ mas yr}^{-1}$. Hence, imaging should probably not be attempted until 30m-class AO is available. The solutions can be distinguished by the $\mu_{\text{rel,hel}}$ measurement, although the physical implications of the different solutions are very similar, in any case. **KMT-2021-BLG-1554** has a 1L2S solution that is disfavored by $\Delta \chi^2 = 10.4$. The 2L1S solution looks substantially better by eye, but the 1L2S solution cannot be absolutely excluded based on $\Delta \chi^2$ alone. The best-fit 1L2S solution is unphysical in the sense that the offset between the sources is $\Delta u_S \sim 0.003$, while the primary source has $\rho_{1,1L2S} = 0.098 \pm 0.024$. That is, either the secondary would be enveloped in the primary (if the physical separation were similar to the projected separation) or there would be strong eclipses (if the true separation were much

larger). This conflict could be ameliorated by reducing $\rho_{1,1L2S}$, but only at a substantial cost in χ^2 . Thus, the 1L2S solution can be decisively excluded based on a combination of arguments. These can be further tightened by a late-time AO proper-motion measurement. **KMT-2021-BLG-1689** was discovered as part of a part of a follow-up program by which the anomaly was monitored intensively from the Auckland Observatory (Yang et al. 2022). There were no KMT data over the anomaly, and hence it was not recovered by AnomalyFinder. Therefore, it does not enter the KMT-based statistical sample. It may still enter a statistical sample based on follow-up protocols. See, e.g., Gould et al. (2010). Note that there are alternate solutions, which are disfavored by only $\Delta\chi^2 = 2.4$ and have smaller q by $\Delta \log q = -0.11$. However, Yang et al. (2022) argue that these are heavily disfavored by phase-space considerations. Moreover, they can easily be vetted by late-time AO observations because they predict proper motions that are twice as fast. **KMT-2021-BLG-1898**: The interpretation will be somewhat complicated by the fact that there are two sources as well as a bright blend. At t_0 , the sources were separated in the Einstein ring by $\Delta u_S \sim 7.8 \times 10^{-3}$, corresponding to $\Delta\theta_S \sim 2.5 \mu\text{as}$ and projected separation $a_{\perp,S} \sim 4 R_{\odot}$. Hence, they are almost certainly in a tightly bound orbit and will appear as a “single star” in late-time AO imaging. Because their separation will be small compared to the lens-source separation, this will not cause any real difficulty, but it should be kept in mind. There is a blend whose brightness is consistent with a bulge star at the base of the giant branch, but whose color is not measured. Han et al. (2022d) do not report its offset from the lens. If it is indeed a bulge giant, then it will be clearly brighter than the combined light of the sources in K band. However, if it lies the foreground, in front of a substantial fraction of the dust, then it could be of comparable brightness to the combined source light, in which case it could cause some confusion. **KMT-2021-BLG-2294** was not found by AnomalyFinder because it had $\Delta\chi^2 = 59$ (far below the threshold of 120). Hence, unless the AnomalyFinder search is modified (and this event is recovered), it will not enter the statistical sample. Note that the planetary signal is very obvious by eye in the online pySIS reductions. Nevertheless, this failure mode is quite rare and so probably does not warrant modifying the search.

6.2. Comments on Events in Table 2

6.2.1. 2016

OGLE-2016-BLG-0263 is not in the AnomalyFinder statistical sample because its best-fit solution is 2% above the formal limit $q = 0.03$. However, because the timescale is short, $t_E = 16$ day, its host is plausibly a late M dwarf (Han et al. 2017a), in which case the planet is a few Jupiter masses.

6.2.2. 2017

KMT-2017-BLG-1146: Shin et al. (2019) do not report $((V - I), I)_{S,0}$, so I have estimated $I_{S,0} = 18 - 2.5 \log(f_{S,KMTC}) - A_I$, and I have estimated $(V - I)_{S,0}$ from the colors of stars with the same I -band offset from the clump (as determined from Table 1 of Nataf et al. 2013) as those in Baade’s Window (as derived from *HST* photometry from Holtzman et al. 1998).

6.2.3. 2018

OGLE-2018-BLG-1212 has a large $\pi_E = 0.77$, which implies a proper motion $\mu_{\text{rel}} = \kappa M \pi_E / t_E \rightarrow 45(M/M_\odot) \text{ mas yr}^{-1}$. Although the Bayesian analysis disfavors masses $M > 0.3 M_\odot$, the lens-source separation could be quite high in 2030 if this inference proves to be incorrect.

KMT-2018-BLG-2602: The source is blended with a clump giant at $\Delta\theta \lesssim 10 \text{ mas}$, which is $\sim 1.4 \text{ mag}$ brighter than the source and very likely its companion. This may make it difficult to measure the source flux, even with EELT. However, if it can be measured, then using color-color relations and the invariants f_{St_E} and qt_E , it may be possible to substantially reduce the errors in q and t_E relative to those shown in Table 2. **KMT-2018-BLG-2718** has a binary-lens solution that is disfavored by $\Delta\chi^2 = 12.7$. In my view, this is sufficient to be included in a “planetary” sample for statistical study, but this is a decision that must finally be made by those carrying out such studies. If the source color (in, e.g., $(J - K)$), is measured at late times, then it may be possible to considerably reduce the errors in t_E and q using the color-color relations and the invariants f_{St_E} and $t_q = qt_E$.

6.2.4. 2019

KMT-2019-BLG-0253: The blended light is $\Delta I \sim 0.5 \text{ mag}$ and $\Delta K \sim 1 \text{ mag}$ brighter than the source. Hwang et al. (2022) argue that it is likely to be either the host or a companion to the host. Given that the color and magnitude of the source are well-measured in V/I , it is plausible that the blend could be precisely characterized by *HST* imaging in similar bands, even before the source and lens have separated. Additional work would still be required to distinguish between the host and companion-to-host scenarios. **KMT-2019-BLG-0414** cannot be considered a “secure planet” at the present time because it has an alternate (xallarap) solution that is disfavored by only $\Delta\chi^2 = 4.2$. Nevertheless, if late-time AO imaging showed that the proper-motion were sufficiently large, e.g., $\mu_{\text{rel}} \gtrsim 6 \text{ mas yr}^{-1}$,

the xallarap solution would require a companion mass $M_{\text{comp}} \gtrsim 1 M_{\odot}$, which would be inconsistent with light curve (unless the companion were a NS or BH). Hence, it is possible that such a measurement would effectively confirm the planetary solution. However, even if confirmed, this planet would not necessarily enter a statistical sample because of the large discrete ($\Delta \log q = 0.47$) and continuous ($\sigma(\log q) = 0.26$) degeneracies.

6.2.5. 2021

KMT-2021-BLG-2478: As discussed by Ryu et al. (2022b) in their Section 5.3, the apparent constraint on ρ is likely to be spurious. Hence, there are no reliable constraints on the proper motion.

6.3. Distribution of Planetary-event μ_{rel}

As I mentioned in Section 3.5, there appears to be an excess of low- μ_{rel} planetary events relative to the expectation for microlensing events as a whole. That is, as argued by Gould et al. (2021), microlensing is dominated by bulge-bulge lensing, for which the sources and lenses have both similar mean proper motions and similar dispersions σ . Hence, the μ_{rel} distribution has approximately zero mean and $\sqrt{2}\sigma$ dispersion. While σ varies somewhat according to the line of sight, Gould et al. (2021) adopted $\sigma = 2.9 \text{ mas yr}^{-1}$ as representative. Taking account of the factor μ_{rel} in the rate equation, this leads to a μ_{rel} distribution

$$p(\mu_{\text{rel}})d\mu_{\text{rel}} = \frac{\mu_{\text{rel}}^{\nu} d\mu_{\text{rel}} \exp[-(\mu_{\text{rel}}/2\sigma)^2]}{0.5[(\nu - 1)/2]!(2\sigma)^{\nu+1}}; \quad \nu = 2. \quad (22)$$

The primary concern of Gould et al. (2021) was to predict the fraction of events with proper motions below some small value of $\mu_{\text{rel}} \ll 2\sigma$, which is then $\simeq \mu_{\text{rel}}^{\nu+1}/(\nu + 1)p(0) = (\mu_{\text{rel}}/2\sigma)^{\nu+1}/[(\nu + 1)/2]! \rightarrow (\mu_{\text{rel}}/\sigma)^3/6\sqrt{\pi}$. While Equation (22) does not apply to disk stars, one does not expect these to greatly alter the low- μ_{rel} form of the distribution. First, disk lenses constitute a minority. Second, because the mean $|\langle \mu_{\text{rel}} \rangle|$ is typically of order $\sim 6 \text{ mas yr}^{-1}$, the height $p(\mu_{\text{rel}} = 0)$ for disk lenses is substantially suppressed compared to bulge lenses. Third, for small μ_{rel} , the functional form $\propto \mu_{\text{rel}}^{\nu+1}$ remains the same. Fourth, while the disk-lens proper-motion dispersion is typically smaller than the bulge dispersion, the difference is not dramatic. In brief, the contribution of disk lenses to the low- μ_{rel} population is small, and its character is not dramatically different from that of the bulge lenses. Hence, we expect that the bulge-bulge formula will be approximately correct, at least for low- μ_{rel} .

However, as noted, this appears not to be the case for the sample of 71 planetary events with proper-motion measurements that are listed in Table 1. To address this issue quantitatively, I fit the planetary events with proper-motion measurements to two-parameter models of the form of Equation (22). For this purpose I remove the two events with $\mu_{\text{rel}} \sim 15 \text{ mas yr}^{-1}$, which both have large errors and which are not accounted for by any models in this class. Most likely, they are due to incorrect measurements, but may be part of, e.g., a near-disk population. In any case, they are not directly relevant to the problem of an excess of low- μ_{rel} planetary events.

The result is shown in Figure 7. The best fit is given by

$$\nu = 1.02 \pm 0.29 \quad \sigma = 3.06 \pm 0.29 \text{ mas yr}^{-1}. \quad (23)$$

Models with $\nu = 2$ and $\sigma \simeq 3.0 \text{ mas yr}^{-1}$ are disfavored by $\Delta \ln L = 7.5$ corresponding to $\Delta \chi^2 = 15$. Given that there is a plausible physical explanation for an excess of low- μ_{rel} planetary events relative to the underlying population of events (i.e., $\Delta \chi^2 \propto \mu_{\text{rel}}^{-1}$), the balance of evidence is that the red curve in Figure 7, together with its corresponding analytic representation, is the best predictor that we currently have at present for the frequency of low- μ_{rel} planetary events. Note, further, that the free fit for (ν, σ) recovers the independently known dispersion of bulge lenses $\sigma = 2.9 \text{ mas yr}^{-1}$. If we impose this value as a prior, then the constraint on ν is even tighter: $\nu = 1.16 \pm 0.20$.

6.4. Availability of Targets

What are the prospects for making host mass measurements by AO imaging with current instruments before AO first light on 30m class telescopes (assumed here to be 2030), and what are the prospects using 30m class telescopes after first AO light?

To address the first question, I first restrict attention to dwarf sources, which I define at $I_0 - (V - I)_0 < 16$. Systems with giant sources are much more likely to have high contrast ratio, which generally requires larger separations. I then restrict consideration to the 82 hosts (of 86 planets) in Table 1, i.e., those that have either μ_{rel} measurements, or μ_{rel} lower limits. For the first, I adopt the reported value, and for the second I adopt the lower limit. I then calculate (adopting $\mu_{\text{rel, hel}} = \mu_{\text{rel}}$) the date on which the separation will reach 72 mas, i.e., 1.3 FWHM in K band on the Keck telescope. I plot the cumulative distribution in Figure 8.

This is a relatively crude proxy for the true target population as a function of time. For example, if there is a reasonable expectation that the source and host will have comparable brightness (based on Bayesian or other arguments), then they might be chosen as targets

despite having separations that are only half of this threshold. On the other hand, if similar arguments lead to an expectation of a high contrast ratio, they might not be chosen despite being separated by more than my nominal threshold.

To test this naive reasoning, I estimate the contrast ratio, expressed as a ΔK offset, with negative signs meaning that the host is brighter, for each of the 23 hosts in Figure 8. In most cases, the host brightness is taken from Bayesian host-mass and distance estimates in the discovery papers. In a few cases, it is based on mass measurements, usually from parallax, but sometimes from excess light. These are shown in vertical columns in Figure 8. These estimates show that 9 of the 23 hosts are expected to have $|\Delta K| \leq 2.5$, meaning that they probably can be resolved at 1.3 FWHM, or perhaps slightly bigger separations. Another 3 have $2.5 < |\Delta K| \leq 3.0$, and hence may be resolved at somewhat larger separations, particularly because for the largest of these three $|\Delta K|$, it is the host that is brighter. However, three have $\Delta K > 7$ and so would be completely hopeless unless the Bayesian estimates were radically incorrect, while the remaining 8 would be quite difficult. Hence, I estimate that roughly 10 of total sample of 111 planetary systems in Tables 1 and 2 can be successfully imaged prior to 30m-class AO.

To address the second question, I plot the expected separation, $\Delta\theta$, in 2030 versus K_0 in Figure 9 for the 71 planetary events with μ_{rel} measurements. The K_0 magnitude is important because intrinsically brighter sources will generally have larger source-lens contrast ratios, which may require larger $\Delta\theta$ to resolve. There are only two cases (OGLE-2018-BLG-1647 and OGLE-2016-BLG-1227) with $\Delta\theta < 15$ mas, and only three others (KMT-2021-BLG-1077, KMT-2017-BLG-2509, and KMT-2021-BLG-0712) with $\Delta\theta < 20$ mas. Moreover, four of these five are relatively faint. Sources with high contrast ratio probably require separations $\Delta\theta \gtrsim 5 \times \text{FWHM}$, which would be 70 mas for EELT in the K -band. Note that there are 10 potential targets with $K_0 < 15.5$ and $\Delta\theta < 80$ mas, which may be difficult. In this context, it is notable that 5 of these 10 have *Spitzer*-based parallax, which may be helpful in extracting masses in the case on non-detections.

The lower panel of Figure 9 shows a histogram of the same 71 sources with μ_{rel} measurements in black. It also shows, in red, a histogram of the 40 sources without μ_{rel} measurements, which is scaled to have the same total area as the black histogram. The two distributions look qualitatively similar. This is mildly surprising because one might have guessed that brighter (so bigger) sources would be more likely to intersect caustics and, more generally, to be more likely to yield measurable finite-source effects. However, if this is the case, the effect is not sufficiently strong to show up in a sample of this size. On the other hand, there is a countervailing effect that, other things being equal, the featureless structures in non-caustic-crossing events have lower χ^2 , so they will more easily meet a given χ^2 threshold

for bright sources.

7. Application to Other Statistical Samples

The approach outlined in this paper to transform a statistical sample of q measurements into a statistical sample of M_{planet} measurements could be applied to other samples. Here I discuss four samples, including three completed and one prospective.

7.1. High-Magnification Follow-Up Survey (2005-2008)

Gould et al. (2010) constructed a planet sample from discoveries made by the Microlensing Follow Up Network (μ FUN) by intensive followup observations of high-magnification events that were discovered by OGLE and MOA from 2005-2008. The process of organizing this followup was somewhat chaotic, but Gould et al. (2010) argued that the resulting sample of $A_{\text{max}} > 200$ events could be considered well-defined because they were uniformly selected from all $A_{\text{max}} > 200$ events. They detected 6 planets in 5 events, out of a total of 13 events in their full sample. The 13 events are listed in their Table 1.

Of the 5 planetary events (containing 6 planets), 4 events (5 planets) already have mass measurements, either from $M = \theta_E/\kappa\pi_E$ light-curve analyses or from high resolution follow-up observations. **OGLE-2005-BLG-169** (Gould et al. 2006) was subsequently resolved by Batista et al. (2015) and Bennett et al. (2015), using Keck and *HST* respectively, and was determined to have $M_{\text{host}} = 0.65 \pm 0.05 M_{\odot}$, $M_{\text{planet}} = 13.2 \pm 1.2 M_{\oplus}$, and $D_L = 4.0 \pm 0.4$ kpc. **OGLE-2006-BLG-109** was already known to have $M_{\text{host}} = 0.51 \pm 0.05 M_{\odot}$, $M_{\text{planet}} = 231 \pm 19 M_{\oplus}$, $M_{\text{planet}} = 86 \pm 7 M_{\oplus}$, and $D_L = 1.51 \pm 0.12$ kpc based on the previous analyses of Gaudi et al. (2008) and Bennett et al. (2010), which included both light-curve based $M = \theta_E/\kappa\pi_E$ and unresolved Keck AO follow-up observations. **OGLE-2007-BLG-349** was subsequently analyzed by Bennett et al. (2016) based on a combination of the $M = \theta_E/\kappa\pi_E$ light-curve method and already existing *HST* data and found to have $M_{\text{host}} = 0.41 \pm 0.07 M_{\odot}$, $M_{\text{planet}} = 80 \pm 13 M_{\oplus}$, and $D_L = 2.7 \pm 0.4$ kpc. Note that this is a circumbinary planet. The mass of the stellar companion is $M_{\text{companion}} = 0.30 \pm 0.07 M_{\odot}$. **MOA-2007-BLG-400** (Dong et al. 2009b) was subsequently resolved via Keck AO follow-up observations by Bhattacharya et al. (2021) and found to have $M_{\text{host}} = 0.69 \pm 0.04 M_{\odot}$, $M_{\text{planet}} = 544 \pm 86 M_{\oplus}$, and $D_L = 6.9 \pm 0.8$ kpc.

Of the 6 planets, only MOA-2008-BLG-310 (Janczak et al. 2010) lacks a mass measurement. While Gould et al. (2010) list a mass measurement based on excess light de-

tected when the lens and source were superposed, Bhattacharya et al. (2017) subsequently showed that this excess light was inconsistent with being the lens. We note that because $\mu_{\text{rel}} = 4.85 \pm 0.15 \text{ mas yr}^{-1}$ (Bhattacharya et al. 2017), the lens and source will be separated by $\Delta\theta = 73 \pm 2 \text{ mas}$ in 2023. Hence, it is possible in principle that the lens and source could be separately resolved “now” using Keck AO. However, based on the original *H*-band light-curve measurements, $H_S = 17.69 \pm 0.03$ (corresponding to $K_S = 17.8$), while Bhattacharya et al. (2017) did a Bayesian analysis that included the flux constraints from their *HST* measurements and derived $M_{\text{host}} = 0.21 \pm 0.14$ and $D_L = 7.7 \pm 1.1 \text{ kpc}$. At the mean values, the expected host magnitude is $K_{\text{host}} \sim 22.3$, i.e., $\Delta K = 4.5$, which would require much greater separations, probably implying that the host and source will only be resolved at first AO light on 30m class telescopes.

Nevertheless, as nearly all of this sample has mass measurements, it is instructive to plot their values, which I do in Figure 10 (black).. For this purpose, I plot MOA-2008-BLG-310 at its Bayesian estimates: $M_{\text{host}} = 0.21 \pm 0.14$, $M_{\text{planet}} = 162 \pm 108 M_{\oplus}$ and $D_L = 7.7 \pm 1.1 \text{ kpc}$.

A naive conclusion from Figure 10 would be that 2/3 of all microlensing planets are in the near disk, $D_L \lesssim 4 \text{ kpc}$, and that 2/3 have host masses $M_{\text{host}} \gtrsim 0.5 M_{\odot}$. Of course, these interpretations would be ignoring the large Poisson uncertainties. However, they would also be ignoring a strong sample bias, which must be accounted for prior to making a statistical analysis.

Note from Table 1 of Gould et al. (2010) that the underlying sample has a median and 68% timescale range of $t_E = 26_{-16}^{+95} \text{ day}$. The median and 1σ lower limit are rather typical of microlensing survey samples, but there is a long tail toward long and very long events. It is notable that three of the six planets were discovered in the two longest events. While the underlying population of $A_{\text{max}} > 200$ events is certainly directly proportional to the number of events at all timescales, there is likely a bias toward long events with $A_{\text{max}} > 200$ being detected in the surveys and then being recognized in time to conduct follow-up observations over the peak. This could be taken into account by directly using the distribution of the observed timescales combined with the planet sensitivity functions presented by Gould et al. (2010) for the events of various timescales. Note, for example, that the two least sensitive events (their Figure 4) are among the shortest, OGLE-2005-BLG-188 ($t_E = 14 \text{ day}$) and MOA-2008-BLG-105 ($t_E = 10 \text{ day}$). If, as an exercise, I remove these two events, as “effectively non-sensitive”, then the median rises to $t_E = 43 \text{ days}$, which is not at all typical of microlensing samples. Because $t_E \equiv \theta_E/\mu_{\text{rel}}$, a systematic bias toward long events favors slow proper motions and large Einstein radii, and the latter requires large masses and/or nearby lenses, i.e., just the “naive results” mentioned above.

While the selection bias is only directly caused by t_E (and not the physical parameters

that enter it), it would be of some interest to know the lens masses and distances for the 8 non-planetary events. As noted by Gould et al. (2010), three of these events already have such measurements: OGLE-2007-BLG-050 (Batista et al. 2005), OGLE-2007-BLG-224 (Gould et al. 2009), and OGLE-2008-BLG-279 (Yee et al. 2009). Of the remaining 5 events, only one has a proper motion measurement, OGLE-2005-BLG-188 ($\mu_{\text{rel}} \sim 4.5 \pm 0.5 \text{ mas yr}^{-1}$).

7.2. OGLE-MOA-Wise Survey (2011-2014)

Shvartzvald et al. (2016) monitored the richest 8 deg^2 of microlensing fields from the Wise observatory 1m telescope in Israel during the central portions of four seasons, 2011-2014, and then analyzed the 224 events that were discovered by OGLE and MOA and that occurred in this area. The cadence of the Wise observations was $\Gamma \sim 2 \text{ hr}^{-1}$, compared to $\Gamma \sim 4 \text{ hr}^{-1}$ for MOA and $\Gamma \sim 4 \text{ hr}^{-1}$ and $\Gamma \sim 1.3 \text{ hr}^{-1}$ for OGLE. The goal was to carry out an objective survey with (weather permitting) roughly continuous coverage, i.e., similar to the subsequent goal of KMTNet but on a smaller scale. While the total number of planets found in this survey (8) was more than an order of magnitude smaller than will come from the 6-year KMT survey described above, it has, in the present context, the significant advantage that its median t_0 is about 6 years earlier, which should provide a similar advantage as to when the lenses and sources can first be resolved using current instruments.

Moreover, this sample has the important advantage that there are first-epoch AO images for 5 of these 8 events when the lenses and sources were still superposed, 3 using the 6.5-m Magellan adaptive optics system (MagAO; Close et al. 2012; Males et al. 2014; Morzinski et al. 2014) in a follow-up project to systematically characterize the planet hosts of this sample (Xie et al. 2021; Xie 2021) and two others using Keck (Batista et al. 2014; Beaulieu et al. 2018). [All 3 of the unobserved targets have good π_E measurements, with one of these having a giant-star source, i.e., not susceptible to the excess-flux method.] These images may be useful to understand various issues when they are compared to late-time AO imaging. Thus, in addition to being an independent study, it also may provide more general insights that could not be obtained from events that lack such imaging.

Shvartzvald et al. (2016) carried out only semi-automated planet detection for this sample and so did not vet these candidates at the same level as did the references to Tables 1 and 2. Nevertheless, other workers did carry out such analyses, including the exclusion of systems that were not actually planetary. I should note that Shvartzvald et al. (2016) also presented all the non-planetary (“binary”) candidates in their sample. These could be the subject of an additional study, but I do not include them here. Below I present notes on these 8 events.

MOA-2011-BLG-293: Batista et al. (2014) observed this target on 13 May 2012 using Keck AO and detected about twice as much H -band light as was expected from the source. They show that there is only a few percent probability that this excess is due to a companion to the source or host, and negligible probability that it is due to an ambient star. They obtained $M_{\text{host}} = 0.86 \pm 0.06 M_{\odot}$, $M_{\text{planet}} = 1526 \pm 95 M_{\oplus}$, and $D_L = 7.72 \pm 0.44$ kpc. Still it would be of interest to probe the first two possibilities. Because the blend and source have equal brightness, they can be resolved when separated by about 35 mas (Bhattacharya et al. 2018). Hence, if the blend is the host, they were already resolvable beginning 2019. If the blend is a companion to the host, this would also be true unless the original separation were about 35 mas and opposite to the direction of $\mu_{\text{rel, hel}}$. However, in this case, the blend would have almost certainly been resolved by Batista et al. (2014). Thus, if Keck AO observations done “today” did not resolve the source and blend, they would almost certainly be companions. Such an observation might rigorously exclude that the blend is a companion to the host, but if not, this could be done by taking another observation a few years later. If the proper motion derived from these two observations “points back” sufficiently close to the source, then a putative host companion would have had to have been so close to the host that it would have created an additional bump in the light curve.

MOA-2011-BLG-322: Shvartzvald et al. (2014) did not measure the offset between the blend and the source. Because the blend is a very rare foreground star (with subsequent *Gaia* parallax $\pi = 0.53 \pm 0.14$ mas), they considered that it might be the host or a companion to the host, although they did not consider these scenarios to be likely. However, Xie (2021) did measure this offset, finding ~ 750 mas, which rules out the “host = blend” hypothesis. If the blend is a companion to the host, it lies 1400 au from it in projection, i.e., with a period $\log(P/\text{day}) \sim 7.5$. Roughly 9% of G dwarfs have companions with such periods or larger (Duquennoy & Mayor 1991), so this would not be unusual. Xie (2021) also found that the target was consistent with no excess K -band flux relative to that expected from the source, and thereby placed an upper limit $M_{\text{host}} < 0.6 M_{\odot}$, consistent with the Bayesian expectations of Figure 5 from Shvartzvald et al. (2014). It would be reasonable to attempt Keck AO observations at $\Delta\theta \sim 72$ mas, but given the crude ρ measurements, one cannot say very precisely when that will be. Nevertheless, adopting the best fit $\mu_{\text{rel}} = 4.7 \text{ mas yr}^{-1}$ would imply 2027.

OGLE-2011-BLG-0265 has very precise parallax measurements, but these differ substantially between the two solutions, leading to different host masses, $0.21 M_{\odot}$ or $0.14 M_{\odot}$, and distances 4.4 kpc or 3.5 kpc (Skowron et al. 2015). Hence, the system characteristics are approximately known, but could be improved by late-time AO observations. However, because the host is a giant, $K_{S,0} \sim 14$ and the proper motion is low ($\mu_{\text{rel}} = 2.9 \pm 0.3 \text{ mas yr}^{-1}$), this would not be feasible prior to 30m class AO.

OGLE-2013-BLG-0341 has an excellent parallax measurement, which yields a host

mass, planet mass and system distance of $M_{\text{host}} = 0.145 \pm 0.013 M_{\odot}$, $M_{\text{planet}} = 2.32 \pm 0.27 M_{\oplus}$, and $D_L = 1.16 \pm 0.09 \text{ kpc}$ (Gould et al. 2014). The companion to the host, which (in 2013) lay projected at about 15 mas, would be brighter than the host: $K_{\text{companion}} = 18.1$ and $K_{\text{host}} = 18.6$. These should be compared to $K_S \sim 15.2$ for the source. Thus, there would be a net offset of $\Delta K = 2.7$. Hence, the lens and (binary) source (with $\mu_{\text{rel}} = 10.2 \pm 0.8 \text{ mas yr}^{-1}$) could be separately resolved by Keck AO, either now or in a few years. Assuming (as argued by Gould et al. 2014) that the wide binary solution is correct, the two components could probably be imaged by EELT AO. **OGLE-2013-BLG-0911** has a good parallax measurement, yielding a host mass, planet mass and system distance of $M_{\text{host}} = 0.29 \pm 0.08 M_{\odot}$, $M_{\text{planet}} = 3080 \pm 900 M_{\oplus}$, and $D_L = 3.2 \pm 0.5 \text{ kpc}$ (Miyazaki et al. 2020). If correct, these would imply $K_{\text{host}} = 19.9$, compared to $K_S \sim 17.5$ for the source, yielding $\Delta K = 2.4$. Thus, it would be difficult to resolve the host and blend with current instruments even in 2030, when they will be separated by $\Delta\theta \sim 40 \text{ mas}$. Hence, it would appear best to wait for 30m class AO. **OGLE-2013-BLG-1721**: Xie (2021) measured the baseline object (source + lens) to be $K = 18.04 \pm 0.07$. She did not report this because the position seemed to be displaced from the OGLE position by $\sim 89 \text{ mas}$. However, first, reanalysis by Subo Dong (2022, private communication) shows that the offset is substantially smaller (58 mas), although this is still larger than would be expected. Second, my prediction for the source flux, based on the event parameters reported by Mróz et al. (2017b) is $K_S = 18.62 \pm 0.23$. One possible explanation is that there is a fairly large astrometric error of unknown origin, in which case there is $\sim 3\sigma$ detection of excess flux, i.e., $K_{\text{blend}} = 19.00 \pm 0.37$. This would be consistent with my estimate for the lens flux $K_L = 20.3$, based on the median Bayesian prediction (also with large uncertainty) of Mróz et al. (2017b), i.e., $M_{\text{host}} = 0.46 M_{\odot}$, $D_L = 6.3 \text{ kpc}$, and $A_K = 0.29$. Another explanation is that the excess light is due to a companion to the lens or source that lies at a separation of $140 \pm 45 \text{ mas}$ and therefore would not be resolved (for a substantial fraction of this 1σ range) in the FWHM $\sim 165 \text{ mas}$ seeing of the MagAO images. Because of this ambiguity, all we can really say is that the flux measurement by Xie (2021) is consistent with the Bayesian estimates, but does not further modify them. The proper motion is $\mu_{\text{rel}} = 5.5 \pm 1.1 \text{ mas yr}^{-1}$, while the median predicted contrast ratio in K is 4.7, i.e., $\Delta K = 1.7$. Hence, it is plausible that the source and lens might be separately resolved when they are separated by $\sim 70 \text{ mas}$, i.e., in 2026, although this is far from guaranteed.

OGLE-2014-BLG-0124 has an excellent parallax measurement from *Spitzer* (Yee et al. 2015), yielding a host mass, planet mass and system distance of $M_{\text{host}} = 0.71 \pm 0.22 M_{\odot}$, $M_{\text{planet}} = 162 \pm 51 M_{\oplus}$, and $D_L = 4.1 \pm 0.6 \text{ kpc}$. Keck AO imaging by Beaulieu et al. (2018) detected excess light from the superposed source and host, and thereby refined these measurements to $M_{\text{host}} = 0.90 \pm 0.05 M_{\odot}$, $M_{\text{planet}} = 207 \pm 13 M_{\oplus}$, and $D_L = 3.5 \pm 0.2 \text{ kpc}$. As

discussed in Section 4.1, single-epoch photometric mass measurements are subject to ambiguity because the blend light could come from a more massive companion to the host. This applies more strongly to excess-light mass measurements because there is no simultaneous measurement of θ_E . See Bhattacharya et al. (2017) for an example. In the present case, the light-curve based θ_E measurement has a 31% error, which is the primary source of error in the original M_{host} and M_{planet} measurements. Hence, it remains possible, in principle, that the $0.9 M_\odot$ star detected by Keck is a companion to the host, while the actual host is, e.g., $0.5 M_\odot$ and so does not contribute substantially to the blend light. Thus, it would still be useful to separately resolve the source and the blend. Based on the highly anti-correlated measurements of $\pi_E = 0.146 \pm 0.004$ and the projected velocity $\tilde{v}_{\text{hel}} = 107 \pm 3 \text{ km s}^{-1}$ (Udalski et al. 2015), we can expect $\mu_{\text{rel,hel}} = \kappa M \pi_E^2 \tilde{v}_{\text{hel}} / \text{au} = (3.8 \pm 0.1)(M/M_\odot) \text{ mas yr}^{-1}$. Thus, if the star seen by Keck is truly the host, then $\mu_{\text{rel,hel}} = 3.4 \pm 0.2 \text{ mas yr}^{-1}$. Because the contrast ratio inferred from Beaulieu et al. (2018) is about 2:1, the host and blend should be resolvable with Keck AO at $\Delta\theta \sim 40 \text{ mas}$, i.e., in 2026. If they are resolved, it will lead to an even more precise mass measurement. If they are not, it will show that the blend is a companion to the host and thus requires an additional observation with 30m class AO.

OGLE-2014-BLG-0676: Xie et al. (2021) measured the combined lens+blend light to be $K_{\text{base}} = 16.72 \pm 0.04$ at Magellan and in $J_{\text{base}} = 17.73 \pm 0.03$ at Keck. Because the source is extremely faint ($K_S = 19.7 \pm 0.2$), most of this light is due to the blend: $K_B = 16.79 \pm 0.04$ and $J_B = 17.76 \pm 0.03$. Their analysis showed that the “blend=host” hypothesis is favored over other scenarios by more than 100:1 and derived a host mass, planet mass and system distance of $M_{\text{host}} = 0.73^{+0.14}_{-0.29} M_\odot$, $M_{\text{planet}} = 1170^{+220}_{-458} M_\oplus$, and $D_L = 2.7^{+0.8}_{-1.4} \text{ kpc}$. They note that the large errors are due to the large error in θ_E from the light curve analysis. This could be greatly improved by separately resolving the host and blend. However, given the high contrast ratio and relatively low proper motion, $\mu_{\text{rel}} = 4.3 \pm 1.3 \text{ mas yr}^{-1}$, this may not be possible until 30m class AO is available.

In brief, the OGLE-MOA-Wise survey planet-mass measurements are mostly complete. Of the 8 planet/host systems, 6 have mass determinations that are based either on good parallax measurements or measurement of excess of flux (or both). The only two that lack such measurements are MOA-2011-BLG-322, for which the imaging provided only upper limits on the host mass $M_{\text{host}} < 0.6 M_\oplus$ (corresponding to $M_{\text{planet}} < 18 M_{\text{Jup}}$) and OGLE-2013-BLG-1721, for which the Xie (2021) measurement was consistent with the Bayesian estimates but did not further modify them. Some of the other planets have relatively large errors, many of which could be improved by additional imaging in the future. However, these errors are still small compared to those of typical microlensing planets, which usually only have Bayesian estimates. I show the masses of the hosts and planets in Figure 10 (magenta). For MOA-2011-BLG-322, I adopt $M_{\text{host}} = 0.4 \pm 0.2 M_\odot$, $M_{\text{planet}} = 3800 \pm 1900 M_\oplus$, and $D_L =$

7.6 ± 0.9 kpc, after considering the Bayesian analysis of Shvartzvald et al. (2014) and the flux limits of Xie (2021). For OGLE-2013-BLG-1721, I adopt $M_{\text{host}} = 0.46_{-0.23}^{+0.26} M_{\odot}$, $M_{\text{planet}} = 204_{-99}^{+111} M_{\oplus}$, and $D_L = 6.3_{-1.6}^{+1.1}$ kpc from the Bayesian analysis of Mróz et al. (2017b). In all cases, I symmetrize the error bars for the plot.

It is striking that 5 of the 8 planets have hosts in the near disk, $D_L \lesssim 4$ kpc, a very similar proportion to the 4 out of 6 planets from the high-magnification sample. However, while I pointed out that the high-magnification sample could be subject to selection bias that favors such nearby planets, I know of no such argument that could be applied to the OGLE-MOA-Wise survey. Moreover, none of the distances of the 9 “nearby” ($D_L \lesssim 4$ kpc) planets from either survey rely on Bayesian estimates.

Thus, Figure 10 can be regarded as “suggestive evidence” that planets may be more common in the nearby disk than in the bulge and the more distant disk. Unfortunately, however, the sample is too small to draw strong conclusions on this issue.

7.3. MOA Survey (2007-2012)

Suzuki et al. (2016) analyzed 22 “clear planets” that were objectively found from the MOA survey during the six year period 2007-2012. These are listed in their Table 2. In addition, they found one companion, in the event OGLE-2011-BLG-0950, that was ambiguous between a planetary and binary solution, which was subsequently confirmed to be a binary by Keck AO resolution (Terry et al. 2022). Thus, the sample contains 22 planets in total. The main goal of that paper was to estimate the distributions of q and s . Here I focus on the prospects of measuring masses for individual events.

As discussed by Suzuki et al. (2016), 7 events already had mass measurements at the time of publication. One of these, **OGLE-2007-BLG-349**, overlaps the Gould et al. (2010) sample. It already has a mass measurement, as discussed in Section 7.1. Another event, **OGLE-2011-BLG-0265**, overlaps the Shvartzvald et al. (2016) sample. It also has a mass measurement, as discussed in Section 7.2.

I recapitulate the remaining five. **MOA-2007-BLG-192** (Bennett et al. 2008) has $M_{\text{host}} = 0.060_{-0.021}^{+0.028} M_{\odot}$, $M_{\text{planet}} = 3.3_{-1.6}^{+4.9} M_{\oplus}$, $D_L = 1.0 \pm 0.4$ kpc, from the light-curve based $M = \theta_E / \kappa \pi_E$ method. **MOA-2009-BLG-266** (Muraki et al. 2011) has $M_{\text{host}} = 0.56 \pm 0.09 M_{\odot}$, $M_{\text{planet}} = 10.4 \pm 1.7 M_{\oplus}$, $D_L = 3.04 \pm 0.33$ kpc, from the light-curve based $M = \theta_E / \kappa \pi_E$ method. **MOA-2010-BLG-117** (Bennett et al. 2018a) has $M_{\text{host}} = 0.58 \pm 0.11 M_{\odot}$, $M_{\text{planet}} = 172 \pm 32 M_{\oplus}$, $D_L = 6.9 \pm 0.7$ kpc, from the light-curve based $M = \theta_E / \kappa \pi_E$ method. **MOA-2010-BLG-328** (Furusawa et al. 2013) has $M_{\text{host}} = 0.11 \pm 0.01 M_{\odot}$,

$M_{\text{planet}} = 9.2 \pm 2.2 M_{\oplus}$, $D_L = 0.81 \pm 0.10$ kpc, from the light-curve based $M = \theta_E / \kappa \pi_E$ method. **OGLE-2012-BLG-0950**: In this case, the original excess-light based determinations by Koshimoto et al. (2017a), which were summarized by Suzuki et al. (2016), have been superseded by Bhattacharya et al. (2018), who resolved the source and lens using *HST* and Keck AO. They found $M_{\text{host}} = 0.58 \pm 0.04 M_{\odot}$, $M_{\text{planet}} = 39 \pm 8 M_{\oplus}$, $D_L = 2.19 \pm 0.23$ kpc.

Note that the mass measurement of MOA-2007-BLG-192 has large uncertainties. The host is plausibly a BD at 3 kpc. If so, further refinement will have to await 30m class AO. For MOA-2010-BLG-328, Furusawa et al. (2013) caution that the unusually low mass and distance could be due to xallarap being misconstrued as parallax, and they point out that this concern could be addressed by future AO follow-up observations. They report $\mu_{\text{rel}} = 5.7 \pm 0.7 \text{ mas yr}^{-1}$ and $K_{S,0} = 16.89$ (implying $K_S = 17.13$). For their parallax-based solution, they predict $K_{\text{host}} = 19.42 \pm 0.47$, i.e., $\Delta K = 2.29 \pm 0.47$. If the low estimates of the mass and distance were due to xallarap, the host would be brighter, so the contrast ratio would be more favorable. Hence, Keck AO observations in 2023, when $\Delta\theta = 74 \pm 9$ mas would resolve the source and lens if the xallarap model were correct, thus yielding revised mass and distance measurements. If such observations failed to resolve the source and lens separately, they would confirm the parallax model. Thus, this ambiguity can already be resolved.

Of the remaining 15 planetary events, only one has a published mass measurement: **MOA-2009-BLG-319** (Miyake et al. 2011) was resolved with Keck AO by Terry et al. (2021), who found $M_{\text{host}} = 0.52 \pm 0.04 M_{\odot}$, $M_{\text{planet}} = 67 \pm 6 M_{\oplus}$, $D_L = 7.1 \pm 0.7$ kpc.

Another event, **MOA-2013-BLG-322** was observed using Magellan by Xie (2021), who found only upper limits on the host flux. As I discussed in Section 7.2, it may be possible to resolve the source and lens beginning about 2027, but this is far from certain.

Three events are very unlikely to be resolved before 30m class AO is available because they are too bright. **MOA-2010-BLG-028** and **MOA-2012-BLG-006** both have giant-star sources, while **MOA-2010-BLG-353** has an unusually red sub-giant source, which likely has $K_0 \simeq 13.6$, i.e., nearly as bright as a clump giant.

This leaves $22 - 8 - 1 - 3 = 10$ events whose prospects should be evaluated more closely. One of these 10, **MOA-2012-BLG-355** appears from Suzuki et al. (2016) to have a proper-motion measurement, but this measurement is not reported in that work, and there is no published analysis of this event. Hence, I ignore it here. For each of the remaining 9 events, I evaluate their predicted separation, $\Delta\theta$, in 2030 by adopting (from the listed reference) the best estimate of μ_{rel} and assuming $\mu_{\text{rel, hel}} = \mu_{\text{rel}}$, and I evaluate the magnitude offset, ΔK between the host and the source by adopting the most likely mass and distance according to

its published Bayesian analysis. These 9 events are listed in order of my rough estimate of how easy they would be to resolve before 2030. If the Bayesian estimates are approximately correct, then Keck AO observations prior to 2030 of the first two of these events should be straightforward, the last four will be difficult, and the remaining three may be feasible. Thus of the 22 “clear planets” from Suzuki et al. (2016), about 12 will plausibly have mass and distance measurements before the advent of 30m class AO, i.e., 6 with π_E measurements, two that were resolved by Keck AO, and perhaps 4 more that will be accessible to 8m-class AO before 2030. As anticipated, this is a far larger fraction than can be expected from the KMT sample by that date (see Section 6). However, given that the parallax subsample is heavily biased toward nearby and/or low-mass lenses (because $\pi_E^2 \propto \pi_{\text{rel}}/M$), it would be difficult to draw firm conclusions from such a partial list of planet mass and distance measurements.

Hence, apart from the tentative conclusions that might be drawn from the relatively small high-magnification (6) and OGLE-MOA-Wise (8) surveys, which already have mostly complete mass measurements, comprehensive catalogs of microlensing planets with masses and distances will have to await 30m class AO.

7.4. *Roman* Microlensing Survey (2027-2032)?

The *Nancy Grace Roman Telescope* (*Roman*) is currently scheduled for launch “no earlier” than 2026. During its nominal 5 year mission, it will carry out a series of dedicated microlensing campaigns, primarily using a broad *H*-band filter, with a fraction of observations taken in a different band to measure source colors. Currently, the plan is for 6 such campaigns, each lasting 72 days. See Penny et al. (2019) and Johnson et al. (2022) for predictions of its yield in bound planets and free-floating planets, respectively.

Roman is expected to measure host masses and distance for a much larger fraction of the bound planets that it detects than ground-based surveys. There are three principal reasons for this enhanced anticipated performance.

First, the source stars will be fainter (a natural consequence of a much deeper survey over a much smaller area, $\sim 2 \text{ deg}^2$), while the population of host-star lenses will be similar. This means that the excess flux due to the host will be measurable in a substantially larger fraction of cases. Under the assumption that the host accounts for this excess flux, its color and magnitude will, by themselves, significantly constrain the host mass and distance. In many cases (see below), there will also be θ_E measurements, which (under the same assumption) will substantially improve these mass and distance determinations.

Second, during the lifetime of the mission, which plausibly could be extended to 10

years, the image from the combined source-host light will become extended as they gradually separate (or, for planets found near the end of the mission, will become less extended). For cases that this can be measured, it will give at least the direction of $\boldsymbol{\mu}_{\text{rel}}$ (possibly up to a sign ambiguity). Provided that the lens and host colors differ sufficiently, it could give the magnitude of $\boldsymbol{\mu}_{\text{rel}}$ as well (in which case the ambiguity would also be resolved). See Bennett et al. (2006). Then, one would obtain $\theta_{\text{E}} = \mu_{\text{rel}} t_{\text{E}}$ even for the cases for which this quantity was not measured from the event.

Third, *Roman*’s high photometric stability and long-duration observing campaigns will enable 1-D parallax measurements ($\pi_{\text{E},\parallel}$). When these are combined with the direction of $\boldsymbol{\mu}_{\text{rel}}$ (same as direction of $\boldsymbol{\pi}_{\text{E}}$), these yield $\boldsymbol{\pi}_{\text{E}}$, which can be combined with θ_{E} to yield $M = \theta_{\text{E}}/\kappa\pi_{\text{E}}$ and $\pi_{\text{rel}} = \theta_{\text{E}}\pi_{\text{E}}$. See Gould (2014).

However, there will be many bound planets for which the host mass and distance cannot be determined from *Roman* observations alone, and ambiguities will remain about a substantial fraction of those that are “basically measured”.

First, θ_{E} will not be measured from the light curve for a substantial fraction planetary events. As mentioned in Section 3.1, Zhu et al. (2014) predicted that half of all planetary events from a “KMT-like” survey would lack caustic crossings, and this estimate was confirmed by Jung et al. (2022) for the only complete-year sample (i.e., 2018) of KMT planets published to date. It was further confirmed by Zang et al. (2023a) for the 4-year complete sample of low- q KMT planets. Some events without caustic crossings nevertheless yield θ_{E} measurements, primarily when the source crosses a ridge that extends from a cusp. Nevertheless, for the KMT sample, about 1/3 still lacked θ_{E} measurements. This provides our best estimate at present for the fraction of *Roman* bound planets that will lack θ_{E} measurements from the light curve.

Second, from Figure 12 of Penny et al. (2019), $\sim 1/3$ of all planets will have flux ratios $f_{\text{B}}/f_{\text{S}} < 0.1$. Unambiguous interpretation of such signals will be extremely difficult, in part because the source-flux parameter may not be measured with substantially greater precision and in part because the surface density of ambient stars increases at faint magnitudes.

Third, while many events will have 1-D parallax measurements, this is far from universal. See Gould & Zhu (2016).

Fourth, all mass determinations that are based on excess flux are subject to spurious host identifications due to brighter stellar companions to the lens and/or companions to the source. In individual cases, various arguments can be made to exclude, or at least greatly restrict, these possibilities, but in many other cases, the only counter-arguments are statistical. For example, if a G dwarf is superposed on the source, the chance that it

has some fainter companion is about 70%. The chance that this companion is what gave rise to the microlensing event scales as the square root of the mass ratio Q , so perhaps $\sqrt{Q}/(1 + \sqrt{Q}) \sim 40\%$ on average. If the projected separation is too high, the astrometric offset between the source and baseline object can be detected. This limit will vary by event, but I use 10 mas here for illustration. If the companion is too close, then it would have given rise to microlensing effects during the event. Again this will vary but I use $2\theta_E \sim 1$ mas for illustration. This leaves 2 decades in separation, so 3 decades in period, or about half of the period distribution for G dwarfs. In this example, there would be a $\sim 0.6 \times 0.4 \times 0.5 = 12\%$ chance that the event was actually due to an unseen companion. There could be additional arguments based on measurements of θ_E and $\pi_{E,\parallel}$. Nevertheless, incorrect identifications do occur, as demonstrated by the case of MOA-2008-BLG-310 (Bhattacharya et al. 2017).

In brief, of order 1/3 of hosts will not generate sufficient excess flux to enable mass measurements, and these will be overwhelmingly concentrated among low-mass hosts. In addition, a substantial fraction of mass determinations that rely on excess flux will have a residual uncertainty (although relatively small) that the excess light is not due to the host. Late time 30m class AO observations can clarify both classes of events.

For simplicity, I identify $f_B/f_S < 0.1$ as the limit beyond which the mass cannot be determined from an excess-flux measurement. Then, from Figure 12 of Penny et al. (2019), about half of these cases will have host-source flux offsets in the range $2.5 < \Delta H < 3.75$ and almost all the rest will have $3.75 < \Delta H < 5$. As mentioned above, for both classes, about 2/3 will have μ_{rel} measurements, and I will initially restrict attention to these. The first (brighter) class of lenses probably will require separations of about 2 FWHM, i.e., ~ 30 mas for K -band observations with EELT. Hence, they require wait times of $\Delta t \sim 5 \text{ yr} (\mu_{\text{rel}}/6 \text{ mas yr}^{-1})^{-1}$, where μ_{rel} is the measured proper motion. That is, some measurements could begin about 4 years after the start of the mission, and a large fraction could be completed within 8 years of the end of the mission. The second (fainter) class of lenses might require separations of up to 5 FWHM. At present, it is difficult to estimate this limit in the absence of empirical evidence about instrument performance. However, based on this estimate, the wait times would be up to 2.5 times longer.

For the events without θ_E measurements, one might adopt a moderately conservative lower limit, $\mu_{\text{rel}} \gtrsim 3 \text{ mas yr}^{-1}$, in which case the wait time would be about 10 years.

The cases with well-detected excess flux will generally have more favorable contrast ratios, and can mostly be observed at separations of 0.5–1.3 FWHM. Probably, it will be sufficient to spot check these events, to determine the scale of the problem of false host identifications. Because the wait times will typically be short, it should be possible to gain an understanding of the scale of this problem quickly.

8. Discussion: Pont du Gard

With the advent of 30m-class telescopes, it will “suddenly” become possible to make mass measurements of the great majority of microlensing planets only 5–10 years after their discovery. Coincidentally, first AO light on these telescopes is expected about a decade after the discovery of about 150 planets from the first six full seasons of the KMTNet experiment. By contrast, using the ~ 4 times smaller current-generation telescopes, one would have to wait 20-40 years, i.e., until roughly 2050 to obtain a relatively complete set of planet-mass measurements.

The bulk of the present paper is motivated by and built around the prospect of exploiting this coincidence to “rapidly” obtain a measurement of the planet mass function over this large parameter space. A striking feature of this prospect is that it rests on two completely different types of scientific initiative, i.e., the massive 8-yr observational and data-analysis effort of KMTNet (including commissioning year and Covid-19-induced 2020 semi-hiatus) and the construction of massive next-generation telescopes with advanced instrumentation. In terms of capital costs, ELTs are larger by 100:1, i.e., \$1 billion versus \$10 million. However, in terms of amortized capital plus operations, the sign of the imbalance is reversed: 1:10. That is, estimating that 100 hours of observations are required (out of 40,000 hours of an initial 20-year telescope “lifetime”) and approximating the operational and amortization costs as equal, the comparison is \$50 million for the KMT project versus \$5 million for the AO followup.

The very high capital costs and the modest amortization/operations costs of the AO follow-up (compared to the those of the KMTNet project) inspires me to ask: how, and under what conditions, can this planet mass function measurement be made if ELTs are not built. It is always useful to consider such questions, if only to help understand the different possible paths to achieving a given scientific goal. However, under present conditions, it is quite possible that public support for science, and astronomy in particular, may radically decline, perhaps for an extended period. This may seem unthinkable to scientists immersed in our work, but in my own locale, which is undertaking the largest and nearest-to-completion of these ELTs, there are active plans (as of August 2022) to ration heating and to close factories, and there is wide discussion of possible food shortages. Under such conditions, 30m-class telescopes may come to appear as an unaffordable luxury. Neither does the overall trajectory of events necessarily portend improvement.

The reason that this issue is particularly worthy of investigation in the present context is that, as outlined above, 90% of the scientific effort (measured in dollars) has already been carried out, and would be difficult to duplicate in the future if support for science drops dramatically. Hence, the conditions under which the “other 10%” can be completed in such

adverse circumstances should be considered.

The first-level answer to this question has already been given above: if ELTs are seriously delayed or canceled, one can use present-day telescopes and instruments to carry out the necessary observations, which can mostly be completed by 2050. This would be disappointing to me personally, but it would not raise any scientific questions that needed to be addressed in the current paper.

However, the same adverse circumstances that led to ELT cancellations might also lead to abandonment of current 8m-class telescopes, or at least to failure to maintain their AO capabilities, which are relatively expensive.

Hence, the real question is, at what point would the fruit of the original KMTNet investment be “lost”, so that the experiment would have to be repeated, which, as I have indicated, would be a daunting prospect.

The main “loss mechanism” would be if the lenses and sources separated sufficiently that they dissolved into the field, so that they could not be reliably identified relative to random field stars. For example, after a century, their typical separations would be about 600 mas, an area that in typical field contains a dozen or more faint dwarf stars. At first sight, it seems “simple” to identify the lens and source: they will be the only pair of stars whose relative proper motion points back to zero, within $\lesssim 1$ mas, at t_0 . Depending on the quality of instruments, such relative proper motions could be measured by a second epoch taken 10% later, e.g., a decade in this illustrative example.

However, in the great majority of cases, either the source or the host (or both) will have a binary companion, mostly undetected, which means that the instantaneous proper motion will not point exactly back to zero. In most cases, this effect will not be critically important after only a century. For example, for a host in a face-on orbit, the internal proper motion will induce an offset after time Δt ,

$$\Delta\theta_{\text{int}} = \mu_{\text{int}}\Delta t = 8.2 \text{ mas} \left(\frac{Q^3 M / (1 + Q)^2}{M_{\odot} / 36} \right)^{1/3} \left(\frac{P}{100 \text{ yr}} \right)^{-1/3} \left(\frac{D_L}{5 \text{ kpc}} \right)^{-1} \left(\frac{\Delta t}{100 \text{ yr}} \right), \quad (24)$$

where I have normalized to a $Q \equiv M_{\text{companion}}/M_{\text{host}} = 0.5$ companion of an $M_{\text{host}} = 0.5 M_{\odot}$ host star. Hence, in the fiducial case, the proper motion would still point back to “zero” within 10 mas, which would likely be quite adequate.

The fiducial parameters in Equation (24) give a good indication of the general scale of the problem. Naively, it would seem that 8 times shorter periods would increase $\Delta\theta_{\text{int}}$ by a factor of 2. However, two measurements separated by the illustrative 10-year offset would differ by far less than would be inferred from the instantaneous internal velocity used in the

formula. The formula shows that the problem declines slowly with increasing period, so that quite a broad range of periods, for companions of either the host or the source, would cause problems of a similar scale.

However, for much larger wait times, e.g., $\Delta t \sim 1000$ yr, the problems of identifying the sources and lenses would become more challenging. Thus, I conclude that late-time AO could be comfortably delayed by up to a century or so.

At that point, the sources and hosts would have separated sufficiently that 3m-class AO would be adequate to carry out the observations. This reduced requirement could be important if the resources available to astronomy were still strapped.

Another issue related to such a possible long hiatus of astronomical work is data archiving. While we have no difficulty reading Mayan or Sumerian tablets, or even parchment and papyrus texts of the *Dead Sea Scrolls*, it is already challenging to read magnetic tapes of the 1980s. Up until a few years ago, astronomy papers were routinely archived in paper form. However, according to my understanding, this is no longer the case. While the general problems of scientific archiving are well beyond the scope of this paper, I suggest that it would be prudent to at least print out and carefully store all microlensing planet-discovery papers, i.e., match the prudence of the archivists of the *Scrolls*.

I thank S. Dong, J. Kollmeier, M. Pinsonneault, Y. Shvartzvald, and J.C. Yee for valuable discussions.

REFERENCES

- Alcock, C., Alssman, R.A., Alves, D.R., et al. 2001, *Nature*, 414, 617
- Bachelet, E., Shin, I.-G., Han, C., et al. 2012, *ApJ*, 754, 75
- Baraffe, I., Homeier, D., Allard, F., & Chabrier, G. 2015, *A&A*, 577, A42
- Batista, V., Dong, S., Gould, A., et al. 2005, *ApJ*, 508, 467
- Batista, V., Gould, A., Dieters, S. et al. 2011, *A&A*, 529, 102
- Batista, V., Beaulieu, J.-P., Gould, A., et al. 2014 *ApJ*, 780, 54
- Batista, V., Beaulieu, J.-P., Bennett, D.P., et al. 2015, *ApJ*, 808, 170
- Beaulieu, Batista, V., J.-P. Bennett, D.P., et al. 2018, *AJ*, 155, 78

- Benedict, G.F., Henry, T.J., Franz, O.G., et al. 2016, *AJ*, 152, 141
- Bennett, D.P., Anderson, J., Bond, I.A., Udalski, A., & Gould, A. 2006, *ApJ*, 647, L171
- Bennett, D.P., Bond, I.A., Udalski, A., et al. 2008, *ApJ*, 684, 663
- Bennett, D.P., Rhie, S.H., Nikolaev, S. et al. 2010, *ApJ*, 713, 837
- Bennett, D.P., Batista, V., Bond, I.A., et al. 2014, *ApJ*, 785, 155
- Bennett, D.P., Bhattacharya, A., Anderson, J., et al. 2015, *ApJ*, 808, 169
- Bennett, D.P., Rhie, S.H., Udalski, A., et al. 2016, *AJ*, 152, 125
- Bennett, D.P., Udalski, A., Han, C., et al. 2018a, *AJ*, 155, 141
- Bennett, D.P., Udalski, A., Bond, I.A., et al. 2018b, *AJ*, 156, 113
- Bennett, D.P., Bhattacharya, A., Beaulieu, J.-P., et al. 2020, *AJ*, 159, 68
- Bessell, M.S., & Brett, J.M. 1988, *PASP*, 100, 1134
- Bhattacharya, A., Bennett, D.P., Anderson, J., et al. 2017, *AJ*, 154, 59
- Bhattacharya, A., Beaulieu, J.-P., Bennett, D.P., et al. 2018, *AJ*, 156, 289
- Bhattacharya, A., Bennett, D.P., Beaulieu, J.-P., et al. 2021, *AJ*, 162, 60
- Blackman, J.W., Bennett, D.P., Cole, A.A., et al. 2021, *AJ*, 162, 279
- Bond, I.A., Bennett, D.P., Sumi, T. et al. 2017, *MNRAS*, 469, 2434
- Calchi Novati, S., Skowron, J., Jung, Y.K., et al. 2018, *AJ*, 155, 261
- Calchi Novati, S., Suzuki, D., Udalski, A., et al. 2019, *AJ*, 157, 121
- Chung, S.-J., Yee, J.C., Udalski, A., 2022, *JKAS*, 55, 123
- Close, L. M., Males, J. R., Kopon, D. A., et al. 2012, *Proc. SPIE*, 8447, 84470X
- Dong, S., Gould, A., Udalski, A., et al. 2009a, *ApJ*, 695, 970
- Dong, S., Bond, I.A., Gould, A., et al. 2009b, *ApJ*, 698, 1826
- Dong, S., Mérand, A., Delplancke-Strobale, F. et al. 2019, *ApJ*, 871, 70
- Duquennoy, A., & Mayor, M. 1991, *A&A*, 248, 485

- Fukui, A., Gould, A., Sumi, T., et al. 2015, *ApJ*, 809, 74
- Furusawa, K., Udalski, A., Sumi, T., et al. 2013, *ApJ*, 779, 91
- Gaudi, B.S., Bennett, D.P., Udalski, A. et al. 2008, *Science*, 319, 927
- Ghosh, H., DePoy, D.L., Gal-Yam, A., et al. 2004, *ApJ*, 615, 450
- Gonzalez, O. A., Rejkuba, M., Localize, M., et al. 2012, *A&A*, 543, A13
- Gould, A. 1999, *ApJ*, 514, 869
- Gould, A. 2004, *ApJ*, 606, 319
- Gould, A. 2014, *JKAS*, 47, 153
- Gould, A. 2020, *JKAS*, 53, 99
- Gould, A., Miralda-Escudé, J. & Bahcall, J.N. 1994, *ApJ*, 423, L105
- Gould, A., Udalski, A., An, D. et al. 2006, *ApJ*, 644, L37
- Gould, A., Udalski, A., Monard, B. et al. 2009, *ApJ*, 698, L147
- Gould, A., Dong, S., Gaudi, B.S. et al. 2010, *ApJ*, 720, 1073
- Gould, A., Udalski, A., Shin, I.-G. et al. 2014, *Science*, 345, 46
- Gould, A. & Zhu, W. 2016, *JKAS*, 49, 93
- Gould, A., Ryu, Y.-H., Calchi Novati, S., et al. 2020, *JKAS*, 53, 9
- Gould, A., Zang, W., Mao, S., & Dong, S., 2021, *RAA*, 21, 133
- Gould, A., Han, C., Zang, W., et al. 2022, *A&A*, 664A, 13
- Gould, A., Jung, Y.K., Hwang, K.-H., et al. 2022, *JKAS*, in press, arXiv:2204.03269
- Han, C., Udalski, A., Gould, A. 2017a, *AJ*, 154, 133
- Han, C., Udalski, A., Gould, A. 2017b, *AJ*, 154, 223
- Han, C., Sumi, T., Udalski, A., et al. 2018a, *AJ*, 155, 211
- Han, C., Bond, I.A., Gould, A., et al. 2018b, *AJ*, 156, 226
- Han, C., Yee, J.C., Udalski, A., et al. 2019a, *AJ*, 158, 102

- Han, C., Bennett, D.P., Udalski, A., et al. 2019b, *AJ*, 158, 114
- Han, C., Shin, I.-G., Jung, Y. K., et al. 2020a, *A&A*, 641A, 105
- Han, C., Udalski, A., Kim, D., et al. 2020b, *A&A*, 642A, 110
- Han, C., Udalski, A., Gould, A., et al. 2020c, *AJ*, 159, 91
- Han, C., Kim, D., Jung, Y.K., et al. 2020c, *AJ*, 160, 17
- Han, C., Udalski, A., Lee, C.-U., et al. 2021a, *A&A*, 649A, 90
- Han, C., Udalski, A., Kim, D., et al. 2021b, *A&A*, 650A, 89
- Han, C., Albrow, M.D., Chung, S.-J., et al. 2021c, *A&A*, 652A, 145
- Han, C., Udalski, A., Kim, D., et al. 2021d, *A&A*, 655A, 21
- Han, C., Gould, A., Hirao, Y., et al. 2021e, *A&A*, 655A, 24
- Han, C., Udalski, A., Kim, D., et al. 2021f, *AJ*, 161, 270
- Han, C., Udalski, A., Lee, C.-U., et al. 2022a, *A&A*, 658A, 93
- Han, C., Bond, I.A., Yee, J.C., et al. 2022b, *A&A*, 658A, 94
- Han, C., Gould, A., Bond, I.A., et al. 2022c, *A&A*, 662A, 70
- Han, C., Gould, A., Doeon, K., et al. 2022d, *A&A*, 663A, 145
- Han, C., Doeon, K., Gould, A., et al. 2022e, *A&A*, 664A, 33
- Han, C., Doeon, K., Yang, H., et al. 2022f, *A&A*, 664A, 114
- Han, C., Lee, C.-U., Gould, A., et al. 2022g, *A&A*, submitted,
- Han, C., et al. 2022h, *A&A*, in prep
- Herrera-Martin, A., Albrow, A., Udalski, A., et al. 2020, *AJ*, 159, 134
- Hirao, Y., Bennett, D.P., Ryu, Y.-H., et al., 2020, *AJ*, 160, 74
- Holtzman, J.A., Watson, A.M., Baum, W.A., et al. 1998, *AJ*, 115, 1946
- Hwang, K.-H., Udalski, A., Shvartzvald, Y. et al. 2018a, *AJ*, 155, 20
- Hwang, K.-H., Kim, H.-W., Kim, D.-J., et al. 2018b, *JKAS*, 51, 197

- Hwang, K.-H., Ryu, Y.-H., Kim, H.-W., et al. 2019, *AJ*, 157, 23
- Hwang, K.-H., Zang, W., Gould, A., et al., 2022, *AJ*, 163, 43
- Janczak, J., Fukui, A., Dong, S., et al. *ApJ*, 711, 731
- Jiang, G., DePoy, D.L., Gal-Yam, A., et al. 2004, *ApJ*, 617, 307
- Johnson, S.A., Penny, M.T., & Gaudi, B.S. 2022, *ApJ*, 927, 63
- Jung, Y. K., Gould, A., Udalski, A., et al. 2018, *AJ*, 155, 219
- Jung, Y. K., Gould, A., & Zang, W. et al. 2019a, *AJ*, 157, 72
- Jung, Y.K., Gould, A., Udalski, A., et al. 2019b, *AJ*, 158, 28
- Jung, Y.K., Gould, A., Udalski, A., et al. 2020a, *AJ*, 160, 148
- Jung, Y. K., Udalski, A., & Zang, W. et al. 2020b, *AJ*, 160, 255
- Jung, Y.K., Han, C., Udalski, A., et al. 2021, *AJ*, 161, 293
- Jung, Y. K., Zang, W., Han, C., et al. 2022, *AJ*, submitted, arXiv:2206.11409
- Kim, S.-L., Lee, C.-U., Park, B.-G., et al. 2016, *JKAS*, 49, 37
- Kim, D.-J., Kim, H.-W., Hwang, K.-H., et al., 2018a, *AJ*, 155, 76
- Kim, D.-J., Hwang, K.-H., Shvartzvald, et al. 2018b, arXiv:1806.07545
- Kim, Y.-H., Chung, S.-J., Udalski, A., et al. 2020, *JKAS*, 53, 161
- Kim, Y.H., Chung, S.-J., Yee, J.-C., et al. 2021a, *AJ*, 162, 17
- Kim, Y.-H., Chung, S.-J., Udalski, A., et al. 2021b, *MNRAS*, 503, 2706
- Kondo, I., Yee, J.C., Bennett, D.P., et al. 2021, *AJ*, 162, 77
- Koshimoto, N., Udalski, A., Sumi, T., et al. 2014, *AJ*, 788, 128
- Koshimoto, N., Udalski, A., Beaulieu, J.-P., et al. 2017a, *AJ*, 153, 1
- Koshimoto, N., Shvartzvald, Y., Bennett, D.P., et al., 2017b, *AJ*, 154, 3
- Males, J. R., Close, L. M., Morzinski, K. M., et al. 2014, *ApJ*, 786, 32
- Miyake, N., Sumi, T., Dong, S. et al. *ApJ*, 728, 120

- Miyazaki, S., Sumi, T., Bennett, D.P., et al. 2020, *AJ*, 159, 76
- Morzinski, K. M., Close, L. M., Males, J. R., et al. 2014, *Proc. SPIE*, 9148, 914804
- Mróz, P., Han, C., Udalski, A. et al. 2017a, *AJ*, 153, 143
- Mróz, P., Udalski, A. Bond, I.A., et al. 2017b, *AJ*, 154, 205
- Muraki, Y., Han, C., Bennett, D.P., et al. 2011, *ApJ*, 741, 22
- Nagakane, M., Sumi, T., Koshimoto, N. et al. 2017, *AJ*, 154, 35
- Nataf, D.M., Gould, A., Fouqué, P. et al. 2013, *ApJ*, 769, 88
- Penny, M.T., Gaudi, B.S., Kerins, E., et al. 2019, *AJ*, 241, 3
- Rattenbury, N.J., Bennett, D.P., Sumi, T., et al. 2017, *MNRAS*, 466, 2710
- Refsdal, S. 1964, *MNRAS*, 128, 295
- Ryu, Y.-H., Udalski, A., Yee, J.C. et al. 2017a, *AJ*, 154, 247
- Ryu, Y.-H., Yee, J.C., Udalski, A., et al. 2017b, *AJ*, 155, 40
- Ryu, Y.-H., Hwang, K.-H., Gould, A. et al. 2019a, *AJ*, 158, 151
- Ryu, Y.-H., Navarro, M.G., Gould, A. et al. 2019b, *AJ*, 159, 58
- Ryu, Y.-H., Udalski, A., Yee, J.C. et al. 2020, *AJ*, 160, 183
- Ryu, Y.-H., Hwang, K.-H., Gould, A. et al. 2021, *AJ*, 162, 96
- Ryu, Y.-H., Jung, Y.K., Yang, H., et al. 2022a, *AJ*, in press, arXiv:2202.03022
- Ryu, Y.-H., Shin, I.-G., Yang, H., et al. 2022b, *AAS*, submitted, arXiv:2207.07295
- Shin, I.-G., Ryu, Y.H, Yee, J.C., et al. 2019, *AJ*, 157, 146
- Shin, I.-G., Yee, J.C., Hwang, K.-H., et al. 2022a, *AJ*, 183, 254
- Shin, I.-G., Yee, J.C., Gould, A, et al. 2022b, *AJ*, submitted arXiv:2209.03886
- Shvartzvald, Y., Maoz, D., Kaspi, S. et al. 2014, *MNRAS*, 439, 604
- Shvartzvald, Y., Maoz, D., Udalski, A. et al. 2016, *MNRAS*, 457, 4089
- Shvartzvald, Y., Yee, J.C., Calchi Novati, S. et al. 2017, *ApJ*, 840, L3

- Skowron, J., Shin, I.-G., Udalski, A., et al. 2015, *ApJ*, 804, 33
- Skowron, J., Ryu, Y.-H., Hwang, K.-H., et al. 2016, *Acta Astron.*, 68, 43
- Smith, M., Mao, S., & Paczyński, B., 2003, *MNRAS*, 339, 925
- Sumi, T., Bennett, D.P., Bond, I.A., et al. 2010, *ApJ*, 710, 1641
- Suzuki, D., Udalski, A., Sumi, T., et al. 2014, *ApJ*, 780, 123
- Suzuki, D., Bennett, D.P., Sumi, T., et al. 2016, *ApJ*, 833, 145
- Szymański, M.K., Udalski, A., Soszyński, I., et al. 2011, *Acta Astron.*, 61, 83
- Terry, S.K., Bhattacharya, A., Bennett, D.P., et al. 2021, *AJ*, 161, 54
- Terry, S.K., Bennett, D.P., Bhattacharya, A., et al. 2022, arXiv:2206.03502
- Udalski, A., Yee, J.C., Gould, A., et al. 2015, *ApJ*, 799, 237
- Udalski, A., Ryu, Y.-H., Sajadian, S., et al. 2018, *Acta Astron.*, 68, 1
- Unwin, S.C., Shao, M., Tanner, A.M., et al. *PASP*, 120, 38
- Vandorou, A., Bennett, D.P., Beaulieu, J.-P., et al. 2020, *AJ*, 160, 121
- Wang, H., Zang, W., Zhu, W., et al. 2022, *MNRAS*, 510, 1778
- Xie, X.-J. 2021, Ph.D. Thesis, Peking University
- Xie, X.-J. Dong, S., Shvartzvald, Y., et al. 2021, *RAA*, 21, 303
- Yang, H., Zhang, X., Hwang, K.-H., et al. 2020, *AJ*, 159, 98
- Yang, H., Zang, W., Gould, A., et al. 2022, *MNRAS*, 516, 1894
- Yee, J.C., Udalski, A., Sumi, T. et al. 2009, *ApJ*, 703, 2082
- Yee, J.C., Shvartzvald, Y., Gal-Yam, A. et al. 2012, *ApJ*, 755, 102
- Yee, J.C., Gould, A., Beichman, C., 2015, *ApJ*, 810, 155
- Yee, J.C., Zang, W., Udalski, A. et al. 2021, *AJ*, 162, 180
- Yoo, J., DePoy, D.L., Gal-Yam, A. et al. 2004, *ApJ*, 603, 139
- Zang, W., Hwang, K.-H., Udalski, A., et al. 2021, *AJ*, 162, 163

Zang, W., Shvartzvald, Y., Udalski, A., et al. 2022a, MNRAS, 514, 5952

Zang, W., Yang, H., Han, c., et al. 2022b, MNRAS, 515, 928

Zang, W., Jung, Y.K., Yang, H., et al. 2023a, in prep

Zang, W., Jung, Y.K, et al. 2023b, in prep

Zhu, W., Penny, M., Mao, S., Gould, A., & Gendron, R. 2014, ApJ, 788, 73

Table 1. EVENTS WITH μ_{rel} MEASUREMENTS

| Name | t_0 | μ_{rel} | I_0 | $(V-I)_0$ | A_K | l/b | $\log t_E$ | $\log u_0$ | $\log \rho$ | $\log q$ | $v_{\oplus,\perp}$ | M_{cr} | codes | Reference |
|----------|-------|--------------------|-------|-----------|-------|-------|------------|------------|-------------|----------|--------------------|-----------------|-------|-----------------------------|
| MB16227 | 7518 | 4.9 | 18.54 | 0.78 | 0.12 | +3.30 | 1.23 | -1.08 | -2.52 | -2.03 | 1.7 | 0.08 | 11000 | Koshimoto et al. (2017b) |
| KB160622 | | 0.2 | | | | -3.24 | 0.00 | 0.00 | 0.01 | 0.01 | 21.4 | | | |
| MB16319 | 7553 | 4.5 | 17.49 | 0.77 | 0.20 | +0.35 | 0.93 | -0.57 | -2.00 | -2.41 | 0.1 | 0.02 | 11000 | Han et al. (2018b) |
| KB161816 | | 0.0 | | | | -2.17 | 0.01 | 0.02 | 0.00 | 0.01 | 29.1 | | | |
| OB160596 | 7487 | 5.1 | 18.55 | 0.83 | 0.41 | -1.01 | 1.91 | -1.95 | -3.22 | -1.93 | 3.5 | 0.92 | 01000 | Mróz et al. (2017a) |
| KB161677 | | 0.8 | | | | -2.03 | 0.01 | 0.01 | 0.06 | 0.01 | 10.0 | | | |
| OB160613 | 7494 | 5.6 | 20.81 | 0.85 | 0.27 | +1.99 | 1.87 | -1.68 | -3.66 | -2.49 | 2.1 | 1.04 | 14020 | Han et al. (2017b) |
| KB160017 | | 1.1 | | | | -1.74 | 0.01 | 0.02 | 0.04 | 0.03 | 12.9 | | | |
| OB160693 | 7498 | 1.5 | 19.99 | 1.35 | 0.34 | +5.55 | 2.20 | -1.49 | -3.02 | -1.21 | -0.4 | 1.47 | 13000 | Ryu et al. (2017a) |
| KB161248 | | 0.2 | | | | +2.22 | 0.05 | 0.08 | 0.07 | 0.07 | 15.1 | | | |
| OB161067 | 7564 | 2.1 | 17.92 | 0.74 | 0.11 | +4.66 | 1.42 | -0.33 | -2.26 | -2.84 | 0.6 | 0.11 | 11001 | Calchi Novati et al. (2019) |
| KB161453 | | 0.0 | | | | -4.25 | 0.02 | 0.03 | 0.00 | 0.02 | 29.3 | | | |
| OB161093 | 7560 | 1.8 | 18.55 | 0.84 | 0.21 | -2.11 | 1.75 | -1.68 | -2.73 | -2.84 | -0.2 | 0.43 | 11001 | Shin et al. (2022a) |
| KB161345 | | 0.3 | | | | -3.85 | 0.01 | 0.02 | 0.07 | 0.03 | 29.3 | | | |
| OB161190 | 7582 | 1.9 | 19.35 | 0.77 | 0.29 | +2.63 | 1.98 | -1.76 | -3.04 | -1.85 | -0.8 | 1.23 | 11001 | Ryu et al. (2017b) |
| KB160113 | | 0.2 | | | | -1.84 | 0.00 | 0.01 | 0.02 | 0.01 | 27.3 | | | |
| OB161195 | 7569 | 9.2 | 17.83 | 0.69 | 0.24 | 0.00 | 1.00 | -1.28 | -2.49 | -4.32 | -0.8 | 0.07 | 11001 | Bond et al. (2017) |
| KB160372 | | 0.8 | | | | -2.47 | 0.00 | 0.01 | 0.03 | 0.05 | 28.9 | | | Shvartzvald et al. (2017) |
| OB161227 | 7562 | 0.8 | 14.07 | 1.38 | 0.40 | -4.47 | 1.66 | -1.18 | -1.04 | -2.10 | -1.4 | 0.13 | 11200 | Han et al. (2020c) |
| KB161089 | | 0.1 | | | | -1.94 | 0.08 | 0.08 | 0.08 | 0.16 | 29.2 | | | |
| KB160212 | 7463 | 8.1 | 19.09 | 0.77 | 0.27 | +0.79 | 1.42 | -0.48 | -2.92 | -1.43 | 3.0 | 0.05 | 13800 | Hwang et al. (2018b) |
| | | 2.5 | | | | -1.60 | 0.01 | 0.02 | 0.08 | 0.07 | -2.2 | | | |
| KB161107 | 7509 | 2.6 | 14.14 | 1.38 | 0.37 | +2.49 | 1.31 | -0.03 | -1.23 | -1.44 | 0.5 | 0.06 | 14000 | Hwang et al. (2019) |

Table 1—Continued

| Name | t_0 | μ_{rel} | I_0 | $(V-I)_0$ | A_K | l/b | $\log t_E$ | $\log u_0$ | $\log \rho$ | $\log q$ | $v_{\oplus, \perp}$ | M_{cr} | codes | Reference |
|----------|-------|--------------------|-------|-----------|-------|-------|------------|------------|-------------|----------|---------------------|-----------------|-------|-----------------------------|
| | | 0.4 | | | | +1.50 | 0.02 | 0.03 | 0.05 | 0.07 | 20.9 | | | |
| KB162364 | 7601 | 3.2 | 19.26 | 0.91 | 0.52 | +0.96 | 1.31 | -1.55 | -2.52 | -2.12 | -2.0 | 0.08 | 01000 | Han et al. (2020b) |
| | | 0.0 | | | | +1.30 | 0.02 | 0.03 | 0.00 | 0.04 | 21.8 | | | |
| KB162605 | 7566 | 12.3 | 17.57 | 1.00 | 0.39 | +3.22 | 0.53 | -1.31 | -1.92 | -1.92 | 1.6 | 0.01 | 12000 | Ryu et al. (2021) |
| | | 1.0 | | | | -1.60 | 0.02 | 0.04 | 0.03 | 0.04 | 13.8 | | | |
| OB170173 | 7838 | 6.5 | 14.98 | 1.19 | 0.43 | +0.41 | 1.48 | -0.06 | -2.00 | -4.61 | 3.0 | 0.07 | 14800 | Hwang et al. (2018a) |
| KB171707 | | 0.4 | | | | -1.35 | 0.01 | 0.02 | 0.02 | 0.04 | 3.0 | | | |
| OB170373 | 7841 | 8.8 | 17.97 | 0.76 | 0.22 | -1.31 | 1.08 | -0.38 | -2.53 | -2.81 | 4.4 | 0.02 | 13800 | Skowron et al. (2018) |
| KB171529 | | 1.0 | | | | -3.71 | 0.01 | 0.01 | 0.03 | 0.10 | 3.7 | | | ⊙ |
| OB170406 | 7909 | 5.8 | 15.69 | 1.02 | 0.25 | +0.36 | 1.57 | -2.03 | -2.23 | -3.16 | 0.7 | 0.59 | 11001 | Hirao et al. (2020) |
| KB170243 | | 0.1 | | | | -2.42 | 0.00 | 0.00 | 0.00 | 0.01 | 28.2 | | | |
| OB171049 | 7907 | 6.7 | 17.14 | 0.75 | 0.45 | +2.95 | 1.46 | -0.74 | -2.62 | -2.02 | 0.5 | 0.40 | 01000 | Kim et al. (2020) |
| KB170370 | | 1.4 | | | | -1.46 | 0.00 | 0.00 | 0.01 | 0.02 | 27.8 | | | |
| OB171099 | 7917 | 5.9 | 19.91 | 1.03 | 0.44 | -1.68 | 1.28 | -2.40 | -2.81 | -2.19 | -1.1 | 0.16 | 01000 | Han et al. (2021d) |
| KB172336 | | 2.5 | | | | +1.46 | 0.04 | 0.11 | 0.05 | 0.05 | 29.3 | | | |
| OB171140 | 7941 | 4.1 | 15.09 | 1.02 | 0.36 | +4.00 | 1.17 | -0.62 | -1.57 | -2.14 | -0.8 | 0.07 | 11001 | Calchi Novati et al. (2018) |
| KB171018 | | 0.6 | | | | -1.93 | 0.00 | 0.01 | 0.04 | 0.04 | 28.0 | | | |
| OB171375 | 7970 | 3.6 | 19.80 | 0.70 | 0.29 | +0.04 | 2.01 | -1.55 | -1.44 | -1.83 | -2.5 | 2.10 | 01000 | Han et al. (2020b) |
| KB170078 | | 0.5 | | | | -2.76 | 0.02 | 0.03 | 0.04 | 0.02 | 21.4 | | | |
| OB171434 | 7985 | 8.1 | 18.45 | 0.73 | 0.23 | -0.28 | 1.80 | -1.37 | -3.33 | -4.24 | -3.2 | 1.30 | 11000 | Udalski et al. (2018) |
| KB170016 | | 0.5 | | | | -2.07 | 0.01 | 0.01 | 0.01 | 0.01 | 15.2 | | | |
| OB171522 | 7972 | 3.2 | 20.61 | 1.15 | 0.20 | +2.51 | 0.88 | -1.27 | -2.22 | -1.80 | -1.8 | 0.01 | 01000 | Jung et al. (2018) |
| KB170460 | | 0.5 | | | | -2.18 | 0.02 | 0.03 | 0.05 | 0.04 | 21.1 | | | |

Table 1—Continued

| Name | t_0 | μ_{rel} | I_0 | $(V-I)_0$ | A_K | l/b | $\log t_E$ | $\log u_0$ | $\log \rho$ | $\log q$ | $v_{\oplus, \perp}$ | M_{cr} | codes | Reference |
|----------|-------|--------------------|-------|-----------|-------|-------|------------|------------|-------------|----------|---------------------|-----------------|-------|---------------------|
| OB171691 | 8003 | 5.7 | 17.40 | 0.71 | 0.43 | -1.60 | 1.28 | -1.31 | -2.45 | -4.01 | -3.3 | 0.03 | 12300 | Han et al. (2022e) |
| KB170752 | | 1.0 | | | | +1.90 | 0.02 | 0.02 | 0.06 | 0.15 | 5.0 | | | |
| OB171806 | 8024 | 1.7 | 18.98 | 0.83 | 0.30 | +4.09 | 1.82 | -1.59 | -2.74 | -4.35 | -0.4 | 0.09 | 01200 | Zang et al. (2023a) |
| KB171021 | | 0.6 | | | | +2.66 | 0.03 | 0.03 | 0.15 | 0.17 | 4.6 | | | |
| KB170165 | 7854 | 6.9 | 19.25 | 1.01 | 0.32 | +2.14 | 1.62 | -1.46 | -3.11 | -2.87 | 2.3 | 0.32 | 11000 | Jung et al. (2019a) |
| | | 1.1 | | | | -2.04 | 0.01 | 0.01 | 0.06 | 0.03 | 10.1 | | | |
| KB170673 | 7973 | 15.7 | 14.15 | 1.10 | 0.45 | -4.88 | 1.35 | -0.92 | -2.12 | -2.25 | -4.8 | 0.39 | 01000 | Han et al. (2022g) |
| | | 5.1 | | | | -1.73 | 0.01 | 0.02 | 0.13 | 0.10 | 18.6 | | | |
| KB171003 | 7873 | 2.6 | 17.60 | 0.67 | 0.24 | +3.42 | 1.41 | -0.75 | -2.28 | -4.37 | -0.2 | 0.09 | 11200 | Zang et al. (2023a) |
| | | 0.6 | | | | +3.15 | 0.01 | 0.01 | 0.10 | 0.14 | 19.8 | | | |
| KB171038 | 7993 | 2.1 | 19.00 | 0.79 | 0.35 | +3.13 | 1.34 | -0.76 | -2.40 | -2.28 | -1.1 | 0.03 | 11000 | Shin et al. (2019) |
| | | 0.0 | | | | +2.06 | 0.01 | 0.01 | 0.00 | 0.02 | 10.9 | | | |
| KB171194 | 7943 | 1.3 | 19.29 | 0.71 | 0.14 | +6.63 | 1.67 | -0.59 | -2.59 | -4.58 | 0.6 | 0.21 | 11000 | Zang et al. (2023a) |
| | | 0.0 | | | | -4.34 | 0.02 | 0.03 | 0.00 | 0.06 | 28.6 | | | |
| KB172509 | 7872 | 1.3 | 20.18 | 1.14 | 0.44 | +1.85 | 1.83 | -1.18 | -2.72 | -2.36 | 0.5 | 0.30 | 01000 | Han et al. (2021d) |
| | | 0.6 | | | | +1.99 | 0.03 | 0.05 | 0.07 | 0.05 | 19.7 | | | |
| OB180298 | 8189 | 4.8 | 16.72 | 0.77 | 0.57 | -1.63 | 1.51 | -1.67 | -2.45 | -3.71 | 2.1 | 0.04 | 01400 | Jung et al. (2022) |
| KB181354 | | 1.0 | | | | +1.16 | 0.01 | 0.04 | 0.09 | 0.10 | -2.7 | | | |
| OB180383 | 8199 | 3.1 | 16.56 | 1.15 | 0.27 | +1.19 | 1.05 | -1.15 | -1.62 | -3.67 | 2.8 | 0.00 | 01000 | Wang et al. (2022) |
| KB180900 | | 0.3 | | | | -1.61 | 0.01 | 0.01 | 0.04 | 0.07 | 0.6 | | | |
| OB180506 | 8224 | 6.5 | 15.10 | 1.18 | 0.58 | -2.01 | 1.38 | -1.06 | -1.92 | -4.09 | 3.7 | 0.13 | 11000 | Hwang et al. (2022) |
| KB180835 | | 0.0 | | | | -2.45 | 0.01 | 0.01 | 0.00 | 0.12 | 13.4 | | | |
| OB180532 | 8220 | 3.3 | 21.30 | 1.73 | 0.13 | +1.54 | 2.14 | -2.08 | -3.55 | -4.01 | 2.7 | 1.72 | 11300 | Ryu et al. (2020) |

Table 1—Continued

| Name | t_0 | μ_{rel} | I_0 | $(V-I)_0$ | A_K | l/b | $\log t_E$ | $\log u_0$ | $\log \rho$ | $\log q$ | $v_{\oplus, \perp}$ | M_{cr} | codes | Reference |
|----------|-------|--------------------|-------|-----------|-------|-------|------------|------------|-------------|----------|---------------------|-----------------|-------|------------------------------|
| KB181161 | | 0.2 | | | | -2.73 | 0.03 | 0.03 | 0.04 | 0.05 | 10.2 | | | |
| OB180567 | 8245 | 3.1 | 15.33 | 0.98 | 0.38 | +1.99 | 1.39 | -0.13 | -1.75 | -2.91 | 1.5 | 0.10 | 01000 | Jung et al. (2021) |
| KB180890 | | 0.5 | | | | -1.49 | 0.02 | 0.02 | 0.02 | 0.02 | 21.1 | | | |
| OB180596 | 8277 | 4.1 | 15.30 | 1.14 | 0.29 | +0.96 | 1.46 | -0.55 | -1.87 | -3.74 | 0.5 | 0.25 | 11301 | Jung et al. (2019b) |
| KB180945 | | 0.4 | | | | -2.13 | 0.00 | 0.01 | 0.02 | 0.03 | 28.6 | | | |
| OB180677 | 8230 | 3.4 | 17.73 | 0.59 | 0.22 | -1.61 | 0.69 | -0.99 | -1.31 | -4.05 | 3.2 | 0.00 | 15000 | Herrera-Martin et al. (2020) |
| KB180816 | | 0.0 | | | | -3.31 | 0.01 | 0.01 | 0.00 | 0.19 | 15.3 | | | |
| OB180740 | 8254 | 7.7 | 21.53 | 0.87 | 0.11 | +1.74 | 1.77 | -1.40 | -3.65 | -2.34 | 2.4 | 1.61 | 11200 | Han et al. (2019a) |
| KB181822 | | 0.9 | | | | -4.80 | 0.03 | 0.03 | 0.05 | 0.04 | 23.2 | | | ⊕ |
| OB180799 | 8295 | 1.8 | 15.90 | 1.00 | 0.20 | +6.12 | 1.44 | -0.38 | -1.71 | -2.58 | 0.7 | 0.10 | 11001 | Zang et al. (2022a) |
| KB181741 | | 0.2 | | | | -3.73 | 0.01 | 0.01 | 0.05 | 0.03 | 29.3 | | | |
| OB180932 | 8301 | 6.2 | 14.75 | 1.05 | 0.29 | +0.81 | 1.43 | -0.07 | -1.93 | -2.92 | -0.9 | 0.33 | 11001 | Gould et al. (2022) |
| KB182087 | | 0.4 | | | | -1.50 | 0.00 | 0.00 | 0.01 | 0.03 | 28.7 | | | |
| OB180962 | 8263 | 5.6 | 19.37 | 0.87 | 0.28 | -2.11 | 1.46 | -0.68 | -2.94 | -2.62 | 1.7 | 0.32 | 01000 | Jung et al. (2021) |
| KB182071 | | 0.9 | | | | -3.04 | 0.00 | 0.07 | 0.02 | 0.01 | 26.4 | | | |
| OB180977 | 8277 | 11.5 | 18.55 | 0.66 | 0.24 | -0.49 | 1.31 | -0.83 | -2.72 | -4.38 | 0.5 | 0.36 | 11000 | Hwang et al. (2022) |
| KB180728 | | 2.4 | | | | -2.42 | 0.02 | 0.03 | 0.09 | 0.04 | 28.6 | | | |
| OB181011 | 8285 | 2.8 | 17.33 | 0.77 | 0.27 | +1.04 | 1.09 | -1.28 | -1.92 | -2.01 | 0.1 | 0.03 | 01010 | Han et al. (2019b) |
| KB182122 | | 0.2 | | | | -2.04 | 0.01 | 0.01 | 0.06 | 0.01 | 29.2 | | | |
| OB181011 | 8285 | 2.8 | 17.33 | 0.77 | 0.27 | +1.04 | 1.09 | -1.28 | -1.92 | -1.82 | 0.1 | 0.03 | 01010 | Han et al. (2019b) |
| KB182122 | | 0.2 | | | | -2.04 | 0.01 | 0.01 | 0.06 | 0.02 | 29.2 | | | |
| OB181185 | 8311 | 4.8 | 18.12 | 0.68 | 0.28 | +2.47 | 1.20 | -2.16 | -2.46 | -4.16 | -0.8 | 0.09 | 11001 | Kondo et al. (2021) |
| KB181024 | | 0.4 | | | | -2.00 | 0.00 | 0.00 | 0.01 | 0.01 | 27.7 | | | |

Table 1—Continued

| Name | t_0 | μ_{rel} | I_0 | $(V-I)_0$ | A_K | l/b | $\log t_E$ | $\log u_0$ | $\log \rho$ | $\log q$ | $v_{\oplus,\perp}$ | M_{cr} | codes | Reference |
|----------|-------|--------------------|-------|-----------|-------|-------|------------|------------|-------------|----------|--------------------|-----------------|-------|---------------------|
| OB181269 | 8344 | 8.3 | 17.44 | 0.64 | 0.26 | +2.61 | 1.85 | -0.84 | -3.23 | -3.24 | -1.7 | 1.98 | 11000 | Jung et al. (2020a) |
| KB182418 | | 0.6 | | | | -1.82 | 0.01 | 0.08 | 0.01 | 0.02 | 18.3 | | | |
| OB181428 | 8340 | 5.6 | 15.76 | 0.87 | 0.44 | +1.99 | 1.38 | -0.15 | -2.14 | -2.77 | -1.7 | 0.16 | 01000 | Kim et al. (2021b) |
| KB180423 | | 0.4 | | | | +2.11 | 0.03 | 0.00 | 0.01 | 0.01 | 18.5 | | | |
| OB181647 | 8374 | 0.6 | 19.44 | 0.85 | 0.17 | -1.35 | 1.72 | -0.96 | -2.29 | -2.00 | -4.3 | 0.03 | 11000 | Gould et al. (2022) |
| KB182060 | | 0.1 | | | | -3.37 | 0.02 | 0.03 | 0.09 | 0.03 | 4.7 | | | |
| KB180029 | 8295 | 3.3 | 18.45 | 0.78 | 0.48 | -0.09 | 2.24 | -1.57 | -3.35 | -4.74 | -1.5 | 7.50 | 11001 | Gould et al. (2020) |
| | | 0.5 | | | | +1.95 | 0.04 | 0.05 | 0.07 | 0.05 | 29.0 | | | |
| KB180087 | 8282 | 7.0 | 13.96 | 1.37 | 0.43 | -0.03 | 0.66 | -0.28 | -0.96 | -2.68 | -1.0 | 0.01 | 11200 | Jung et al. (2022) |
| | | 0.0 | | | | +2.14 | 0.01 | 0.03 | 0.00 | 0.09 | 29.2 | | | |
| KB180247 | 8308 | 8.8 | 18.01 | 0.52 | 0.43 | +0.66 | 1.03 | -1.19 | -2.60 | -2.15 | -1.7 | 0.07 | 01000 | Jung et al. (2022) |
| | | 1.2 | | | | +2.33 | 0.02 | 0.02 | 0.05 | 0.03 | 27.2 | | | |
| KB180748 | 8372 | 9.2 | 17.27 | 0.79 | 0.39 | -0.81 | 0.64 | -1.47 | -1.96 | -2.69 | -3.8 | 0.00 | 11300 | Han et al. (2020a) |
| | | 0.8 | | | | -1.97 | 0.01 | 0.03 | 0.04 | 0.03 | 5.0 | | | |
| KB181025 | 8275 | 4.3 | 19.33 | 1.11 | 0.25 | +2.46 | 0.98 | -2.15 | -2.26 | -4.08 | 0.6 | 0.03 | 13500 | Han et al. (2021a) |
| | | 0.0 | | | | -2.08 | 0.01 | 0.01 | 0.00 | 0.14 | 28.2 | | | |
| KB181292 | 8407 | 10.8 | 13.99 | 1.81 | 0.74 | -5.23 | 1.76 | -0.54 | -2.13 | -2.45 | -3.9 | 1.42 | 11000 | Ryu et al. (2019b) |
| | | 1.9 | | | | -0.28 | 0.03 | 0.01 | 0.06 | 0.03 | -14.8 | | | |
| KB181743 | 8249 | 2.3 | 19.60 | 0.70 | 0.12 | +5.69 | 1.45 | -0.60 | -2.68 | -2.92 | 1.7 | 0.10 | 13830 | Han et al. (2021c) |
| | | 0.5 | | | | -4.79 | 0.02 | 0.89 | 0.08 | 0.08 | 20.9 | | | |
| KB181990 | 8230 | 7.1 | 16.79 | 0.60 | 0.35 | +6.77 | 1.66 | -1.37 | -2.86 | -2.45 | -0.7 | 0.61 | 01400 | Ryu et al. (2019a) |
| | | 0.9 | | | | +1.91 | 0.02 | 0.02 | 0.05 | 0.04 | 15.8 | | | |
| OB190299 | 8560 | 1.7 | 19.45 | 0.89 | 0.25 | +4.70 | 1.47 | -1.25 | -2.46 | -2.00 | 0.1 | 0.00 | 11000 | Han et al. (2021d) |

Table 1—Continued

| Name | t_0 | μ_{rel} | I_0 | $(V-I)_0$ | A_K | l/b | $\log t_E$ | $\log u_0$ | $\log \rho$ | $\log q$ | $v_{\oplus, \perp}$ | M_{cr} | codes | Reference |
|----------|-------|--------------------|-------|-----------|-------|-------|------------|------------|-------------|----------|---------------------|-----------------|-------|---------------------|
| KB192735 | | 0.0 | | | | +2.57 | 0.02 | 0.02 | 0.00 | 0.03 | −0.6 | | | |
| OB190362 | 8564 | 6.8 | 16.99 | 0.72 | 0.43 | +2.11 | 1.35 | −1.01 | −2.46 | −2.13 | 0.7 | 0.03 | 01000 | Chung et al. (2022) |
| KB190075 | | 1.3 | | | | +4.41 | 0.01 | 0.02 | 0.01 | 0.09 | 2.8 | | | |
| OB190468 | 8494 | 4.4 | 19.43 | 0.83 | 0.36 | +3.83 | 1.88 | −1.92 | −3.28 | −2.45 | 0.1 | 1.05 | 01010 | Han et al. (2022a) |
| KB192696 | | 0.6 | | | | +2.34 | 0.02 | 0.02 | 0.03 | 0.02 | 16.0 | | | |
| OB190468 | 8494 | 4.4 | 19.43 | 0.83 | 0.36 | +3.83 | 1.88 | −1.92 | −3.28 | −1.97 | 0.1 | 1.05 | 01010 | Han et al. (2022a) |
| KB192696 | | 0.6 | | | | +2.34 | 0.02 | 0.02 | 0.03 | 0.02 | 16.0 | | | |
| OB190960 | 8686 | 11.3 | 18.85 | 0.92 | 0.11 | +6.10 | 1.79 | −2.21 | −3.48 | −4.83 | 0.2 | 2.95 | 11201 | Yee et al. (2021) |
| KB191591 | | 0.8 | | | | −4.30 | 0.01 | 0.01 | 0.02 | 0.04 | 26.5 | | | ⋈ |
| OB191053 | 8691 | 3.9 | 17.61 | 0.70 | 0.22 | +3.06 | 1.54 | −0.46 | −2.68 | −4.91 | −1.1 | 0.30 | 01000 | Zang et al. (2021) |
| KB191504 | | 0.4 | | | | −2.05 | 0.01 | 0.01 | 0.05 | 0.05 | 24.6 | | | |
| KB190371 | 8592 | 7.7 | 17.62 | 0.64 | 0.30 | −1.37 | 0.81 | −0.85 | −2.19 | −1.10 | 3.5 | 0.01 | 15400 | Kim et al. (2021a) |
| | | 0.7 | | | | +2.81 | 0.01 | 0.01 | 0.01 | 0.01 | 14.4 | | | |
| KB190842 | 8626 | 8.0 | 20.03 | 1.01 | 0.21 | +0.11 | 1.64 | −2.18 | −3.37 | −4.39 | 1.3 | 1.02 | 11000 | Jung et al. (2020b) |
| | | 1.8 | | | | −2.02 | 0.01 | 0.01 | 0.10 | 0.13 | 25.9 | | | |
| KB191042 | 8637 | 10.8 | 19.99 | 1.03 | 0.20 | +3.02 | 1.05 | −1.11 | −2.89 | −3.20 | 0.8 | 0.10 | 01000 | Zang et al. (2022b) |
| | | 2.1 | | | | −2.46 | 0.01 | 0.02 | 0.07 | 0.04 | 27.7 | | | |
| KB191715 | 8697 | 7.6 | 19.62 | 0.79 | 0.15 | +1.90 | 1.64 | −1.25 | −3.36 | −2.40 | −1.7 | 0.86 | 11040 | Han et al. (2021f) |
| | | 0.6 | | | | −2.91 | 0.00 | 0.01 | 0.01 | 0.02 | 22.9 | | | |
| KB191953 | 8702 | 5.7 | 18.39 | 0.63 | 0.29 | +1.85 | 1.21 | −2.63 | −2.62 | −2.71 | −1.9 | 0.08 | 02400 | Han et al. (2020c) |
| | | 0.5 | | | | −1.67 | 0.01 | 0.05 | 0.01 | 0.21 | 20.8 | | | |
| KB210119 | 9306 | 2.1 | 18.92 | 0.77 | 0.05 | +2.57 | 1.73 | −1.10 | −2.74 | −2.03 | 3.4 | 0.08 | 11000 | Shin et al. (2022b) |
| | | 0.0 | | | | −6.16 | 0.01 | 0.02 | 0.00 | 0.03 | 3.6 | | | |

Table 1—Continued

| Name | t_0 | μ_{rel} | I_0 | $(V-I)_0$ | A_K | l/b | $\log t_E$ | $\log u_0$ | $\log \rho$ | $\log q$ | $v_{\oplus, \perp}$ | M_{cr} | codes | Reference |
|----------|-------|--------------------|-------|-----------|-------|-------|------------|------------|-------------|----------|---------------------|-----------------|-------|---------------------|
| KB210171 | 9326 | 7.6 | 17.32 | 0.87 | 0.21 | +0.27 | 1.62 | -2.25 | -2.83 | -4.32 | 2.9 | 0.54 | 11000 | Yang et al. (2022) |
| | | 1.1 | | | | -2.71 | 0.00 | 0.01 | 0.05 | 0.08 | 15.5 | | | |
| KB210192 | 9316 | 4.9 | 17.68 | 0.58 | 0.29 | -0.16 | 1.49 | -2.00 | -2.70 | -3.43 | 3.0 | 0.14 | 01000 | Shin et al. (2022b) |
| | | 0.6 | | | | -1.82 | 0.01 | 0.04 | 0.04 | 0.04 | 11.2 | | | |
| KB210240 | 9313 | 3.1 | 17.44 | 0.68 | 0.49 | -0.39 | 1.63 | -2.52 | -2.56 | -3.19 | 3.1 | 0.16 | 13010 | Han et al. (2022f) |
| | | 0.4 | | | | -1.43 | 0.02 | 0.03 | 0.05 | 0.07 | 10.2 | | | |
| KB210240 | 9313 | 3.1 | 17.44 | 0.68 | 0.49 | -0.39 | 1.63 | -2.52 | -2.56 | -2.74 | 3.1 | 0.16 | 13010 | Han et al. (2022f) |
| | | 0.4 | | | | -1.43 | 0.02 | 0.03 | 0.05 | 0.12 | 10.2 | | | |
| KB210712 | 9350 | 2.2 | 20.40 | 0.69 | 0.17 | -0.66 | 2.00 | -0.84 | -3.37 | -3.25 | 2.2 | 1.38 | 01000 | Ryu et al. (2022b) |
| | | 0.3 | | | | -3.29 | 0.01 | 0.01 | 0.06 | 0.08 | 24.1 | | | |
| KB210748 | 9345 | 2.9 | 19.19 | 0.51 | 0.22 | +5.44 | 1.60 | -0.39 | -2.82 | -2.92 | 1.2 | 0.26 | 11000 | Ryu et al. (2022a) |
| | | 1.1 | | | | -3.03 | 0.06 | 0.04 | 0.15 | 0.16 | 21.4 | | | |
| KB210909 | 9354 | 8.2 | 17.26 | 0.81 | 0.56 | +0.75 | 1.21 | -1.22 | -2.49 | -2.50 | 0.2 | 0.15 | 01000 | Ryu et al. (2022b) |
| | | 1.1 | | | | +1.27 | 0.02 | 0.03 | 0.04 | 0.06 | 26.0 | | | |
| KB210912 | 9417 | 3.8 | 17.33 | 1.19 | 0.24 | -1.14 | 1.83 | -0.21 | -2.57 | -4.98 | -2.2 | 1.16 | 13800 | Han et al. (2022b) |
| | | 1.0 | | | | -4.09 | 0.02 | 0.02 | 0.10 | 0.19 | 25.6 | | | |
| KB211077 | 9378 | 1.8 | 18.56 | 0.82 | 0.26 | -4.15 | 1.40 | -1.97 | -2.26 | -2.81 | -0.2 | 0.09 | 01010 | Han et al. (2022c) |
| | | 0.1 | | | | -2.61 | 0.01 | 0.02 | 0.03 | 0.03 | 29.2 | | | |
| KB211077 | 9378 | 1.8 | 18.56 | 0.82 | 0.26 | -4.15 | 1.40 | -1.97 | -2.26 | -2.76 | -0.2 | 0.09 | 01010 | Han et al. (2022c) |
| | | 0.1 | | | | -2.61 | 0.01 | 0.02 | 0.03 | 0.04 | 29.2 | | | |
| KB211253 | 9374 | 15.2 | 19.10 | 0.80 | 0.64 | +0.26 | 0.98 | -2.25 | -2.89 | -2.31 | 0.1 | 0.10 | 15000 | Ryu et al. (2022a) |
| | | 2.4 | | | | -1.08 | 0.04 | 0.04 | 0.05 | 0.05 | 28.8 | | | |
| KB211303 | 9385 | 6.1 | 19.81 | 0.85 | 0.14 | -0.03 | 1.40 | -1.66 | -3.02 | -3.19 | 0.6 | 0.29 | 01000 | Han et al. (2022e) |

Table 1—Continued

| Name | t_0 | μ_{rel} | I_0 | $(V-I)_0$ | A_K | l/b | $\log t_E$ | $\log u_0$ | $\log \rho$ | $\log q$ | $v_{\oplus,\perp}$ | M_{cr} | codes | Reference |
|----------|-------|--------------------|-------|-----------|-------|-------|------------|------------|-------------|----------|--------------------|-----------------|-------|---------------------|
| | | 0.7 | | | | −3.03 | 0.01 | 0.01 | 0.04 | 0.03 | 29.2 | | | |
| KB211391 | 9385 | 5.3 | 20.96 | 0.88 | 0.15 | +2.66 | 1.50 | −1.92 | −3.27 | −4.44 | 0.2 | 0.40 | 11300 | Ryu et al. (2022a) |
| | | 0.6 | | | | −2.80 | 0.02 | 0.04 | 0.03 | 0.03 | 29.3 | | | |
| KB211554 | 9395 | 7.3 | 18.65 | 0.87 | 0.42 | −1.89 | 0.71 | −1.29 | −2.15 | −2.83 | −1.1 | 0.01 | 11000 | Han et al. (2022e) |
| | | 1.5 | | | | −2.54 | 0.06 | 0.09 | 0.08 | 0.16 | 28.9 | | | |
| KB211689 | 9409 | 6.1 | 19.77 | 1.18 | 0.21 | +0.37 | 1.35 | −2.22 | −2.84 | −3.68 | −1.4 | 0.22 | 15000 | Yang et al. (2022) |
| | | 0.8 | | | | −2.99 | 0.02 | 0.02 | 0.02 | 0.08 | 27.2 | | | |
| KB211898 | 9422 | 5.1 | 17.59 | 0.75 | 0.51 | +1.00 | 1.35 | −1.80 | −2.51 | −2.84 | −1.9 | 0.15 | 11030 | Han et al. (2022d) |
| | | 0.5 | | | | +1.35 | 0.04 | 0.05 | 0.05 | 0.09 | 23.3 | | | 67 |
| KB212294 | 9453 | 8.7 | 19.42 | 0.88 | 0.17 | +1.91 | 0.85 | −2.22 | −2.52 | −3.25 | −2.4 | 0.02 | 15000 | Shin et al. (2022b) |
| | | 1.0 | | | | −2.60 | 0.02 | 0.07 | 0.14 | 0.03 | 13.1 | | | |

Note. — M_{cr} is in units of $0.075 M_{\odot}$. Boldface μ_{rel} indicates a lower limit, in which case M_{cr} is also a lower limit and ρ is an upper limit.

Table 2. EVENTS WITHOUT μ_{rel} MEASUREMENTS

| Name | t_0 | I_0 | $(V-I)_0$ | A_K | l/b | $\log t_E$ | $\log u_0$ | $\log q$ | $v_{\oplus,\perp}$ | codes | Reference |
|----------|-------|-------|-----------|-------|-------|------------|------------|----------|--------------------|-------|---------------------|
| OB160263 | 7470 | 15.82 | 0.99 | 0.00 | -0.95 | 1.21 | -0.24 | -1.51 | 4.4 | 15000 | Han et al. (2017a) |
| KB161515 | | | | -4.06 | 0.03 | 0.02 | 0.01 | 0.9 | | | |
| KB161836 | 7488 | 20.24 | 0.82 | 0.24 | -0.12 | 1.73 | -1.25 | -2.35 | 3.1 | 01000 | Yang et al. (2020) |
| | | | | -1.95 | 0.02 | 0.03 | 0.08 | 10.3 | | | |
| KB162397 | 7550 | 19.96 | 0.82 | 0.20 | +4.81 | 1.77 | -1.39 | -2.40 | -0.8 | 01000 | Han et al. (2020b) |
| | | | | +3.14 | 0.06 | 0.06 | 0.10 | 29.1 | | | |
| KB170428 | 7944 | 19.40 | 1.06 | 0.15 | +2.59 | 1.65 | -0.69 | -4.30 | -0.5 | 01000 | Zang et al. (2023a) |
| | | | | -3.55 | 0.01 | 0.02 | 0.07 | 28.1 | | | |
| OB170482 | 7874 | 18.02 | 0.37 | 0.28 | -0.20 | 1.60 | -1.29 | -3.87 | 2.7 | 01000 | Han et al. (2018a) |
| KB170084 | | | | -2.80 | 0.02 | 0.01 | 0.06 | 19.1 | | | |
| KB171146 | 7925 | 19.01 | 0.77 | 0.18 | -2.44 | 1.41 | -0.54 | -2.70 | -0.2 | 11000 | Shin et al. (2019) |
| | | | | -4.14 | 0.02 | 0.06 | 0.08 | 29.3 | | | |
| OB180516 | 8228 | 17.58 | 0.55 | 0.26 | -0.57 | 1.40 | -0.98 | -3.89 | 3.5 | 01000 | Hwang et al. (2022) |
| KB180808 | | | | -3.59 | 0.01 | 0.01 | 0.05 | 14.1 | | | |
| OB181119 | 8316 | 18.29 | 0.70 | 0.15 | -1.38 | 1.59 | -0.36 | -2.74 | -1.8 | 01000 | Jung et al. (2022) |
| KB181870 | | | | -4.43 | 0.04 | 0.05 | 0.11 | 26.8 | | | |
| OB181126 | 8298 | 19.48 | 0.79 | 0.26 | -1.53 | 1.72 | -2.08 | -4.13 | -0.9 | 04300 | Gould et al. (2022) |
| KB182064 | | | | -2.88 | 0.03 | 0.03 | 0.28 | 29.0 | | | |
| OB181212 | 8394 | 17.63 | 0.73 | 0.13 | +2.72 | 1.71 | -1.89 | -2.91 | -2.5 | 11000 | Gould et al. (2022) |
| KB182299 | | | | -3.17 | 0.00 | 0.00 | 0.02 | -4.6 | | | |
| OB181367 | 8358 | 18.03 | 0.69 | 0.14 | +1.29 | 1.36 | -1.59 | -2.48 | -2.7 | 01000 | Gould et al. (2022) |
| KB180914 | | | | -2.64 | 0.00 | 0.01 | 0.02 | 12.4 | | | |
| KB180030 | 8272 | 13.93 | 1.14 | 0.46 | -0.11 | 1.45 | -0.05 | -2.56 | -0.5 | 01000 | Jung et al. (2022) |

Table 2—Continued

| Name | t_0 | I_0 | $(V-I)_0$ | A_K | l/b | $\log t_E$ | $\log u_0$ | $\log q$ | $v_{\oplus,\perp}$ | codes | Reference |
|----------|-------|-------|-----------|-------|-------|------------|------------|----------|--------------------|-------|---------------------|
| | | | | +1.88 | 0.00 | 0.00 | 0.05 | 28.5 | | | |
| KB181976 | 8183 | 16.99 | 0.87 | 0.19 | -5.80 | 1.62 | -0.84 | -2.50 | 6.4 | 01000 | Han et al. (2021b) |
| | | | | -3.48 | 0.01 | 0.01 | 0.13 | -6.6 | | | |
| KB181996 | 8348 | 15.95 | 0.99 | 0.53 | +6.30 | 1.67 | -1.74 | -2.82 | 0.1 | 01000 | Han et al. (2021b) |
| | | | | +1.38 | 0.01 | 0.02 | 0.11 | 16.2 | | | |
| KB182004 | 8239 | 17.98 | 0.69 | 0.23 | -0.30 | 1.50 | -0.63 | -3.43 | 2.5 | 01000 | Gould et al. (2022) |
| | | | | -2.23 | 0.01 | 0.02 | 0.11 | 19.3 | | | |
| KB182602 | 8270 | 15.88 | 1.06 | 0.32 | +6.43 | 1.99 | -0.29 | -2.78 | -0.7 | 11000 | Jung et al. (2022) |
| | | | | +2.83 | 0.06 | 0.08 | 0.07 | 28.9 | | | |
| KB182718 | 8355 | 21.10 | 1.37 | 0.21 | -0.28 | 2.21 | -1.23 | -1.71 | -3.3 | 12000 | Gould et al. (2022) |
| | | | | -2.02 | 0.08 | 0.08 | 0.07 | 13.0 | | | |
| OB191492 | 8763 | 20.08 | 0.70 | 0.17 | +1.91 | 1.72 | -1.33 | -3.74 | -3.5 | 01000 | Hwang et al. (2022) |
| KB193004 | | | | -2.63 | 0.03 | 0.04 | 0.12 | -7.8 | | | |
| KB190253 | 8591 | 17.29 | 0.67 | 0.37 | +0.13 | 1.78 | -1.27 | -4.39 | 2.6 | 11000 | Hwang et al. (2022) |
| | | | | -1.43 | 0.07 | 0.03 | 0.08 | 13.8 | | | |
| KB190414 | 8611 | 18.28 | 0.70 | 0.41 | +7.18 | 1.85 | -2.36 | -2.23 | -0.7 | 14700 | Han et al. (2022g) |
| | | | | +1.71 | 0.05 | 0.05 | 0.26 | 21.6 | | | |
| KB190953 | 8638 | 16.68 | 0.55 | 0.27 | +1.54 | 1.31 | -0.83 | -4.38 | 0.7 | 01000 | Hwang et al. (2022) |
| | | | | -2.08 | 0.02 | 0.03 | 0.04 | 28.0 | | | |
| KB191367 | 8668 | 20.71 | 1.06 | 0.11 | +1.93 | 1.59 | -1.08 | -4.30 | 0.0 | 01000 | Zang et al. (2023a) |
| | | | | -4.99 | 0.04 | 0.05 | 0.12 | 28.9 | | | |
| KB191552 | 8715 | 18.30 | 0.63 | 0.28 | +2.61 | 2.04 | -0.67 | -2.33 | -1.8 | 01000 | Zang et al. (2022b) |
| | | | | -1.72 | 0.04 | 0.04 | 0.05 | 16.0 | | | |

Table 2—Continued

| Name | t_0 | I_0 | $(V-I)_0$ | A_K | l/b | $\log t_E$ | $\log u_0$ | $\log q$ | $v_{\oplus,\perp}$ | codes | Reference |
|----------|-------|-------|-----------|-------|-------|------------|------------|----------|--------------------|-------|---------------------|
| KB191806 | 8716 | 19.95 | 0.76 | 0.20 | +1.41 | 2.13 | -1.59 | -4.71 | -2.5 | 01000 | Zang et al. (2023a) |
| | | | | -3.35 | 0.03 | 0.03 | 0.12 | 16.1 | | | |
| KB192974 | 8753 | 18.00 | 0.74 | 0.50 | +0.33 | 1.44 | -0.78 | -3.20 | -3.1 | 01000 | Zang et al. (2022b) |
| | | | | -1.33 | 0.04 | 0.04 | 0.13 | -3.1 | | | |
| KB210320 | 9316 | 18.84 | 0.70 | 0.31 | +2.10 | 1.11 | -2.23 | -3.54 | 3.4 | 01000 | Han et al. (2022e) |
| | | | | -4.30 | 0.01 | 0.02 | 0.07 | 10.6 | | | |
| KB211105 | 9376 | 18.61 | 0.51 | 0.39 | +2.61 | 1.54 | -0.96 | -2.70 | -0.7 | 01000 | Ryu et al. (2022b) |
| | | | | +2.30 | 0.02 | 0.03 | 0.04 | 29.1 | | | |
| KB211372 | 9389 | 18.39 | 0.75 | 0.51 | -0.21 | 1.85 | -1.12 | -3.36 | -1.4 | 01000 | Ryu et al. (2022a) |
| | | | | +1.85 | 0.05 | 0.06 | 0.08 | 29.1 | | | |
| KB212478 | 9482 | 18.97 | 0.76 | 0.24 | +1.16 | 1.53 | -1.00 | -2.22 | -2.9 | 11000 | Ryu et al. (2022b) |
| | | | | -2.27 | 0.01 | 0.01 | 0.03 | -1.7 | | | |

Table 3. MEANING AND DISTRIBUTIONS OF 5 CODES

| Entry | Notes? | Stat. Sample? | $\log q$ Degen. | Multiplicity | Spitzer? |
|-------|----------|---------------|-----------------|----------------------|----------|
| 0 | No (51) | | < 0.1 (92) | 2L1S (103) | No (103) |
| 1 | Yes (64) | Likely (92) | | 3L1S (2 plan.) (8) | Yes (12) |
| 2 | | Maybe (4) | 0.1–0.15 (6) | 3L1S (bin+plan.) (1) | |
| 3 | | Needs AO (8) | 0.15–0.2 (6) | 2L2S (2) | |
| 4 | | Unlikely (5) | 0.2–0.25 (4) | 3L2S (bin+plan.) (1) | |
| 5 | | No (6) | 0.25–0.3 (1) | | |
| 6 | | | 0.3–0.35 (0) | | |
| 7 | | | 0.35–0.4 (1) | | |
| 8 | | | > 0.4 (5) | | |

Table 4. $\Delta\theta$ (2030) AND ΔK FOR MOA (2007-12) EVENTS

| Name | $\Delta\theta$ | ΔK | Reference |
|----------|----------------|------------|-------------------------|
| MB10477 | 209 | 0.0 | Bachelet et al. (2012) |
| OB08379 | 163 | −0.4 | Suzuki et al. (2014) |
| OB07368 | 78 | 1.9 | Sumi et al. (2010) |
| MB11262 | 215 | 4.8 | Bennett et al. (2014) |
| OB120563 | 58 | −0.9 | Fukui et al. (2015) |
| MB12505 | 77 | 3.7 | Nagakane et al. (2017) |
| MB09387 | 78 | 3.8 | Batista et al. (2011) |
| OB08355 | 67 | 3.2 | Koshimoto et al. (2014) |
| MB11291 | 39 | 3.3 | Bennett et al. (2018b) |

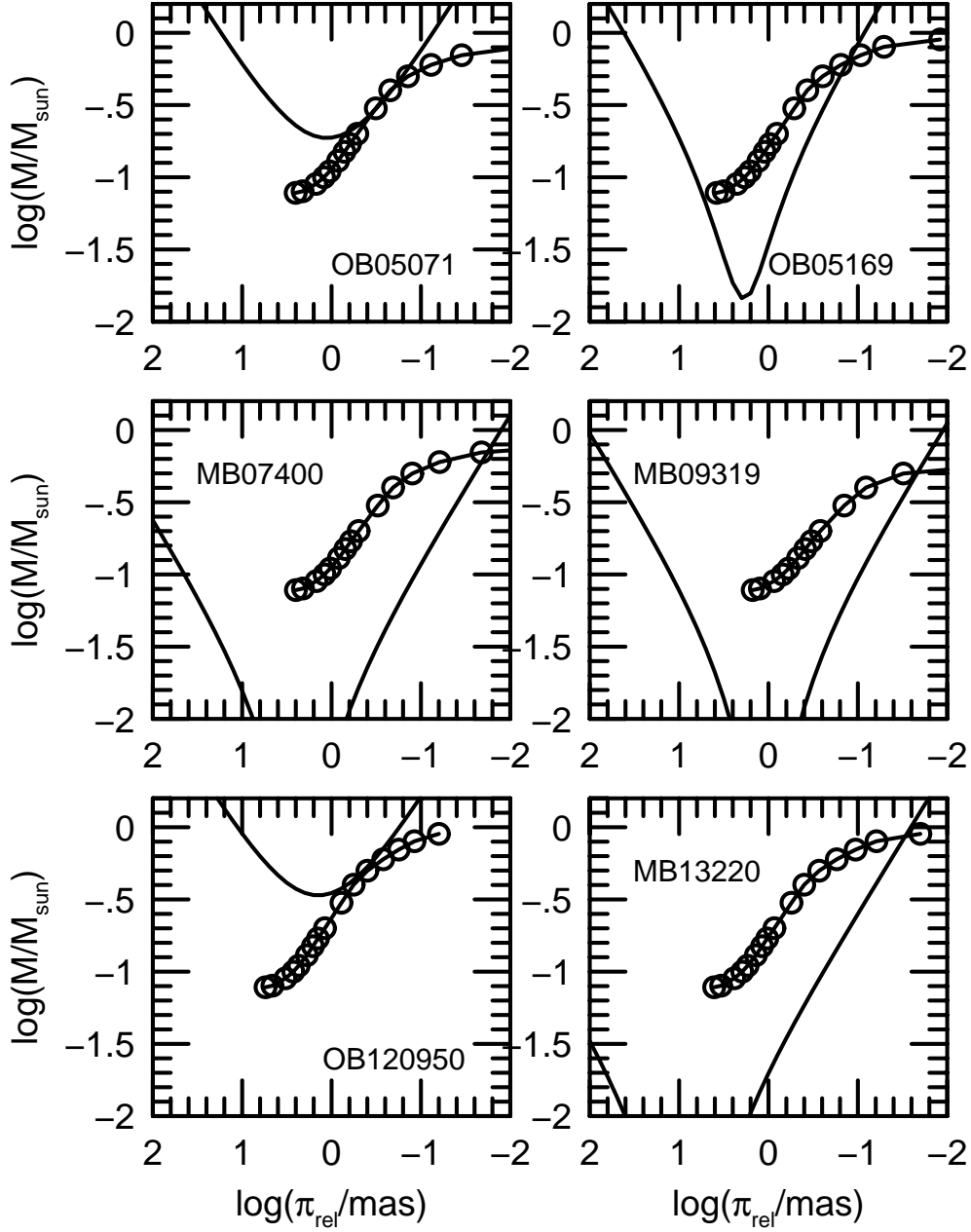


Fig. 1.— Equations (4) and (5) are illustrated for six planetary events (internal labels) for which the source and lens were separately resolved, enabling the measurements of K_{host} and $\mu_{\text{rel, hel}}$. Baraffe et al. (2015) K -band 1-Gyr isochrones are assumed. For OGLE-2005-BLG-169, I adopted $K_{\text{host}} = H_{\text{host}} - 0.11$. To the right, Equation (4) asymptotically approaches constant Einstein radius, i.e., $\theta_E \equiv \sqrt{\kappa M \pi_{\text{rel}}} \rightarrow \mu_{\text{rel, hel}} t_E$, while to the left, it asymptotically approaches constant microlens parallax, i.e., $\pi_E \equiv \pi_{\text{rel}}/\kappa M \rightarrow au/v_{\oplus, \perp} t_E$. For none of the six cases does Equation (5) cross both branches of Equation (4), but it comes close for OGLE-2005-BLG-169. The two curves are nearly tangent for two cases: OGLE-2005-BLG-071 and OGLE-2012-BLG-0950.

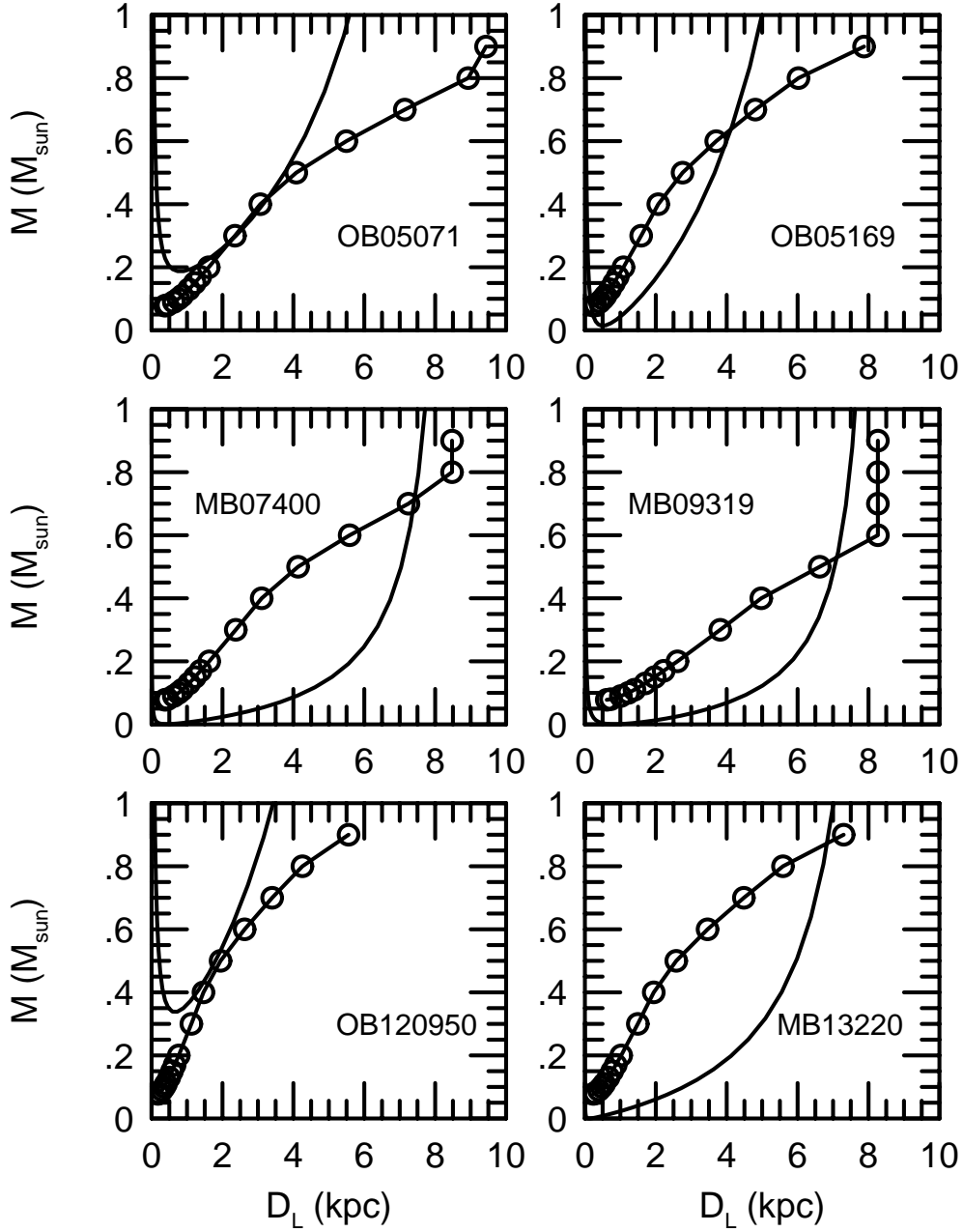


Fig. 2.— Alternate representations of the information in Figure 1, which is more similar to what is often displayed in the Keck AO papers. Note that the left (low-mass) branch of Equation (4) is clearly visible in this representation in only two of the six cases. It has not previously appeared in published diagrams.

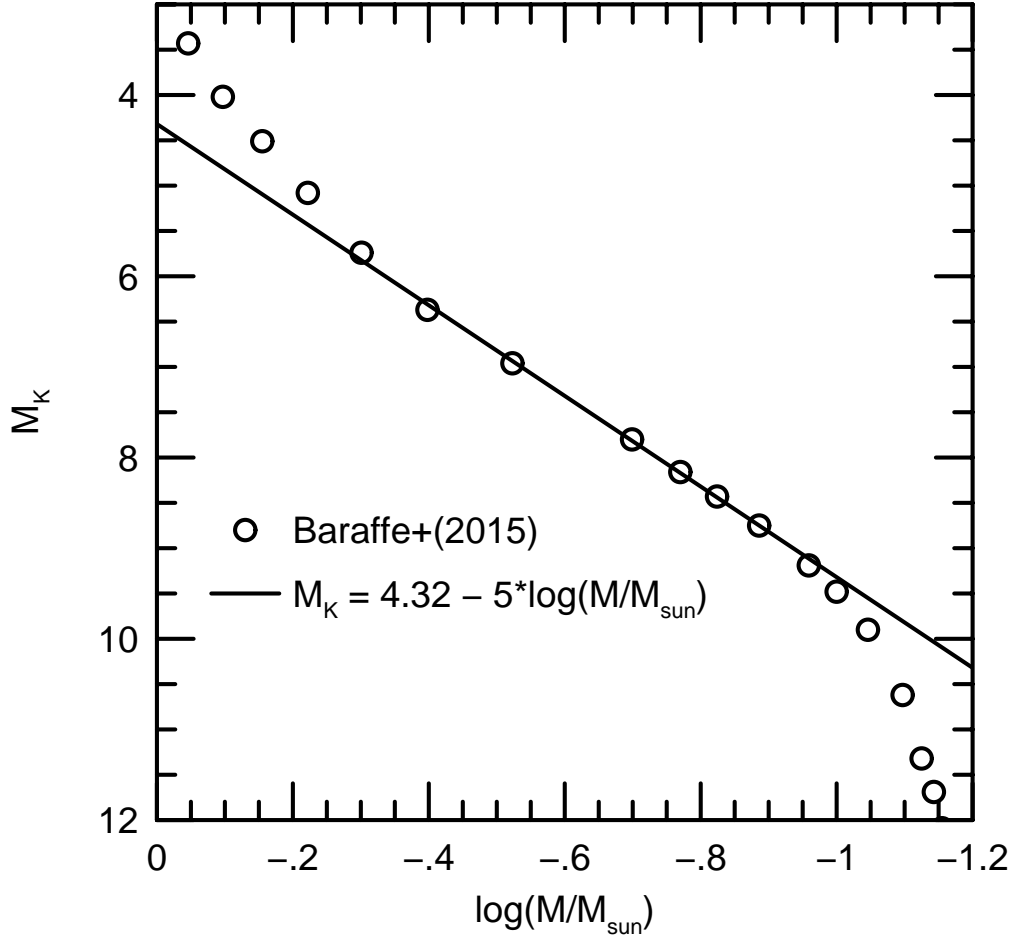


Fig. 3.— M_K versus $\log M$ mass-luminosity relation in the K band. The points show the 1-Gyr, solar-metallicity models of Baraffe et al. (2015). Over the mass range $-0.4 \gtrsim \log(M/M_\odot) \gtrsim -0.9$ (in which the star is fully convective and supported by the ideal gas law, $P = nkT$), these are well approximated by the solid line. This corresponds to a scaling $L_K \propto M^2$ of the K -band luminosity L_K . Hence, over this mass range, the function $H(M) \equiv -(5dM_K/d \log M + 1) \rightarrow 0$. See Figure 5.

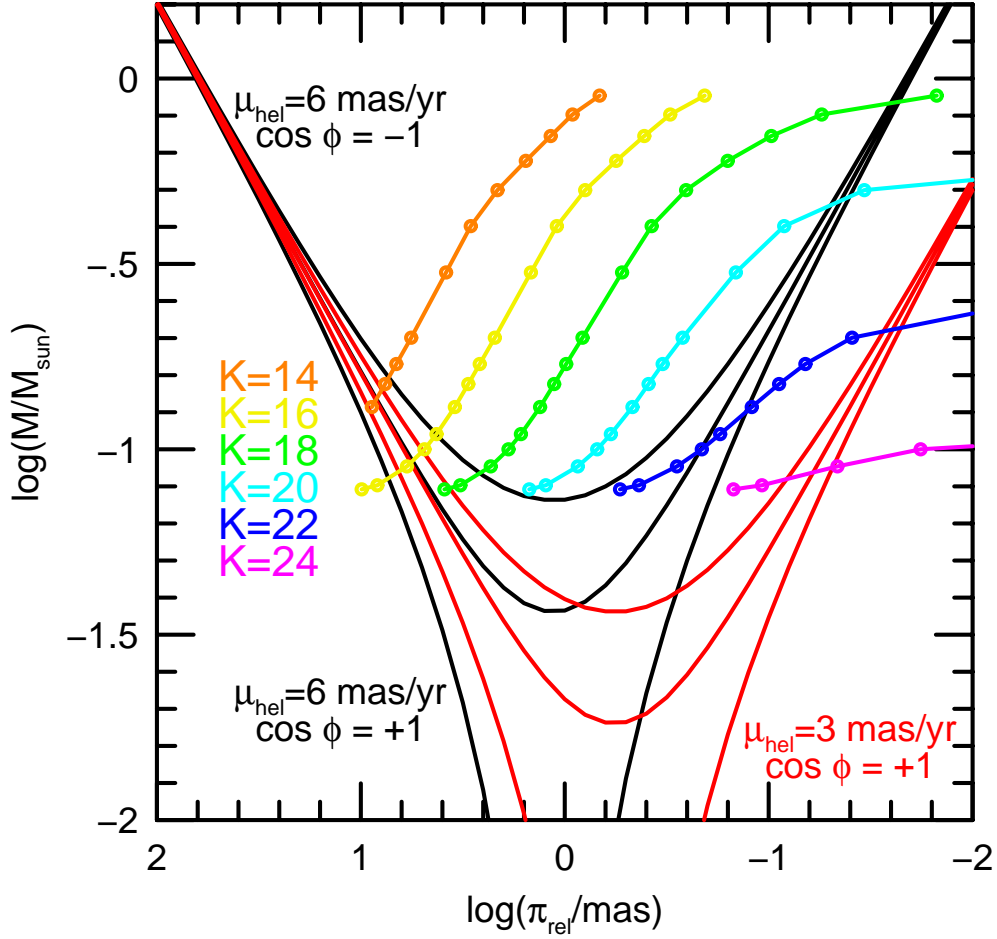


Fig. 4.— Illustration of the variation of Equations (4) and (5) with various input parameters. Several parameters are held fixed for all curves: $t_E = 25 \text{ day}$, $\pi_S = 0.115 \text{ mas}$, $A_K = 0.13$, $b = -3.0$, and $v_{\oplus, \perp} = 25 \text{ km s}^{-1}$. Equation (4) is illustrated for two values of μ_{relhel} , i.e., 3 (red) and 6 (black) mas yr^{-1} , and three values of $\cos \phi \equiv \boldsymbol{\mu}_{\text{relhel}} \cdot \mathbf{v}_{\oplus, \perp} / \mu_{\text{relhel}} v_{\oplus, \perp}$ i.e., -1 , 0 , and $+1$ (top to bottom). Equation (5) is illustrated for 6 values of $K_{\text{host}} = (14, 16, 18, 20, 22, 24)$ (top to bottom).

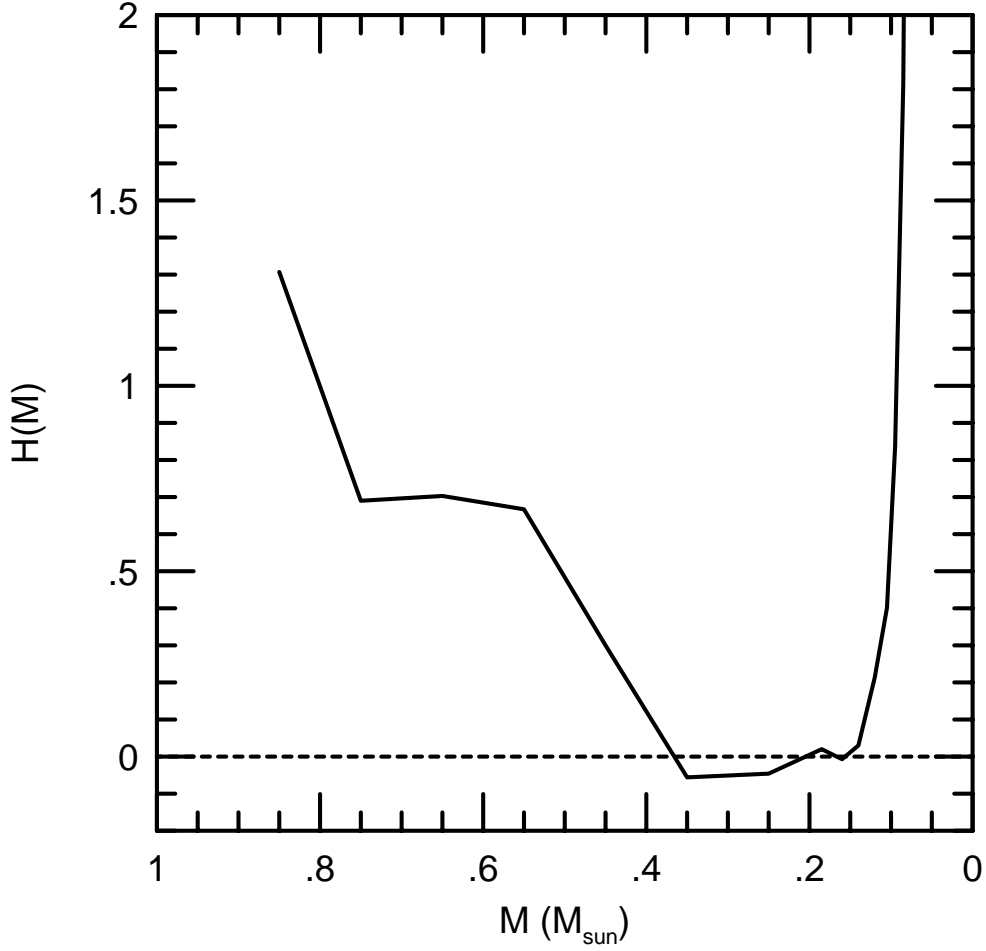


Fig. 5.— The function $H(M) = -(5dM_K/d\log M + 1)$, which plays a critical role in the error propagation. In particular, $H(M) = 0$ for the mass range $-0.4 \gtrsim \log(M/M_\odot) \gtrsim -0.9$, i.e., $0.4 \gtrsim (M/M_\odot) \gtrsim 0.13$. See, e.g., Equations (13), (16), and (18).

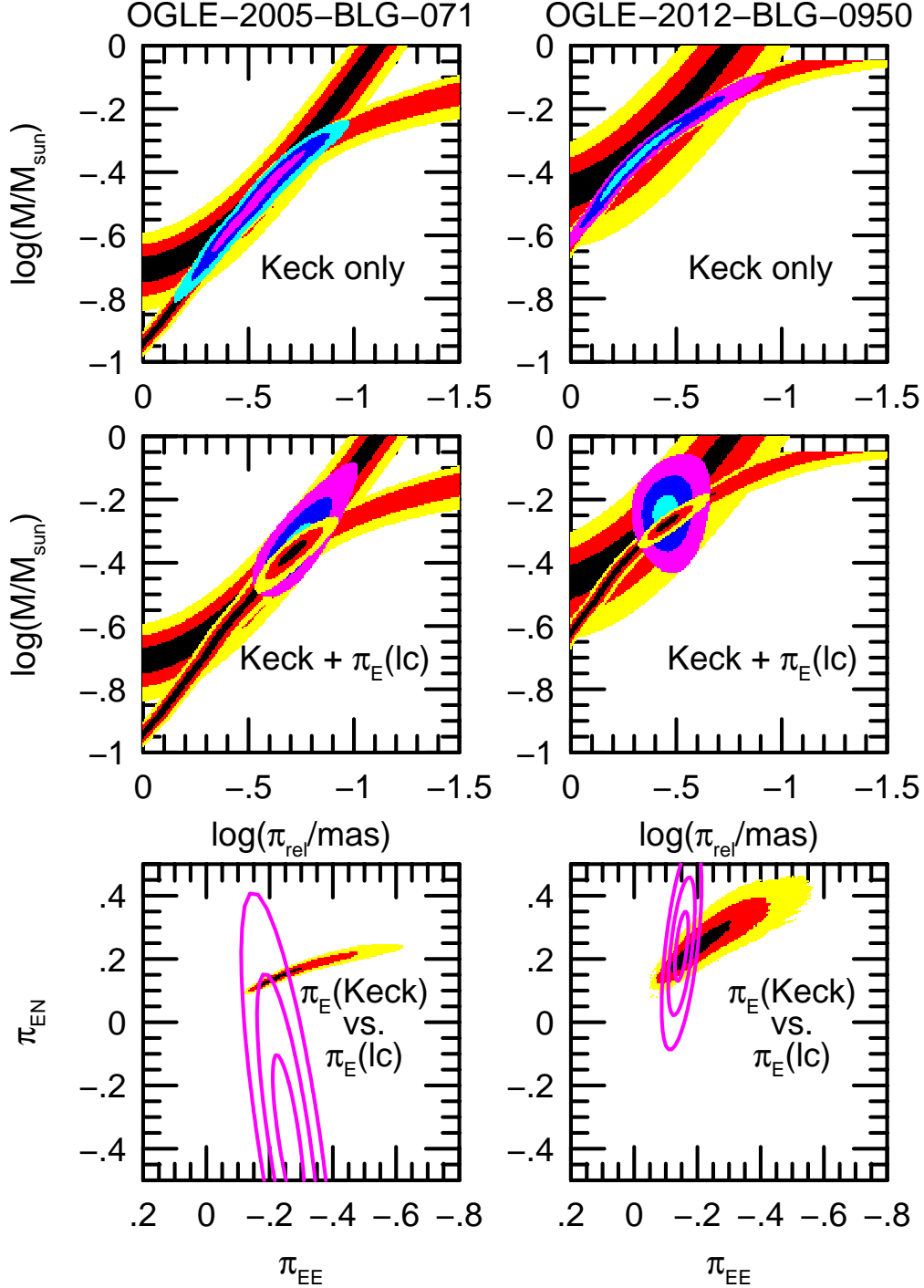


Fig. 6.— Two Keck AO mass measurements with continuous degeneracies that are broken by light-curve π_E measurements: OGLE-2005-BLG-071 (left) and OGLE-2012-BLG-0950 (right). Top row: Equations (4) and (5), i.e., “bottom” and “middle” contours, respectively, are combined to yield mass measurements (“top” contours) with 1σ ranges of $\Delta \log M = 0.4$ and 0.3 , respectively. Bottom row: Combined solution from top row is projected on the π_E plane (filled contours), where it can be compared to π_E contours derived from the light curve (open contours). In both cases, the two sets of contours are roughly orthogonal, so the combination is strongly constrained. Middle panel: “top” contours are the result of combining Equations (4) and (5), i.e., two “bottom” sets of contours, with the π_E constraint

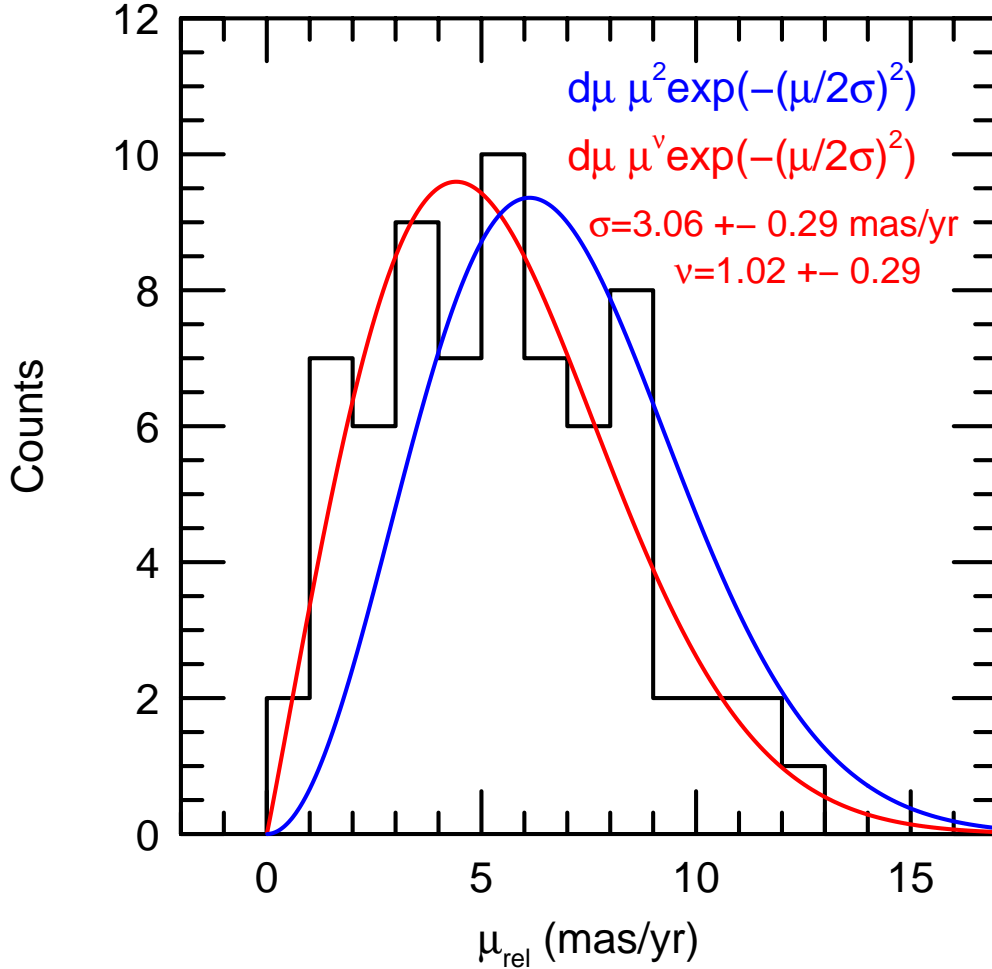


Fig. 7.— Distribution of observed μ_{rel} for 69 planetary events with proper-motion measurements with $\mu_{\text{rel}} < 15 \text{ mas yr}^{-1}$, together with two models of the form given by Equation (22). The blue model is an analytic representation of the distribution expected for microlensing events as a whole, while the red model is the best two-parameter fit of Equation (22) to the data. The red model is preferred by $\Delta\chi^2 = 15$, and it is plausibly explained by the fact that it is easier to detect planets in lower μ_{rel} events.

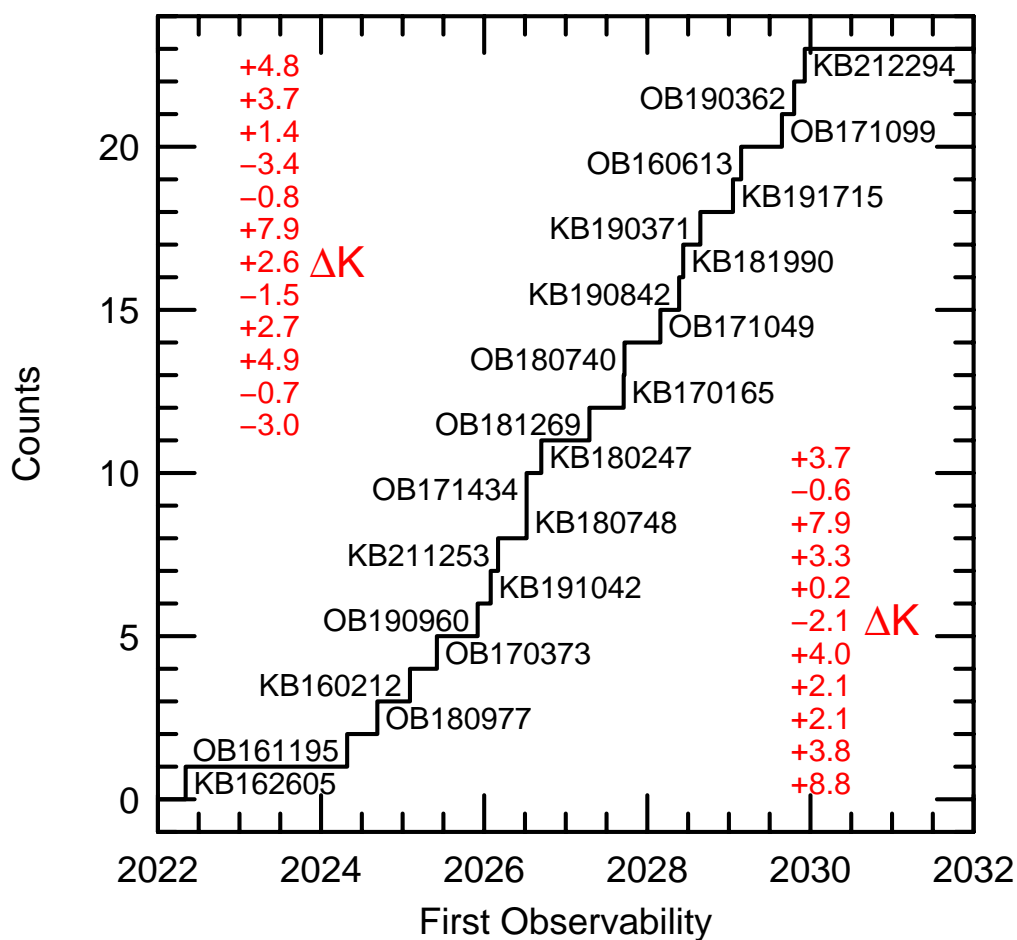


Fig. 8.— Estimated cumulative distribution of planetary events that can be observed with Keck AO as a function of time. The estimate is based on planetary events from Table 1, which are labeled in the figure. However, the actual choice of targets must be based on much more detailed assessments than were used to make this figure. In particular, the vertical red columns at either side show the estimated K -band contrast ratio (expressed as a magnitude difference), which are derived from Bayesian estimates and other information: only about half of the 23 events will actually be resolvable prior to 30m-class AO.

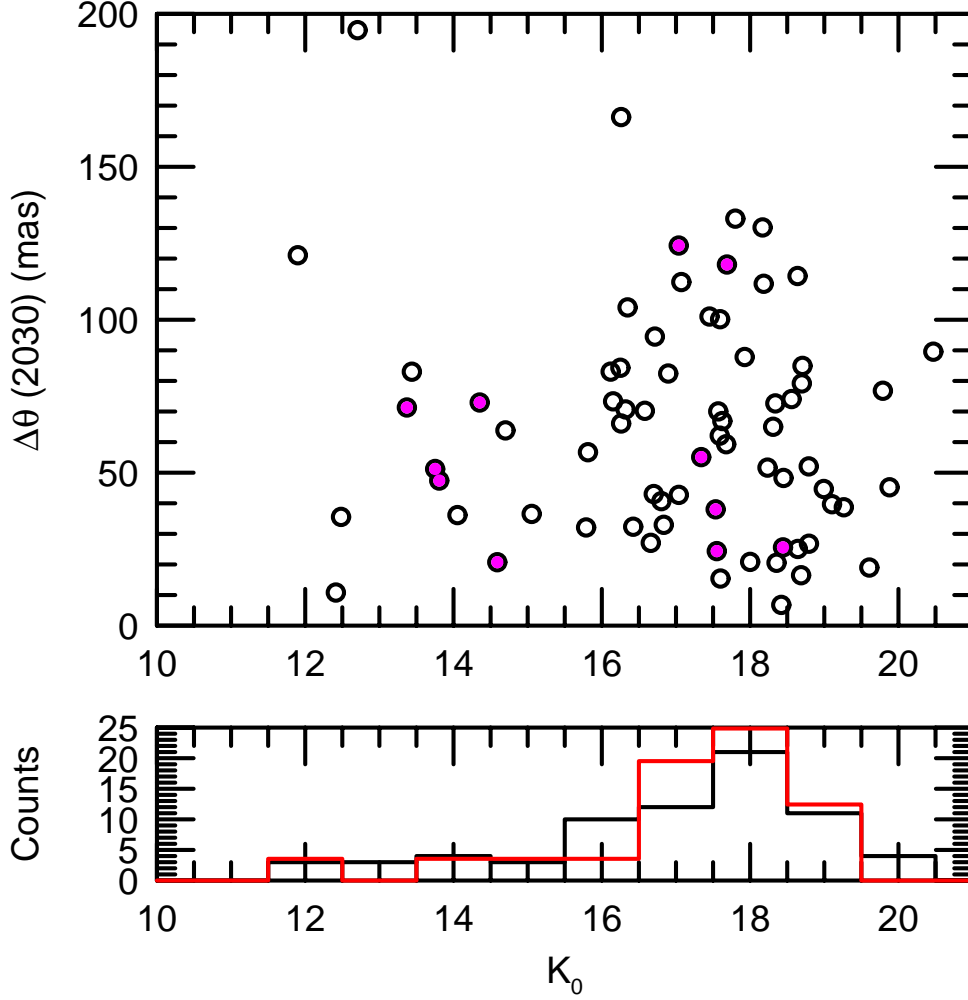


Fig. 9.— Upper panel: Scatter plot of expected lens-source separation in 2030 (i.e., nominal first AO light on 30m class telescopes) versus K_0 for 71 potential targets with μ_{rel} measurements. Events with *Spitzer* measurements are shown in magenta. Intrinsically brighter sources are likely to have greater source-lens contrast ratios and so require greater separations. Only (2, 5) planets have $\Delta\theta < (10, 20)$ mas, and four of these five have relatively faint sources. Hence, a substantial majority of the sample should be accessible in 2030. Lower panel: Histograms of the same 71 potential targets with μ_{rel} measurements (black) and of 40 other potential targets without μ_{rel} measurements (red). The latter are scaled to have the same total area. The two distributions are similar.

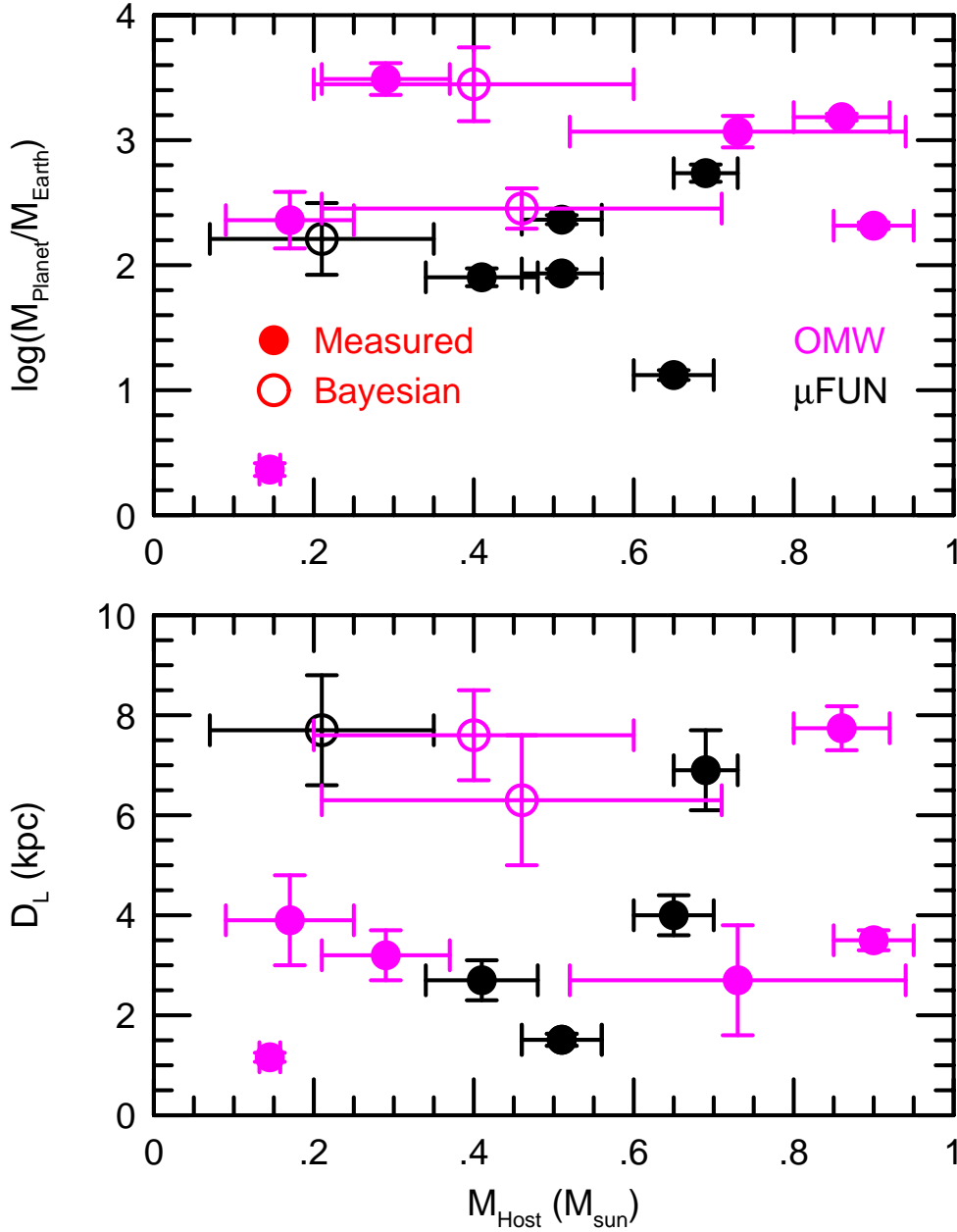


Fig. 10.— Upper panel: Logarithm of planet mass versus host mass for the samples of 6 planets (from 5 events) from the μFUN study of Gould et al. (2010) (black) and of the 8 planets from the OGLE-MOA-Wise study of Shvartzvald et al. (2016) (magenta). Lower panel: Lens distance versus host mass for the same sample. The open symbols are based on a Bayesian estimate while the filled symbols are based on direct measurements. The lower panel suggests that planet frequency may be higher for more nearby hosts, but no strong conclusion can be drawn due to small number statistics.